nature medicine

Article

https://doi.org/10.1038/s41591-025-03501-4

Pandemic monitoring with global aircraft-based wastewater surveillance networks

Received: 31 July 2024

Accepted: 7 January 2025

Published online: 12 February 2025

Check for updates

Guillaume St-Onge[1,2,3] ✉, Jessica T. Davis[1,3], Laurent Hébert-Dufresne[4,5,6], Antoine Allard[4,6,7], Alessandra Urbinati[1,3], Samuel V. Scarpino[2,3,4,8,9], Matteo Chinazzi[1,2,3] & Alessandro Vespignani[1,2,3,10] ✉

Aircraft wastewater surveillance has been proposed as a new approach to monitor the global spread of pathogens. Here we develop a computational framework providing actionable information for the design and estimation of the effectiveness of global aircraft-based wastewater surveillance networks (WWSNs). We study respiratory diseases of varying transmission potential and find that networks of 10–20 strategically placed wastewater sentinel sites can provide timely situational awareness and function effectively as an early warning system. The model identifies potential blind spots and suggests optimization strategies to increase WWSN effectiveness while minimizing resource use. Our findings indicate that increasing the number of sentinel sites beyond a critical threshold does not proportionately improve WWSN capabilities, emphasizing the importance of resource optimization. We show, through retrospective analyses, that WWSNs can notably shorten detection time for emerging pathogens. The approach presented offers a realistic analytic framework for the analysis of WWSNs at airports.

Recent health crises have called attention to the dual role of airports, both in the global spread of infectious diseases and acting as convenient frontlines for detection and monitoring of emerging health threats[1–5]. In this context, aircraft-based wastewater surveillance is gaining increasing scientific and operational interest as a noninvasive method to track pathogens. Traditionally, wastewater surveillance has been used to monitor community prevalence of pathogens such as SARS-CoV-2 variants, poliomyelitis and influenza[6–9]. Expanding wastewater surveillance at airports to create a global wastewater surveillance network (WWSN) has recently been proposed as a new early warning system against emerging pathogens[10–13]. Several national and international initiatives aim to operationalize aircraft wastewater surveillance to enhance global monitoring and early detection of emerging pathogens[14,15]. However, establishing a global WWSN presents challenges, including efficient sample collection, genomic analysis logistics, pathogen selection, optimal airport surveillance, network scaling and addressing blind spots to balance effectiveness and cost[16]. While there have been studies on the feasibility of aircraft wastewater surveillance at several major airports[17–20], fully understanding the performance of a WWSN—in terms of its size, distributed locations and operations—remains to be addressed.

Here, we use the Global Epidemic and Mobility Model (GLEAM)[21–23] to study the performance of global aircraft WWSNs, offering insights

[1]Laboratory for the Modeling of Biological and Socio-technical Systems, Northeastern University, Boston, MA, USA. [2]The Roux Institute, Northeastern University, Portland, ME, USA. [3]Network Science Institute, Northeastern University, Boston, MA, USA. [4]Vermont Complex Systems Institute, University of Vermont, Burlington, VT, USA. [5]Department of Computer Science, University of Vermont, Burlington, VT, USA. [6]Département de physique, de génie physique et d'optique, Université Laval, Québec City, Quebec, Canada. [7]Centre interdisciplinaire en modélisation mathématique, Université Laval, Québec City, Quebec, Canada. [8]Institute for Experiential AI, Northeastern University, Boston, MA, USA. [9]Santa Fe Institute, Santa Fe, NM, USA. [10]Institute for Scientific Interchange Foundation, Turin, Italy. ✉e-mail: g.st-onge@northeastern.edu; a.vespignani@northeastern.edu

https://doi.org/10.1038/s41591-025-03501-4

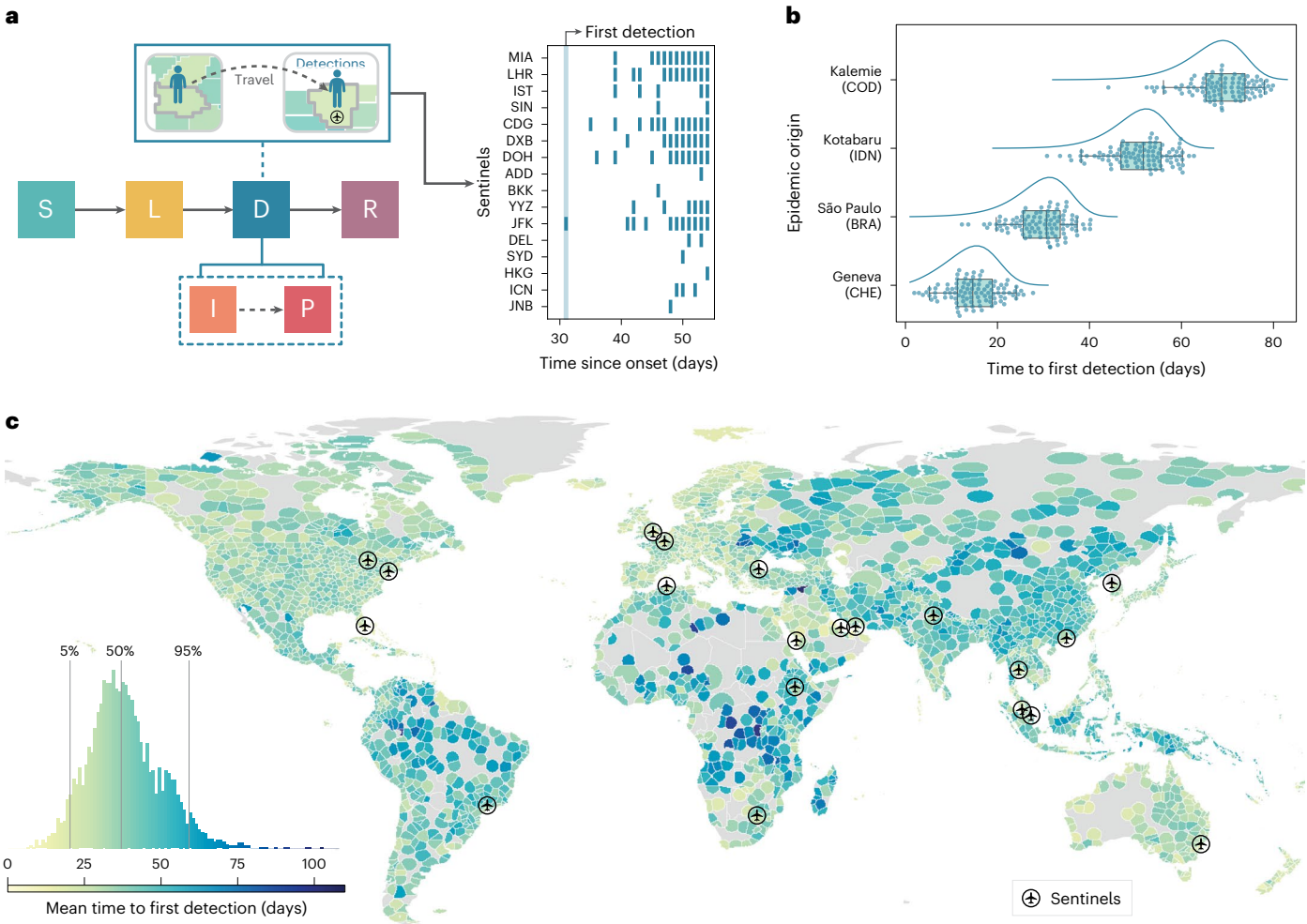

Fig. 1 | Time required to detect a new pathogen with a global surveillance network at airports. a–c, The surveillance network consists of 20 sentinel airports selected for high international passenger volume and geographical diversity (Supplementary Table 6). We use an average $\mathcal{R}_0 = 2$, at the source, T_{gen} of 4 days and a postinfectious period of 10 days, resulting in a detectable period of ~12.7 days. Detectable individuals have a 16% probability of detection on international flights to sentinels. **a**, Schematic of the SLDR model and an example of binary detection time series at sentinel airports, using São Paulo as the origin. Only sentinels (identified by IATA codes) with detections are shown. **b**, Time to first detection by the sentinel network for four origins (ISO 3166-1 alpha-3 country codes of the origins in parentheses). Dots represent GLEAM simulations ($n = 100$ for each origin), with boxplots summarizing the results: median (center line), interquartile range (box) and 90% central prediction interval (whiskers, 5th–95th percentile). Curves show analytical distributions from PGF methodology. **c**, T_{fd} by the network for outbreaks originating from each subpopulation. The histogram (lower left) compiles results from 3,244 subpopulations.

into pathogen spread and detection. GLEAM is a stochastic, spatial, age-structured metapopulation model dividing the global population into over 3,200 subpopulations across more than 200 countries and territories interconnected by air travel and commuting networks. Its air travel component, based on data from over 4,600 airports provided by the Official Aviation Guide (OAG) database, incorporates flight segments and origin–destination information (Methods and Supplementary Information 1). Coupled with an epidemic compartmental model tracking individuals within various disease stages (for example, susceptible, latent and infectious), GLEAM simulates the dissemination of a contagion across subpopulations. It has been used to model global health threats including pandemic influenza, Ebola, Zika and SARS-CoV-2 (refs. 24–26). To simulate a surveillance system within GLEAM, we create a global WWSN that consists of multiple surveillance sites termed sentinels. We assume that each sentinel airport will test the wastewater from a given fraction of international flight arrivals per day.

The model generates stochastic simulations of global epidemic spread from any initial outbreak conditions, producing daily data on infection importations (international and domestic), infection incidence and individual-level detections at sentinel sites. The early growth phase of the modeled epidemics can also be mapped onto a multitype branching process, enabling efficient computation of key analytics via probability-generating functions (PGFs). These analytics include the time to first detection and also, based on sentinel detections, source identification, reproduction number ($\mathcal{R}_0$) estimation and outbreak onset timing. Together, these metrics offer a framework for evaluation of the WWSN's effectiveness in real time for surveillance and public health response.

Results

There are multiple strategies for testing wastewater collected from aircraft for the presence of pathogens. Monitoring efforts can either target a specific pathogen or a priority list of pathogens, such as those identified by the World Health Organization R&D Blueprint, or search for new pathogens using untargeted metagenomic and metatranscriptomic sequencing[11,27]. Each of these strategies can be incorporated into our framework following model adjustment. In this study, we focus on the example of detecting SARS-CoV-2 variants using reverse-transcription

quantitative polymerase chain reaction, with positive samples undergoing whole-genome sequencing to identify specific variants.

We start our analysis by considering a baseline aircraft WWSN with 20 sentinel sites. To achieve sufficient regional coverage, we selected the three busiest international airports from each of the six World Health Organization regions and added two additional sites in South America and Oceania. The locations are shown, by airport markers, in Fig. 1 and are reported in Supplementary Table 6. We show in Supplementary Fig. 14 that selection of less busy airports generally delays disease detection, because larger international hubs offer broader coverage and more frequent flight connections, enabling faster detection.

The efficiency of the WWSN depends on the pathogen's intrinsic characteristics, its detectability and the fraction of aircraft tested at sentinel sites. Here we consider a SARS-CoV-2-like respiratory infection with a wastewater detectability period consistent with reported values in the literature[6,28,29]. We map an individual's disease history to a susceptible–latent–detectable–recovered (SLDR) compartmental structure, as shown in Fig. 1a. Susceptible (S) individuals can become infected through exposure to infectious individuals. Latent (L) individuals have been exposed but are not yet transmitting the pathogen and remain undetectable in the wastewater. Detectable (D) individuals include both infectious (I) individuals who can transmit the pathogen and postinfectious (P) individuals who no longer infect others but are still detectable through wastewater. Finally, recovered (R) individuals are no longer detectable and cannot be reinfected (Methods and Supplementary Information 1).

Each traveling detectable individual arriving at a sentinel on an international flight is detected with probability p_{det}. The detection rate, p_{det}, combines the fraction of sampled aircraft, the probability an individual uses the lavatory during a flight and the probability that a detectable individual is shedding sufficient virus to lead to a detection. Because current detectability estimates for SARS-CoV-2 in aircraft wastewater vary considerably[10,12,19], our analysis varies p_{det} from 4 to 32%. This variation in probability accounts for different estimates of detectability in the wastewater and different fractions of flights tested (Methods includes a detailed discussion). While sampling of individual aircraft independently maximizes detection accuracy, testing combined wastewater at a consolidation point, such as an airport triturator, may be more cost effective. Thus we assume pooled sampling, in which multiple detectable individuals traveling through the same sentinel on the same day result in a single detection, producing binary detection time series as shown in Fig. 1a. It is worth noting that most of these assumptions can be adjusted to accommodate alternative detection schemes, sampling cadences and sentinel site locations.

Baseline WWSN performance

A key metric for evaluating the effectiveness of a WWSN is the time to first detection of an emerging pathogen. This metric measures the number of days from an outbreak onset to the first detection at any sentinel. We simulate an epidemic seeded in one subpopulation with ten latent and ten infectious individuals. The time to first detection depends on the WWSN configuration, outbreak origin, pathogen traits, p_{det} and stochastic variations in travel and detection events.

In Fig. 1b, we show the full probability distribution for the time to first detection for four different origins: Geneva (Switzerland), São Paulo (Brazil), Kotabaru (Indonesia) and Kalemie (Democratic Republic of the Congo). The time to first detection varies widely, from a mean of 14.2 days (90% PI, 4–22) for Geneva to 66.5 days (90% PI, 53–76) for Kalemie, where PI is central prediction interval (5th–95th percentiles). For assessment of WWSN performance globally, we calculate the mean time to first detection, T_{fd}, for each of the >3,200 subpopulations in the model (Fig. 1c). A notable aspect is the important spatial variability of T_{fd} based on the epidemic's origin. For certain locations in Central Africa, T_{fd} is in the order of 100 days, while for many places in Europe, 15–25 days is more typical. While Fig. 2 shows that detection of epidemics emerging from some continents takes, on average, more time than for others, we also note an important heterogeneity within continents (Extended Data Table 1). For instance, in Africa, the 90% PI of T_{fd} ranges from 23 to 71 days. Zooming in at the level of statistical subregions, as defined by the United Nations geoscheme (Supplementary Fig. 6), we still find broad distributions of T_{fd} for all subregions. Middle Africa, for instance, is very dispersed, with 90% PI ranging from 28.2 to 84.5 days. This result indicates that, across regions and scales, there exist blind spots where detection of epidemics would take much longer if they were the source. Blind spots in the WWSN are partly due to low per-capita travel volume, as shown by the strong inverse correlation between international travel volume and T_{fd} (Supplementary Fig. 8). However, in some cases, detection at sentinel sites relies on importations from secondary outbreak locations with community transmission. This indirect path to reaching a sentinel further increases detection time from specific locations.

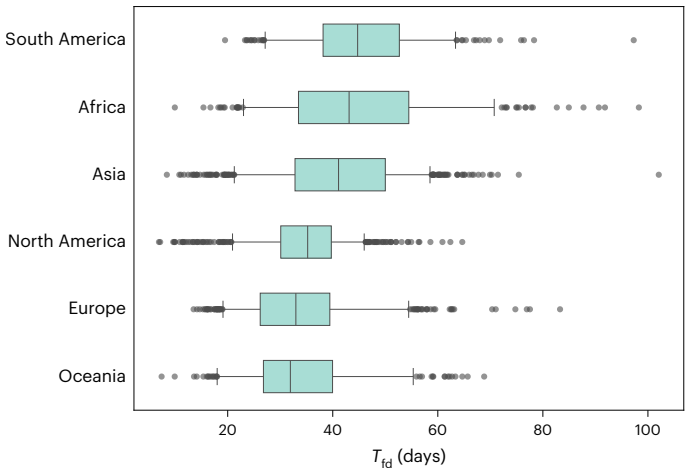

Fig. 2 | Heterogeneity of T_{fd} within geographical regions. We aggregate T_{fd} obtained from Fig. 1 over continents (South America, $n = 297$; Africa, $n = 338$; Asia, $n = 867$; North America, $n = 854$; Europe, $n = 596$; Oceania, $n = 292$). Boxplots show the median (center line), interquartile range (box), 90% central PI (whiskers, 5th–95th percentile) and outliers outside the interval (black dots). Numerical values for some statistics of T_{fd} are reported in Extended Data Table 1.

In Figs. 1 and 2, we assume that p_{det} in the WWSN is 16% and is uniform across all 20 sentinels. This probability of detection amounts to sampling from about 50% of international inbound flights, depending on the estimates for lavatory use and detectable shedding in fecal matter (Methods). In Supplementary Fig. 4, we report additional results for p_{det} as low as 4%, thus assuming a fraction of flights sampled in the range 12–25%. The aforementioned heterogeneity of T_{fd} persists across the full range of p_{det}.

While our analysis focuses on T_{fd} for situational awareness, the effectiveness of an outbreak response also depends on both outbreak size and the number of infections already dispersed internationally, along with their potential for cryptic transmission. To address these factors, we provide in Fig. 3 modeling estimates of both the number of infectious individuals at the source and the number of internationally dispersed infections at the time of first detection by the global WWSN (Supplementary Information 3). In Fig. 3a,b, it is evident that a longer T_{fd} is strongly associated with a larger outbreak in the country of origin (Pearson's $r = 0.906$, two-sided $P = 1.4 \times 10^{-6}$). It is worth noting that our analysis assumes unmitigated scenarios until detection, although large outbreaks would probably be identified earlier at the source, triggering mitigation policies. Interestingly, the number of international introductions at the time of first detection remains relatively stable, typically within the range of a few dozen infected individuals (Fig. 3c,d). This quantity does not exhibit a statistically significant association with T_{fd} (Pearson's $r = 0.289$, two-sided $P = 0.277$). Regardless of

https://doi.org/10.1038/s41591-025-03501-4

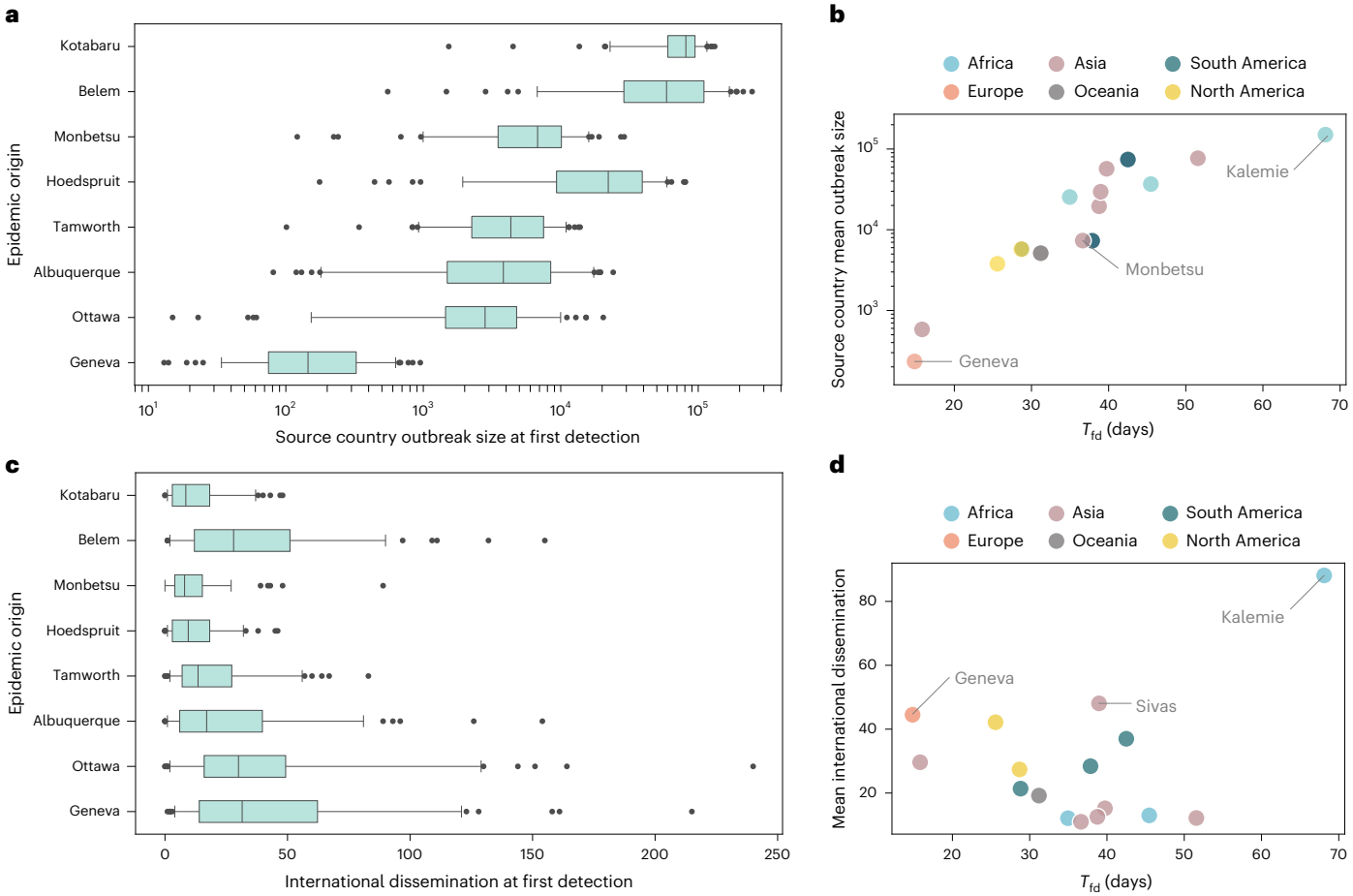

Fig. 3 | Additional performance metrics for global surveillance network at airports. a–d, We use the same baseline WWSN and disease parameters as in Fig. 1. GLEAM simulations ($n = 100$ for each origin) quantify the outbreak size—number of infectious individuals—in the country of origin (**a**,**b**) and the number of latent or infectious carriers disseminated internationally (**c**,**d**) at the time of first detection. **a**, Source country outbreak size at first detection. **b**, Source country mean outbreak size against T_{fd}. Pearson correlation coefficient is 0.906 (90% CI 0.781–0.961, two-sided $P = 1.4 \times 10^{-6}$, testing noncorrelation) between T_{fd} and the logarithm of mean outbreak size in the country of origin ($n = 16$ origins). **c**, International dissemination at first detection. **d**, Mean international dissemination against T_{fd}. Pearson correlation coefficient is 0.289 (90% CI −0.156 to 0.638, two-sided $P = 0.277$, testing noncorrelation) between T_{fd} and mean number of disease carriers disseminated internationally (n = 16 origins). **a**,**c**, Simulation results ($n = 100$) for eight origins, ordered by decreasing T_{fd}. Boxplots show the median (center line), interquartile range (box), 90% central PI (whiskers, 5th–95th percentile) and outliers (black dots).

the outbreak's origin, the WWSN detects the pathogen after a similar number of infections have spread internationally. This suggests that a global WWSN would provide early situational awareness for international public health responses, despite variability in detection time and local outbreak size.

Effects of pathogen characteristics on the WWSN

Although the model is designed to accommodate any specific pathogen and its shedding mechanisms, it is important to note that the natural history of a disease, particularly its key characteristic times and $\mathcal{R}_0$, considerably impacts T_{fd}. In Fig. 4a, we show how the global distribution of T_{fd}, aggregated over all locations, changes with variation in $\mathcal{R}_0$, generation time (T_{gen}) and surveillance p_{det}. A higher $\mathcal{R}_0$ and shorter T_{gen} lead to shorter T_{fd}, and vice versa; the lower the probability of detection, the longer is T_{fd}, although with limited impact. This can be explained by the exponential growth of epidemics in their early stages. The WWSN will typically start detecting cases when there is a sufficient number of detectable individuals (D) traveling through it; this number is approximately $D \propto 2^{T_{fd}/T_2}$, where T_2 is the doubling time of the epidemic (here measured in days). Adjusting either $\mathcal{R}_0$ or T_{gen} greatly affects T_{fd}, due to the change in T_2. Conversely, changes in p_{det} do not similarly impact timing. Indeed, a twofold reduction in p_{det} implies a twofold increase in D before detection. However, this increase in D happens within the span of a single T_2. The exponential growth also implies that the ratio T_{fd}/T_2 should be approximately constant as T_2 of the epidemic varies. More precisely, as shown in Fig. 4b, the complete invariant quantity reads as

$$T_{fd}/T_2 + \log_2 T_2 = \text{constant}. \quad (1)$$

The correction term $\log_2 T_2$ is necessary to account for the stochastic nature of the detection process[30] (Supplementary Information 2). In Fig. 4c, we also show how the distributions of T_{fd} collapse onto one another when considering the invariant quantity in equation (1). In practical terms, altering the disease characteristics effectively results in a linear transformation of T_{fd} across all locations (Supplementary Fig. 10). Therefore, focusing on a specific parametrization does not result in any loss of generality of the results, allowing for consistent and generalizable analyses. Other aspects of disease transmission affecting T_{fd}—overdispersion of the secondary infection distribution, length of the detectable period and seasonal change in the air travel network—have a more limited impact (Supplementary Table 4).

Scaling and optimization of WWSNs

Both the number and geographic placement of sentinel airports are critical for optimization of WWSN effectiveness, representing a classic

https://doi.org/10.1038/s41591-025-03501-4

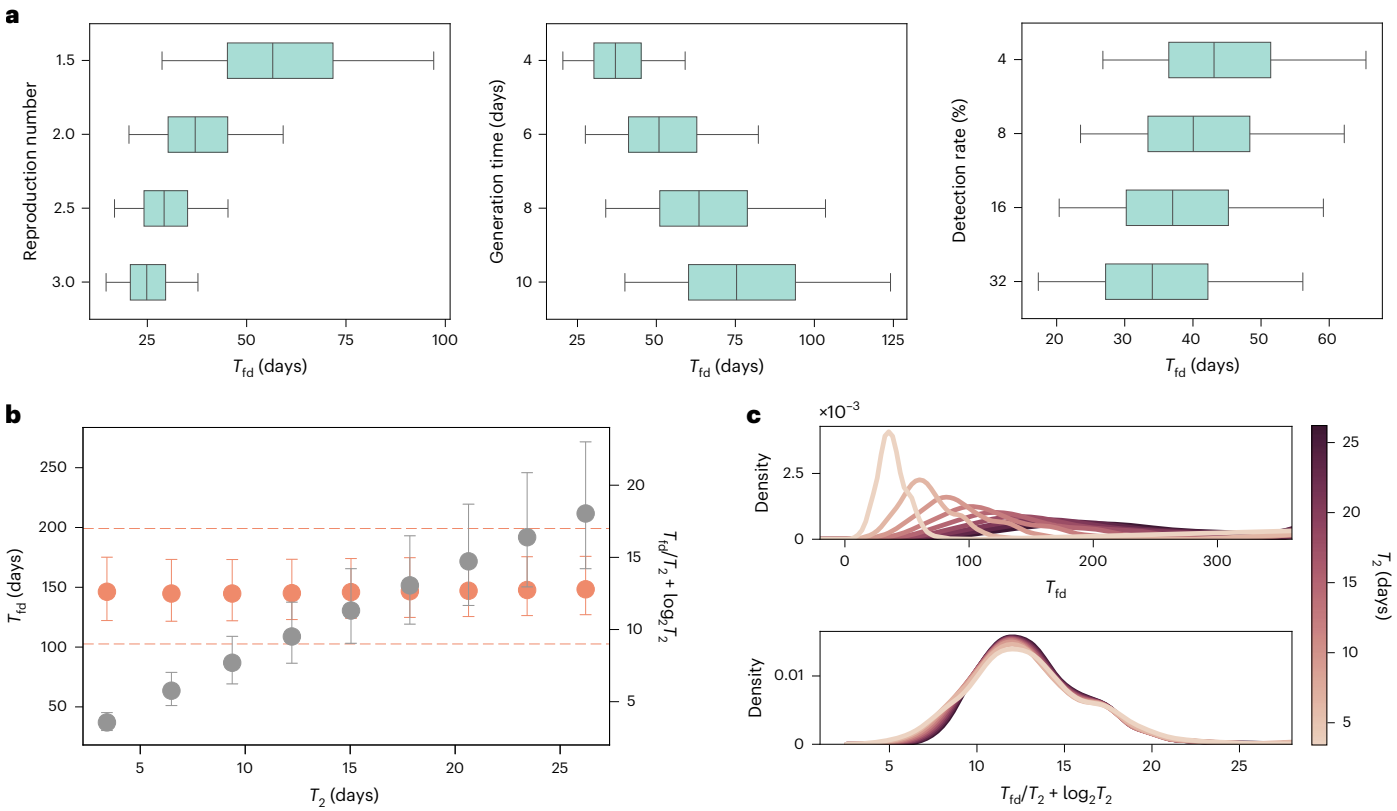

Fig. 4 | Changing transmission dynamics predictably affects T_{fd}. **a**–**c**, We use the same baseline WWSN and detectable period as in Fig. 1. Unless specified, we maintain an average $\mathcal{R}_0$ of 2, T_{gen} of 4 days and 16% p_{det} at sentinels. All prediction intervals are obtained with $n = 3{,}244$ subpopulations. **a**, T_{fd} from all origins, with varying $\mathcal{R}_0$ (left), T_{gen} (middle) and p_{det} (right). Boxplots show the median (center line), interquartile range (box) and 90% central PI (whiskers, 5th–95th percentile) ($n = 3{,}244$); outliers outside the interval are not shown. **b**,**c**, We vary T_{gen} between 4 and 36 days, resulting in T_2 between 3.4 and 26.2 days. **b**, T_{fd} and $T_{fd}/T_2 + \log_2 T_2$ as a function of T_2. Circles indicate the median and error bars cover the interquartile range ($n = 3{,}244$). Dashed lines are purely a visual guide. **c**, Distributions of T_{fd} and $T_{fd}/T_2 + \log_2 T_2$ over all origins for different T_2. For enhanced visualization, we use kernel density estimates for distributions.

resource-constrained optimization challenge. For systematic assessment of network efficiency, we define more precisely $T_{fd}(\mathcal{S}, l)$ as the mean time to first detection for a WWSN configuration, where $\mathcal{S}$ denotes the set of sentinel sites and l indicates the subpopulation at the epidemic's origin. We can then average this metric over multiple origins by weighing each location according to a prior distribution, $P(l)$, for the occurrence of an outbreak, resulting in

$$T_{fd}(\mathcal{S}) = \sum_l P(l)\, T_{fd}(\mathcal{S}, l). \quad (2)$$

While $T_{fd}(\mathcal{S})$ is a well-defined indicator of performance, its value is sensitive to variation in disease transmission characteristics (equation (1)). To provide a more informative measure of network efficiency, we compare $T_{fd}(\mathcal{S})$ with $T_{fd}(\mathcal{C})$, where the latter is for a hypothetical complete WWSN $\mathcal{C}$ that includes all international airports globally. This comparison helps us quantify the relative performance of a specific sentinel configuration $\mathcal{S}$. We define excess time for the sentinel system $\mathcal{S}$ using the following formula:

$$E(\mathcal{S}) = 100 \times \frac{T_{fd}(\mathcal{S}) - T_{fd}(\mathcal{C})}{T_{fd}(\mathcal{C})}. \quad (3)$$

This metric represents the additional percentage of time required for the system $\mathcal{S}$ to achieve its first detection compared with the complete network.

We use three different strategies to define the geographic distribution of the sentinel network: (1) ranking of airports based on their international inbound passenger volume[11]; (2) ranking airports by their entropy in traffic flows—a measure of diversity that favors airports offering wide geographical connectivity; and (3) using a greedy optimization strategy that minimizes T_{fd} (Methods). We acknowledge here that a wide range of approaches and alternative optimization strategies for network surveillance can be explored[31–33]. However, evaluation of these algorithms is beyond the scope of this manuscript and is left for future case-specific studies. In Fig. 5a we show excess time for the three different strategies considered, assuming a homogeneous prior for the source of an epidemic, irrespective of the area or population size (that is, $P(l)$ = constant for all l). While the greedy approach systematically provides the lowest excess time, all three strategies show similar performance despite different network configurations (Supplementary Table 6). The radar chart also shows that the greedy strategy achieves relatively balanced geographical surveillance compared with the complete WWSN. Most notably, optimization analysis yields diminishing returns as the number of sentinels increases. A network of 20 sentinels detects outbreaks only ~20% more slowly than a system with thousands of airports, and doubling this number improves detection time by less than 10%. This result indicates a highly cost-effective trade-off between the efficiency of the WWSN and the resources allocated to it. A small number of sentinels provides near optimal efficiency.

Some diseases are endemic in only certain parts of the world, or have clear seasonal patterns; besides, we have shown that T_{fd} is higher for some geographical areas than others (Fig. 2). For these reasons, the WWSN can be adapted by biasing the optimization procedure to improve detection capabilities for specific geographical areas. The greedy optimization approach allows for this by adjusting the prior

https://doi.org/10.1038/s41591-025-03501-4

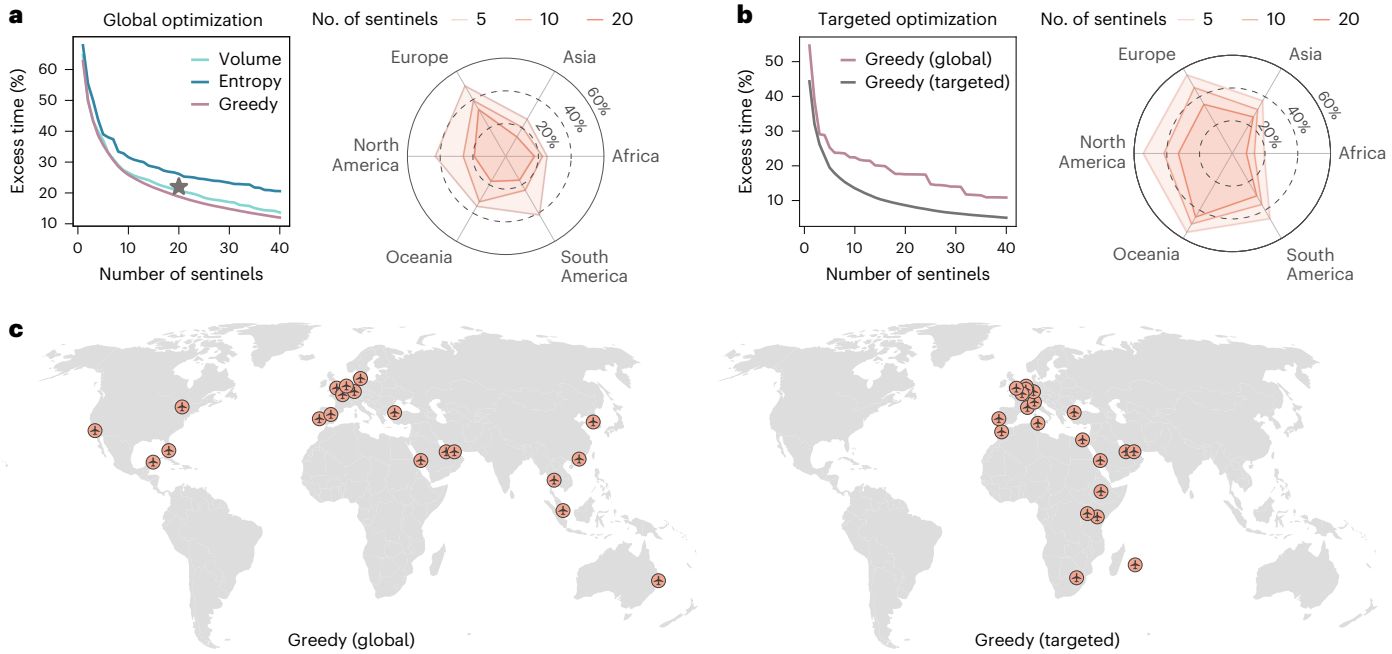

Fig. 5 | Scaling and optimization of a global surveillance network at airports. **a**–**c**, Using the same disease parameters as in Fig. 1, we evaluate T_{fd} and compute excess time relative to the complete WWSN, varying the number of sentinel airports and selection strategies. **a**, Global optimization assumes that all subpopulations are equally probable epidemic origins, with the star indicating the baseline network's excess time. **b**, Targeted optimization minimizes excess time for epidemics originating in Africa. **a**,**b**, Radar charts show excess time by continent for global and targeted greedy strategies. A balanced strategy minimizes excess time across all regions, while lower excess times for a specific region reflect targeted optimization. **c**, Spatial distribution of the first 20 sentinels under global and targeted optimization strategies.

function $P(l)$. For instance, to minimize T_{fd} for outbreaks originating in Africa, we can set $P(l)$ = constant if l is in Africa and $P(l) = 0$ otherwise. Figure 5b compares excess time between conventional global greedy optimization and our targeted greedy optimization strategy. The radar chart highlights the bias introduced by targeted optimization, with coverage favoring Africa at the expense of other regions. Figure 5c shows how sentinel geographical placement shifts substantially when optimization focuses on a specific area. Targeting Africa leads to a higher concentration of sentinels in Africa and Europe, reflecting traffic flow patterns. European hubs are selected due to their high international travel volume, including traffic from many African countries. For example, Paris Charles de Gaulle Airport emerges as the second-top sentinel when optimization is targeting the African continent (Supplementary Table 6). Sentinel selection, however, depends on the specific disease considered and regional characteristics, requiring case-by-case optimization. These findings pave the way for dynamic adaptation of the WWSN to evolving epidemic knowledge and geographic spread.

Situational awareness with WWSNs

WWSNs can be used to provide evolving situational awareness on emerging infectious disease threats. To illustrate the potential use of WWSNs in gathering epidemiological information, we explore the emergence of the SARS-CoV-2 Alpha variant (B.1.1.7) in Fall 2020 (Supplementary Information 4)[34–36]. More precisely, we consider a hypothetical scenario where the baseline WWSN illustrated in Fig. 1 is assumed to be operational. The study uses air travel data from September to November 2020, and in Fig. 6a we present probable distributions for the date of first detection of the Alpha variant. Our findings show that, even with 4% p_{det}, the Alpha variant would probably have been detected by November, with a median detection date of 13 November and 90% PI from 15 October to 1 December. At 16% p_{det}, the first detections are projected by late October, with a median date of 29 October and 90% PI from 2 October to 16 November. Because the Alpha variant was first reported by the UK government on 14 December 2020 (ref. 37), these results show the potential of a global WWSN as an effective early warning system.

Alongside tracking of the initial international spread, the WWSN can also deliver timely information on the origin of an outbreak and help in understanding its growth dynamics. In Fig. 6b, we show the probability that the WWSN correctly identifies the continent and country of origin as multiple detections accumulate in the system. This is achieved by calculating the posterior distribution $P(l|\mathbf{d})$ for each subpopulation l as being the origin of an epidemic based on the cumulative number of detections at each sentinel $\mathbf{d} = (d_v)_{v \in S}$ (Supplementary Information 4). Our analysis suggests that the source country could have been accurately identified after about 20 detections, probably by 5 December in over 50% of model realizations, with 16% p_{det}. In practice, a more efficient adaptive strategy could involve targeted sampling of aircraft from regions suspected as the outbreak's epicenter, enabling quicker and more precise source identification. In addition, multiple detection events can be utilized to estimate key epidemic parameters, including growth rate, onset time and reproduction number, given knowledge of the contagion's T_{gen}. Here, we focus on inferring the epidemic start date and the Alpha variant's increased transmissibility compared with the original SARS-CoV-2 strain. As of 14 December 2020, when the UK first reported the Alpha variant, detection events at sentinel sites produce a joint posterior distribution for the epidemic start date (90% credible interval (CI) 29 July–12 October) and increased transmissibility (90% CI, 25–91%), as shown in Fig. 6c. The high-posterior-density region also matches closely the value of the simulation experiment—that is, a start date of 15 September and 55% increased transmissibility. The detailed inference procedure and individual posterior distributions for different time series are reported in Supplementary Information 4. Additional evidence of the timely situational awareness capacities provided by a global WWSN is presented in Supplementary Information 4, with the hypothetical scenario in

https://doi.org/10.1038/s41591-025-03501-4

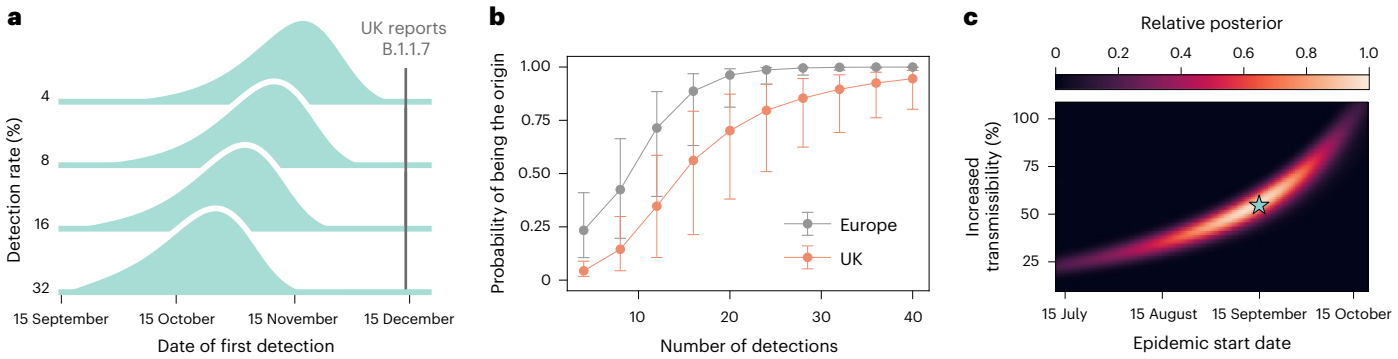

Fig. 6 | WWSN as an early warning system with inferential capabilities. a–**c**, We simulate a counterfactual scenario of the emergence of the SARS-CoV-2 Alpha variant with a global WWSN in place, using the baseline surveillance system from Fig. 1. The wild strain (effective reproduction number $\mathcal{R}_{\text{eff}}^{\text{ws}} = 1.1$) and Alpha variant ($\mathcal{R}_{\text{eff}}^{\text{alpha}} = 1.7$, 55% increase in transmissibility) are modeled with a T_{gen} of 6.5 days and postinfectious period of 10 days. The outbreak starts with 20 infectious and 20 latent individuals in London and southeast England on 15 September, 2020. **a**, Distribution for the date of first infection for varying p_{det}. **b**,**c**, Inference using GLEAM-generated data with 16% p_{det}. **b**, Geolocation of the source improves as detections accumulate; posterior distributions for epidemic origin are based on sentinel detection counts, with markers for median posterior values and error bars for interquartile range (derived from 1,250 detection time series). **c**, Joint posterior distribution of Alpha's increased transmissibility and epidemic start date, averaged over 125 detection time series. Blue star represents ground truth (15 September and 55% increased transmissibility). The use of Gouraud interpolation enhances visualization.

which a global WWSN would have been operational at the time of the emergence of SARS-CoV-2 in Wuhan, China.

Discussion

Our findings demonstrate the potentially important role of WWSNs in shortening pathogen detection time, overcoming some of the challenges faced with standard symptoms-based passenger screening across regions[38]. Gaining even a few extra days of situational awareness about a pathogen's introduction can be critical for outbreak control. For example, in the case of the Alpha SARS-CoV-2 variant, sentinel systems can retrospectively determine the pathogen's introduction date and geographic spread, informing travel restrictions and border screening policies. While these measures are costly, they are often implemented too narrowly or too late to be fully effective. WWSNs can provide timely and precise surveillance data, supporting more effective public health responses. In addition, our framework identifies potential blind spots in WWSNs, guiding the integration of complementary surveillance methods, such as community wastewater monitoring, to increase the network's coverage and effectiveness[39].

The strategies and numerical experiments presented here aim to present the capabilities of a WWSN rather than focus on a specific disease or outbreak. The proposed model integrates real-world airline data and can be extended to include travel disruptions (for example, cancellations, rerouting or restrictions)[26]. It can also account for vaccination effects, such as reduced transmissibility, immune proportions and varying viral shedding rates among vaccinated individuals. Future studies could expand the model's application by incorporating knowledge and experiences from the surveillance of specific pathogens, such as arboviruses and influenza[40,41]. In addition, incorporation of factors influencing zoonotic spillovers—shaped by socioeconomic, environmental and ecological dynamics—will enhance our understanding of emerging diseases and our predictive capabilities[42–45].

Future modeling efforts should incorporate the logistical capabilities of WWSNs, exploring operational implementations such as rotating testing schedules and cadences across sentinel sites to address logistical constraints. For instance, although we used the same detection probability across the WWSN, in Supplementary Information 2 we present a sensitivity analysis with varying levels of heterogeneity for detection probability at sentinel airports, demonstrating that T_{fd} remains robust, with results similar to the homogeneous case shown in Fig. 1. Our modeling framework also enables targeted and adaptive strategies to enhance pathogen screening efficiency while optimizing resource use. It is worth remarking, however, that following detection of an outbreak, response actions must balance social, economic and public health priorities while considering available resources, logistical constraints and the specific disease threat. Our modeling framework supports this process by planning of in silico WWSNs that aligns with the potential response strategies.

Like all modeling studies, our analysis contains assumptions and limitations that must be clearly identified. We model air travel as an independent process for individuals, neglecting clusters and household travel. Spillover events affecting isolated individuals with disease-specific behaviors may lead to variable early-stage dynamics; we mitigate these effects by using small clusters of infected individuals as initial conditions. More technically, some of our analytics rely on a multitype branching process that ignores saturation effects from finite populations. While these effects are minor and do not impact early outbreak conclusions, they should be considered when analyzing WWSN performance for large epidemics or endemic situations. In addition, the model does not account for false positives or positive tests resulting from uncleaned wastewater tanks between flights[19]. While this is unlikely to affect considerably our analysis of T_{fd}, it may influence analysis of the situational awareness capabilities of the WWSN. Future studies should incorporate test specificity, and potential wastewater tank cross-contamination, into the model. This will be crucial for decision-making, particularly when detecting rare but high-consequence pathogens.

Taking into account its limitations, our study provides a general framework for modeling wastewater surveillance at airports, supporting public health decision-making through both planning and surveillance modes. In the planning mode, the model identifies optimal sentinel networks and evaluates effectiveness using metrics such as T_{fd}. In surveillance mode, it estimates key epidemiological parameters such as transmission characteristics and outbreak timing from detection events. Furthermore, although our study focuses on aircraft wastewater surveillance, it can also be applied to environmental monitoring and other travel-based surveillance methods, such as nasal swab testing, offering a comprehensive modeling platform for genomic and travel-based disease surveillance.

Online content

Any methods, additional references, Nature Portfolio reporting summaries, source data, extended data, supplementary information, acknowledgements, peer review information; details of author contributions

and competing interests; and statements of data and code availability are available at https://doi.org/10.1038/s41591-025-03501-4.

References

1. Williams, G. H. et al. SARS-CoV-2 testing and sequencing for international arrivals reveals significant cross border transmission of high risk variants into the United Kingdom. *eClinicalMedicine* **38**, 101021 (2021).
2. Bart, S. M. et al. Effect of predeparture testing on postarrival SARS-CoV-2-positive test results among international travelers — CDC traveler-based genomic surveillance program, four U.S. airports, March–September 2022. *MMWR Morb. Mortal. Wkly Rep.* **72**, 206–209 (2023).
3. Wegrzyn, R. D. et al. Early detection of severe acute respiratory syndrome Coronavirus 2 variants using traveler-based genomic surveillance at 4 US airports, September 2021–January 2022. *Clin. Infect. Dis.* **76**, e540–e543 (2022).
4. National Academies of Sciences, Engineering, and Medicine. *Improving the CDC Quarantine Station Network's Response to Emerging Threats* (The National Academies Press, 2022).
5. Kucharski, A. J. et al. Real-time surveillance of international SARS-CoV-2 prevalence using systematic traveller arrival screening: an observational study. *PLOS Med.* **20**, e1004283 (2023).
6. Foladori, P. et al. SARS-CoV-2 from faeces to wastewater treatment: what do we know? A review. *Sci. Total Environ.* **743**, 140444 (2020).
7. Keshaviah, A. et al. Separating signal from noise in wastewater data: an algorithm to identify community-level COVID-19 surges in real time. *Proc. Natl Acad. Sci. USA* **120**, e2216021120 (2023).
8. Brouwer, A. F. et al. Epidemiology of the silent polio outbreak in Rahat, Israel, based on modeling of environmental surveillance data. *Proc. Natl Acad. Sci. USA* **115**, E10625–E10633 (2018).
9. Wolfe, M. K. et al. Wastewater-based detection of two influenza outbreaks. *Environ. Sci. Technol. Lett.* **9**, 687–692 (2022).
10. Farkas, K. et al. Wastewater-based monitoring of SARS-CoV-2 at UK airports and its potential role in international public health surveillance. *PLOS Glob. Public Health* **3**, e0001346 (2023).
11. Li, J. et al. A global aircraft-based wastewater genomic surveillance network for early warning of future pandemics. *Lancet Glob. Health.* **11**, e791–e795 (2023).
12. Jones, D. L. et al. Suitability of aircraft wastewater for pathogen detection and public health surveillance. *Sci. Total Environ.* **856**, 159162 (2023).
13. Shingleton, J. W., Lilley, C. J. & Wade, M. J. Evaluating the theoretical performance of aircraft wastewater monitoring as a tool for SARS-CoV-2 surveillance. *PLOS Glob. Public Health* **3**, e0001975 (2023).
14. Traveler-based genomic surveillance for early detection of new SARS-CoV-2 variants. *US Centers for Disease Control and Prevention* https://wwwnc.cdc.gov/travel/page/travel-genomic-surveillance (accessed 16 January 2025).
15. EU Wastewater Observatory for Public Health. *European Commission* https://wastewater-observatory.jrc.ec.europa.eu/#/guidance/2 (accessed 16 January 2025).
16. Bivins, A., Morfino, R., Franklin, A., Simpson, S. & Ahmed, W. The lavatory lens: tracking the global movement of pathogens via aircraft wastewater. *Crit. Rev. Environ. Sci. Technol.* **54**, 321–341 (2023).
17. Albastaki, A. et al. First confirmed detection of SARS-COV-2 in untreated municipal and aircraft wastewater in Dubai, UAE: the use of wastewater based epidemiology as an early warning tool to monitor the prevalence of COVID-19. *Sci. Total Environ.* **760**, 143350 (2021).
18. Ahmed, W. et al. Detection of the Omicron (B.1.1.529) variant of SARS-CoV-2 in aircraft wastewater. *Sci. Total Environ.* **820**, 153171 (2022).
19. Ahmed, W. et al. Wastewater surveillance demonstrates high predictive value for COVID-19 infection on board repatriation flights to Australia. *Environ. Int.* **158**, 106938 (2022).
20. Morfino, R. C. et al. Notes from the field: aircraft wastewater surveillance for early detection of SARS-CoV-2 variants — John F. Kennedy International Airport, New York City, August–September 2022. *Morb. Mortal. Wkly Rep.* **72**, 210–211 (2023).
21. Balcan, D. et al. Multiscale mobility networks and the spatial spreading of infectious diseases. *Proc. Natl Acad. Sci. USA* **106**, 21484–21489 (2009).
22. Balcan, D. et al. Modeling the spatial spread of infectious diseases: the global epidemic and mobility computational model. *J. Comput. Sci.* **1**, 132–145 (2010).
23. Chinazzi, M. et al. A multiscale modeling framework for scenario modeling: characterizing the heterogeneity of the COVID-19 epidemic in the US. *Epidemics* **47**, 100757 (2024).
24. Tizzoni, M. et al. Real-time numerical forecast of global epidemic spreading: case study of 2009 A/H1N1pdm. *BMC Med.* **10**, 165 (2012).
25. Zhang, Q. et al. Spread of Zika virus in the Americas. *Proc. Natl Acad. Sci. USA* **114**, E4334–E4343 (2017).
26. Davis, J. T. et al. Cryptic transmission of SARS-CoV-2 and the first COVID-19 wave. *Nature* **600**, 127–132 (2021).
27. Levy, J. I., Andersen, K. G., Knight, R. & Karthikeyan, S. Wastewater surveillance for public health. *Science* **379**, 26–27 (2023).
28. Weiss, A., Jellingsø, M. & Sommer, M. O. A. Spatial and temporal dynamics of SARS-CoV-2 in COVID-19 patients: a systematic review and meta-analysis. *EBioMedicine* **58**, 102916 (2020).
29. Li, Q. et al. Number of COVID-19 cases required in a population to detect SARS-CoV-2 RNA in wastewater in the province of Alberta, Canada: sensitivity assessment. *J. Environ. Sci.* **125**, 843–850 (2023).
30. Gautreau, A., Barrat, A. & Barthélemy, M. Global disease spread: statistics and estimation of arrival times. *J. Theor. Biol.* **251**, 509–522 (2008).
31. Leskovec, J. et al. Cost-effective outbreak detection in networks. In *Proc. 13th ACM SIGKDD International Conference on Knowledge Discovery and Data Mining* 420–429 (ACM, 2007).
32. Brockmann, D. & Helbing, D. The hidden geometry of complex, network-driven contagion phenomena. *Science* **342**, 1337–1342 (2013).
33. Pei, S., Teng, X., Lewis, P. & Shaman, J. Optimizing respiratory virus surveillance networks using uncertainty propagation. *Nat. Commun.* **12**, 222 (2021).
34. Kraemer, M. U. G. et al. Spatiotemporal invasion dynamics of SARS-CoV-2 lineage B.1.1.7 emergence. *Science* **373**, 889–895 (2021).
35. Davies, N. G. et al. Estimated transmissibility and impact of SARS-CoV-2 lineage B.1.1.7 in England. *Science* **372**, eabg3055 (2021).
36. Volz, E. et al. Assessing transmissibility of SARS-CoV-2 lineage B.1.1.7 in England. *Nature* **593**, 266–269 (2021).
37. COVID-19 – United Kingdom of Great Britain and Northern Ireland. *World Health Organization* www.who.int/emergencies/disease-outbreak-news/item/2020-DON304 (accessed 16 January 2025).
38. Niehus, R., De Salazar, P. M., Taylor, A. R. & Lipsitch, M. Using observational data to quantify bias of traveller-derived COVID-19 prevalence estimates in Wuhan, China. *Lancet Infect. Dis.* **20**, 803–808 (2020).
39. Keshaviah, A. et al. Wastewater monitoring can anchor global disease surveillance systems. *Lancet Glob. Health* **11**, e976–e981 (2023).
40. Polgreen, P. M. et al. Optimizing influenza sentinel surveillance at the state level. *Am. J. Epidemiol.* **170**, 1300–1306 (2009).

41. Scarpino, S., Meyers, L. A. & Johansson, M. Design strategies for efficient arbovirus surveillance. *Emerg. Infect. Dis.* **23**, 642–644 (2017).
42. Jones, K. E. et al. Global trends in emerging infectious diseases. *Nature* **451**, 990–993 (2008).
43. Watts, N. et al. Health and climate change: policy responses to protect public health. *Lancet* **386**, 1861–1914 (2015).
44. Carlson, C. J. et al. Climate change increases cross-species viral transmission risk. *Nature* **607**, 555–562 (2022).
45. Becker, D. J. et al. Optimising predictive models to prioritise viral discovery in zoonotic reservoirs. *Lancet Microbe* **3**, e625–e637 (2022).

Methods

GLEAM

GLEAM is a computational platform used for modeling epidemic spread, combining stochastic elements and spatial data in an age-structured, metapopulation framework[21–23]. GLEAM divides the world into distinct geographic subpopulations using a Voronoi tessellation of the Earth's surface, with each subpopulation centered around major transportation hubs such as airports. These subpopulations are detailed with high-resolution data about population demographics, age-specific contact patterns, health infrastructure and other relevant attributes based on available data. GLEAM incorporates a human mobility layer into its modeling, using data from various sources, including the OAG and International Air Transport Association (IATA) databases. This layer includes both short-range (for example, commuting) and long-range (for example, flights) mobility data, and creates a network of daily passenger flows between airports worldwide. The model uses a worldwide homogeneous standard for commuting and compensates for missing information with synthetic data based on the 'gravity law' calibrated with real data[21,23].

GLEAM tracks the number of individuals in each disease state for all subpopulations over time. It simulates travelers' movements through the flight network, with air travel probabilities varying by age group. Finally, the disease dynamics and the detection process at airports within GLEAM are simulated using stochastic binomial chain processes. These processes rely on parameter values sourced from existing literature, defining the natural history of the infection being modeled. See Supplementary Information 1 for a more technical description of the model. All our analyses make use of a global air travel network capturing the period September 2022 to August 2023, except for the case studies on the emergence of COVID-19 (Supplementary Section 4) and the SARS-CoV-2 Alpha variant, for which we use data from December 2018 to February 2019 (the available air travel networks at the beginning of the COVID-19 pandemic) and September to November 2020, respectively.

Disease progression and transmission dynamics

For modeling of disease transmission within subpopulations and detections at airports following air travel, we make use of a standard compartmentalization scheme for disease progression. Each individual, at any time point, is assigned to a compartment corresponding to their particular disease-related state. An individual who becomes infected will go through the following sequence of states: susceptible (S, pre-exposure), latent (L, exposed, but does not yet transmit the infectious pathogen), infectious (I, can transmit the disease), postinfectious (P, no longer infectious) and recovered (R). In our model, we assume that only infectious and postinfectious can be detected through wastewater, which we regroup under the detectable (D) state. Inclusion of the postinfectious state in our model is necessary because viruses such as SARS-CoV-2 remain detectable in wastewater well beyond the active infectious period of the single individual[6,28,29]. Furthermore, since the period an individual spends in a certain compartment is typically not exponentially distributed[46,47], we add realism to our model by decomposing the infectious and postinfectious states into two substates, namely I_1 and I_2, and P_1 and P_2. Parameters and details on the contagion dynamics (T_{gen}, T_2, detectable period and $\mathcal{R}_0$) are reported in the Supplementary Information.

Aircraft wastewater detection

In our model, a detectable individual passing through a sentinel site is detected with probability p_{det} that depends on several factors, including the cadence and sampling of airport wastewater surveillance, the duration of the flight, the diverse sociodemographic profiles of the passengers[12] and so on. In our analysis we assume that, on average, p_{det} is uniform across all inbound international flights arriving at any given sentinel site. To provide a rationale for the spectrum of p_{det} examined in this study, we break down probability into the following components—$p_{det} = p_{lav} \times p_{shed} \times p_{sample}$, where p_{lav} represents the likelihood that an individual will utilize the lavatory and consequently deposit detectable genetic traces of the pathogen in the wastewater; p_{shed} denotes the probability that a detectable individual is actively shedding the pathogen at levels sufficient for detection in the wastewater; and p_{sample} refers to the proportion of flights that are subjected to sampling at the sentinel airport.

The proportion of adult passengers defecating on flights, critical for estimation of p_{lav}, is surveyed to be less than 13% on short-haul and less than 36% on long-haul flights[12]. Further, p_{shed}, the probability of detectable pathogen shedding in fecal matter, ranges between 30 and 60% for SARS-CoV-2 (ref. 12). This would correspond to a p_{det} per passenger on sampled flights ($p_{lav} \times p_{shed}$) in the range 11–22% on long-haul flights. These estimates are possibly a large underestimation for viruses such as SARS-CoV-2, because individuals can leave genetic material in the wastewater without defecating[48], such as by disposing of a used tissue or spitting in the toilet. Indeed, previous studies[19] have shown 83.7% accuracy in detection of COVID-19 on repatriation flights using wastewater analysis. Translating this value to an individual's marginal detection probability is complex, because the number of COVID-19 cases per flight varied considerably, averaging 4.62 cases. Accounting for false-positive wastewater results, assuming each case had an equal probability to be detected and a flat prior, we find a median marginal p_{det} of 51% (90% CI, 28–72) on sampled flights. However, this value could be inflated, notably due to the persistent nature of fecal RNA shedding compared with respiratory shedding[49], and accounting for the fact that not all international flights are long haul.

Interpolating from the above values, we consider an estimate of 32% for the p_{det} of a single detectable passenger on a flight subject to wastewater sampling ($p_{lav} \times p_{shed}$). In our analysis, we assume a baseline p_{det} of 16%, which corresponds to sampling 50% of international flights ($p_{sample} = 50\%$). Given the variability in these estimates, we also explore a range of p_{det}, from as high as 32% to as low as 4%, acknowledging that only a small fraction (for example, 12%) of flights might be sampled. Our sensitivity analysis presents findings across this full spectrum of p_{det} (Figs. 4a and 6a and Supplementary Fig. 4).

PGF analytics

The mechanistic GLEAM model uses large-scale stochastic simulations that are computationally intensive. To streamline our analysis, for most of the results in this paper we utilize PGFs to efficiently extract the required analytic information from the data and model. PGFs are a standard tool in mathematical epidemiology[50,51] and have found many applications, including the quantitative analysis of the risk of disease introduction[52–55].

PGFs are useful in counting elements. Here we are counting individuals based on certain properties: their age, their location and their epidemiological state. We define s_σ as the number of individuals of type σ. For instance, s_σ could represent the current number of latent individuals in a given location and of a certain age. We use the vector $\mathbf{s}$ to encapsulate all these numbers.

To capture the full stochastic evolution of the system, we encode the probability distribution $P(\mathbf{s}, t)$ with a multivariate PGF

$$\Psi^t(\boldsymbol{x}) = \sum_{\mathbf{s}} P(\mathbf{s}, t) \prod_{\sigma} x_\sigma^{s_\sigma}, \tag{4}$$

where the sum (product) runs over all possible values of $\mathbf{s}$ (σ) and each x_σ is a variable that acts as a placeholder to encode probability distribution. The vector $\mathbf{x}$ encapsulates all these variables.

In the early stage, a structured metapopulation epidemic model such as GLEAM can be described by a multitype branching process[56], in which case we solve the PGF through the recursive equation

$$\Psi^{t+1}(\boldsymbol{x}) = \Psi^t[\mathbf{F}(\mathbf{x})], \tag{5}$$

where $\mathbf{F}(\mathbf{x})$ is a vector and each element $F_\sigma(\mathbf{x})$ is itself a PGF that characterizes the offspring distribution of an individual of type σ. Computing the full distribution $P(\mathbf{s}, t)$ is out of reach—the number of terms explodes combinatorially. However, computing marginal or joint distributions for a few observables, such as the total number of individuals in a particular state, is possible (Supplementary Information 1).

Taken together, the recursive evaluation of PGFs and their numerical inversion to recover probability distributions represents a very efficient computational alternative to Monte Carlo simulations. This crucially allows us to extract distributions of observables, like the time to first detection, assuming that the epidemic could have started from any of the >3,200 subpopulations of our model, a task that would be prohibitive with a purely simulation-based framework. See Supplementary Information 1 for an in-depth description and characterization of the PGF methodology.

WWSN optimization algorithms

The heuristic optimization of global WWSNs selects sentinel sites based on their rankings according to the following measures. Let $N_{l\to v}$ be the number of individuals per day who will travel and arrive at airport v on an international flight, either as a final destination or for a connection; the flows of international passengers generate a weighted bipartite network connecting international airports v to subpopulations l. We can therefore rank airports based on their volume of international travel:

$$c_v^{\mathrm{vol}} = \sum_l N_{l\to v}. \tag{6}$$

A second-ranking measure is based on each airport traffic entropy, defined as:

$$c_v^{\mathrm{ent}} = -\sum_l \left(\frac{N_{l\to v}}{\sum_{l'} N_{l'\to v}}\right) \log\left(\frac{N_{l\to v}}{\sum_{l'} N_{l'\to v}}\right). \tag{7}$$

This expression is also known as Shannon's diversity index; this measure favors airports with a broad and homogeneous coverage of the different subpopulations.

A more refined optimization algorithm aims at minimizing the T_{fd} of an epidemic, averaged over all potential origins. We can assign an arbitrary prior probability $P(l)$ for location l to be the origin of an epidemic, resulting in the following objective function:

$$\Phi(\mathcal{S}) \equiv T_{\mathrm{fd}}(\mathcal{S}) = \sum_l P(l)\, T_{\mathrm{fd}}(\mathcal{S}, l), \tag{8}$$

where $T_{\mathrm{fd}}(\mathcal{S}, l)$ is T_{fd}, assuming that the epidemic started in subpopulation l and that the WWSN consists of the set of sentinel airports $\mathcal{S}$. For global optimization we use $P(l) = \text{const.}\ \forall l$—that is, all subpopulations are an equiprobable source. For targeted optimization, we use $P(l) = \text{const.}$ for locations in the targeted region and $P(l) = 0$ otherwise.

We conjecture that $-\Phi(\mathcal{S})$ is a monotone submodular set function[57]. We prove this statement in Supplementary Information 2 for a very accurate approximation of $-\Phi(\mathcal{S})$, but the exact case remains to be proven. Monotone submodular functions have desirable properties in relation to discrete optimization problems: we have a guarantee on the performance of a greedy optimization algorithm—that is, there exists an upper bound on the value of $\Phi(\mathcal{S})$ obtained through this approach[57]. Most importantly, in practice, a greedy algorithm should find a solution that is very close to the optimal one. Consequently, to minimize the objective function, equation (8), we use the following greedy optimization scheme:

(1) Define an initial set S (can be empty).
(2) For each airport $v \notin \mathcal{S}$, compute $\Phi(\mathcal{S} \cup \{v\})$.
(3) Update the set $\mathcal{S} \leftarrow \mathcal{S} \cup \{v^\star\}$, where v^* is the sentinel airport that minimizes the objective function.
(4) Repeat steps 2 and 3 until a desired number of sentinels is reached.

Reporting summary

Further information on research design is available in the Nature Portfolio Reporting Summary linked to this article.

Data availability

Proprietary airline data are commercially available from OAG (https://www.oag.com/passenger-booking-data). Data on the effective reproduction number in London and southeast England during fall 2020 are available from the UK government website (https://www.gov.uk/guidance/the-r-value-and-growth-rate). Source data are provided with this paper.

Code availability

The mechanistic GLEAM model is publicly available at http://www.gleamviz.org/ and can be used to generate simulation data. The code associated with PGF methodology is publicly available on GitHub (https://github.com/mobs-lab/pgfgleam), with documentation to compute the analytics in this paper. All data analyses of model results were performed using Python v.3.10.8.

References

46. Wearing, H. J., Rohani, P. & Keeling, M. J. Appropriate models for the management of infectious diseases. *PLOS Med.* **2**, 621–627 (2005).
47. Krylova, O. & Earn, D. J. D. Effects of the infectious period distribution on predicted transitions in childhood disease dynamics. *J. R. Soc. Interface* **10**, 20130098 (2013).
48. Crank, K., Chen, W., Bivins, A., Lowry, S. & Bibby, K. Contribution of SARS-CoV-2 RNA shedding routes to RNA loads in wastewater. *Sci. Total Environ.* **806**, 150376 (2022).
49. Zhang, Y. et al. Prevalence and persistent shedding of fecal SARS-CoV-2 RNA in patients with COVID-19 infection: a systematic review and meta-analysis. *Clin. Transl. Gastroenterol.* **12**, e00343 (2021).
50. Brauer, F., Van den Driessche, P., Wu, J. & Allen, L. J. *Mathematical Epidemiology* (Springer, 2008).
51. Miller, J. C. A primer on the use of probability generating functions in infectious disease modeling. *Infect. Dis. Model.* **3**, 192–248 (2018).
52. Johansson, M. A., Powers, A. M., Pesik, N., Cohen, N. J. & Staples, J. E. Nowcasting the spread of Chikungunya virus in the Americas. *PLoS ONE* **9**, e104915 (2014).
53. Mier-y Teran-Romero, L., Tatem, A. J. & Johansson, M. A. Mosquitoes on a plane: disinsection will not stop the spread of vector-borne pathogens, a simulation study. *PLoS Negl. Trop. Dis.* **11**, e0005683 (2017).
54. Lai, S. et al. Seasonal and interannual risks of dengue introduction from South-East Asia into China, 2005-2015. *PLOS Negl. Trop. Dis.* **12**, e0006743 (2018).
55. Truelove, S. et al. Epidemics, air travel, and elimination in a globalized world: the case of measles. Preprint at *medRxiv* https://doi.org/10.1101/2020.05.08.20095414 (2020).
56. Lahodny, G. E. & Allen, L. J. S. Probability of a disease outbreak in stochastic multipatch epidemic models. *Bull. Math. Biol.* **75**, 1157–1180 (2013).
57. Nemhauser, G. L., Wolsey, L. A. & Fisher, M. L. An analysis of approximations for maximizing submodular set functions—I. *Math. Program.* **14**, 265–294 (1978).

Acknowledgements
This work was in part supported by the Bill & Melinda Gates Foundation (no. INV-058220 to G.S.-O., J.T.D., A.U., M.C. and A.V.). Under the grant conditions of the Foundation, a Creative Commons Attribution 4.0 Generic License has already been assigned to the author accepted manuscript version that might arise from this submission. We acknowledge support from contract no. CDC-75D301Cl4810 (G.S.-O., M.C. and A.V.) and cooperative agreement no. CDC-RFA-FT-23-0069 from the CDC's Center for Forecasting and Outbreak Analytics (to G.S.-O., J.T.D., A.U., S.V.S., M.C. and A.V.). G.S.-O. acknowledges financial support from Fonds de recherche du Québec – Nature et technologies (project no. 313475). L.H.-D. is supported by the National Institutes of Health Centers of Biomedical Research Excellence Award no. P20GM125498. A.A. acknowledges support from the Natural Sciences and Engineering Research Council of Canada (project nos. 2019-05183 and 2024-05626). The findings and conclusions in this study are those of the authors and do not necessarily represent the official position of the funding agencies, the CDC or the US Department of Health and Human Services.

Author contributions
Conceptualization was contributed by G.S.-O., J.T.D., M.C. and A.V. Methodology was undertaken by G.S.-O., J.T.D., L.H.-D., A.A., M.C. and A.V. Investigation was carried out by G.S.-O., J.T.D. and A.V. G.S.-O. and A.V. wrote the original draft. Review and editing were performed by G.S.-O., J.T.D., L.H.-D., A.A., A.U., S.V.S., M.C. and A.V.

Competing interests
S.V.S. is a paid consultant at Verily. The other authors declare no competing interests.

Additional information
Extended data is available for this paper at https://doi.org/10.1038/s41591-025-03501-4.

Supplementary information The online version contains supplementary material available at https://doi.org/10.1038/s41591-025-03501-4.

Correspondence and requests for materials should be addressed to Guillaume St-Onge or Alessandro Vespignani.

Peer review information *Nature Medicine* thanks Aaron Bivins and the other, anonymous, reviewer(s) for their contribution to the peer review of this work. Primary Handling Editor: Lorenzo Righetto, in collaboration with the *Nature Medicine* team.

https://doi.org/10.1038/s41591-025-03501-4

Extended Data Table 1 | Statistics of the mean time to first detection

Continent	Sample size *n*	Minimum	5th percentile	Median	Mean	95th percentile	Maximum
South America	297	19.5	27.1	44.7	45.4	63.4	97.3
Africa	338	9.9	23	43.1	45.3	71	98.3
Asia	867	8.4	21.3	41.1	41.1	58.7	102.1
North America	854	6.9	20.8	35.2	34.6	46.1	64.7
Europe	596	13.5	19.1	33	33.7	54.5	83.3
Oceania	292	7.4	18	31.9	33.9	55.6	68.8

Numerical values for some of the statistics of the mean time to first detection presented in Fig. 2.

nature portfolio

Corresponding author(s): Alessandro Vespignani

Last updated by author(s): Dec 11, 2024

Reporting Summary

Nature Portfolio wishes to improve the reproducibility of the work that we publish. This form provides structure for consistency and transparency in reporting. For further information on Nature Portfolio policies, see our Editorial Policies and the Editorial Policy Checklist.

Statistics

For all statistical analyses, confirm that the following items are present in the figure legend, table legend, main text, or Methods section.

n/a	Confirmed
☐	☒ The exact sample size (*n*) for each experimental group/condition, given as a discrete number and unit of measurement
☒	☐ A statement on whether measurements were taken from distinct samples or whether the same sample was measured repeatedly
☐	☒ The statistical test(s) used AND whether they are one- or two-sided *Only common tests should be described solely by name; describe more complex techniques in the Methods section.*
☒	☐ A description of all covariates tested
☒	☐ A description of any assumptions or corrections, such as tests of normality and adjustment for multiple comparisons
☐	☒ A full description of the statistical parameters including central tendency (e.g. means) or other basic estimates (e.g. regression coefficient) AND variation (e.g. standard deviation) or associated estimates of uncertainty (e.g. confidence intervals)
☐	☒ For null hypothesis testing, the test statistic (e.g. *F*, *t*, *r*) with confidence intervals, effect sizes, degrees of freedom and *P* value noted *Give P values as exact values whenever suitable.*
☐	☒ For Bayesian analysis, information on the choice of priors and Markov chain Monte Carlo settings
☒	☐ For hierarchical and complex designs, identification of the appropriate level for tests and full reporting of outcomes
☒	☐ Estimates of effect sizes (e.g. Cohen's *d*, Pearson's *r*), indicating how they were calculated

Our web collection on statistics for biologists contains articles on many of the points above.

Software and code

Policy information about availability of computer code

Data collection	No software was used for data collection.
Data analysis	The mechanistic GLEAM model is publicly available at http://www.gleamviz.org/ and can be used to generate simulation data. The code associated with the probability generating function methodology is publicly available on Github (https://github.com/mobs-lab/pgfgleam) with documentation to compute the analytics in this paper. All data analyses of model results were performed using Python v3.10.8.

For manuscripts utilizing custom algorithms or software that are central to the research but not yet described in published literature, software must be made available to editors and reviewers. We strongly encourage code deposition in a community repository (e.g. GitHub). See the Nature Portfolio guidelines for submitting code & software for further information.

Data

Policy information about availability of data

All manuscripts must include a data availability statement. This statement should provide the following information, where applicable:

- Accession codes, unique identifiers, or web links for publicly available datasets
- A description of any restrictions on data availability
- For clinical datasets or third party data, please ensure that the statement adheres to our policy

The source data for the figures are attached. Proprietary airline data are commercially available from the Official Aviation Guide (https://www.oag.com/passenger-booking-data). Data on the reproduction number in London and South East England during Fall 2020 are available from the United Kingdom government website

(https://www.gov.uk/guidance/the-r-value-and-growth-rate).

Research involving human participants, their data, or biological material

Policy information about studies with human participants or human data. See also policy information about sex, gender (identity/presentation), and sexual orientation and race, ethnicity and racism.

Reporting on sex and gender	Our study didn't involve human participant or human data. Sex and gender were not considered in the study design.
Reporting on race, ethnicity, or other socially relevant groupings	Our study didn't involve human participant or human data. Race, ethnicity, or other socially relevant groupings were not considered in the study design.
Population characteristics	Our study didn't involve human participants.
Recruitment	No participant was recruited for this study.
Ethics oversight	Our study didn't need approval from an organization.

Note that full information on the approval of the study protocol must also be provided in the manuscript.

Field-specific reporting

Please select the one below that is the best fit for your research. If you are not sure, read the appropriate sections before making your selection.

☒ Life sciences ☐ Behavioural & social sciences ☐ Ecological, evolutionary & environmental sciences

For a reference copy of the document with all sections, see nature.com/documents/nr-reporting-summary-flat.pdf

Life sciences study design

All studies must disclose on these points even when the disclosure is negative.

Sample size	We use all available data generated by model simulations. We do not generate primary biological or epidemiological data from field experiments.
Data exclusions	No data were excluded.
Replication	All data used are described in the data availability statement. Model generated data were simulated using the mechanistic GLEAM model and the probability generating function methodology documented in the code availability statement. All attempts at replication were successful.
Randomization	We did not perform/consider individual subject studies. We did not allocate any individuals to control or experimental groups.
Blinding	We did not perform/consider individual subject studies. We did not allocate any individuals to control or experimental groups.

Reporting for specific materials, systems and methods

We require information from authors about some types of materials, experimental systems and methods used in many studies. Here, indicate whether each material, system or method listed is relevant to your study. If you are not sure if a list item applies to your research, read the appropriate section before selecting a response.

Materials & experimental systems

n/a	Involved in the study
☒	☐ Antibodies
☒	☐ Eukaryotic cell lines
☒	☐ Palaeontology and archaeology
☒	☐ Animals and other organisms
☒	☐ Clinical data
☒	☐ Dual use research of concern
☒	☐ Plants

Methods

n/a	Involved in the study
☒	☐ ChIP-seq
☒	☐ Flow cytometry
☒	☐ MRI-based neuroimaging

Plants

Seed stocks	No seed stock or plant material was used.
Novel plant genotypes	No novel plant genotype was produced.
Authentication	No seed stock or plant material was used and no novel plant genotype was produced.

nature medicine

Supplementary information

https://doi.org/10.1038/s41591-025-03501-4

Pandemic monitoring with global aircraft-based wastewater surveillance networks

In the format provided by the authors and unedited

Pandemic monitoring with global aircraft-based wastewater surveillance networks

Supplementary Information

Guillaume St-Onge[1,2,3], Jessica T. Davis[1,3], Laurent Hébert-Dufresne[4,5,6], Antoine Allard[4,6,7], Alessandra Urbinati[1,3], Samuel V. Scarpino[2,3,4,8,9], Matteo Chinazzi[1,2,3], and Alessandro Vespignani[1,2,3,10]

[1] *Laboratory for the Modeling of Biological and Socio-technical Systems, Northeastern University, Boston, MA 02115, USA*
[2] *The Roux Institute, Northeastern University, Portland, ME 04101, USA*
[3] *Network Science Institute, Northeastern University, Boston, MA 02115, USA*
[4] *Vermont Complex Systems Institute, University of Vermont, Burlington, VT 05405, USA*
[5] *Department of Computer Science, University of Vermont, Burlington VT 05405, USA*
[6] *Département de physique, de génie physique et d'optique, Université Laval, Québec City, QC G1V 0A6, Canada*
[7] *Centre interdisciplinaire en modélisation mathématique, Université Laval, Québec City, QC G1V 0A6, Canada*
[8] *Institute for Experiential AI, Northeastern University, Boston, MA 02115, USA*
[9] *Santa Fe Institute, Santa Fe, NM 87501, USA*
[10] *Institute for Scientific Interchange Foundation, Turin, 10126, Italy*

Contents

1 Model description

1.1 Global Epidemic and Mobility Model

The GLEAM (Global Epidemic and Mobility) model is a stochastic epidemic metapopulation framework that incorporates age-based contact matrices and data on human mobility. The approach has been documented in previous publications [1, 2] and has been used to study the spread of diseases such as Ebola [3], Zika [4], and COVID-19 [5, 6].

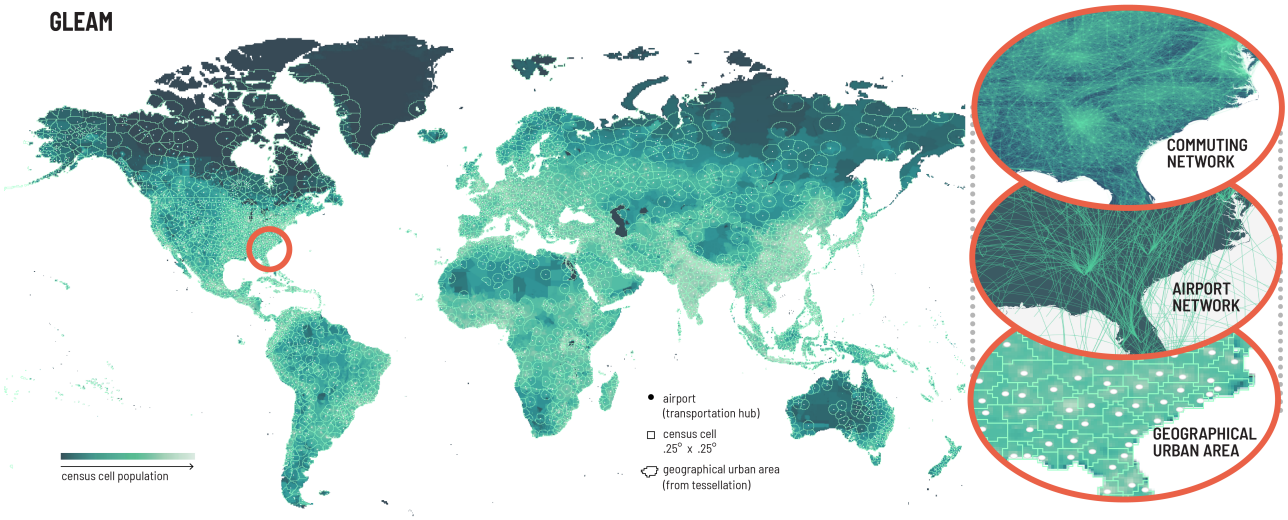

Figure S1: Schematic representation of GLEAM. (left) Voronoi tessellation of the globe centered around transportation hubs (airports) creating each of the 3200+ geographical units that we refer to as subpopulations. Each subpopulation is constructed from census cells of approximately 25km × 25km. (right) For a particular region, we illustrate the subpopulations and the two mobility layers— air travel (long-range) and commuting (short-range).

The model uses a Voronoi tessellation to create a metapopulation network with over 3,200 subpopulations, covering areas of the globe inhabited by humans. These subpopulations are anchored around major transport hubs like airports and are themselves divided into cells measuring around 25 x 25 kilometers, equivalent to 15 x 15 arc minutes. In addition, the model integrates cell-level population data [7] and subpopulation-level age-specific contact patterns using the contact matrices developed in [8]. Here, we consider individuals divided into 5 age groups: [0-4, 5-17, 18-49, 50-64, 65+].

The individual subpopulations are connected through a human mobility layer that combines both short-range (i.e., commuting) and long-range (i.e., flights) mobility data. Commuting data is sourced from the Offices of Statistics for 30 countries on 5 continents. To harmonize the varying spatial resolutions of commuting data across different countries and to address data availability gaps, the short-range mobility layer is synthetically generated where necessary. This is achieved by relying on the "gravity law" [1, 9, 10], which is calibrated on the available data. Air-travel data from the Official Aviation Guide (OAG) and IATA databases is used to build an origin-destination network, incorporating connecting flight information. The network provides daily passenger flows between airports globally, which we systematically map and aggregate at the subpopulation level. Figure S1 displays the geographical resolution of the model for selected regions, illustrating both the short-range and long-range mobility networks and the global population structure.

Compartmental model

The synthetic world created by the human mobility layer couples the epidemic dynamics unfolding within each subpopulation. To model the infection process, we adopt an extended SLIR-like model in which individuals are either susceptible (S), latent (L), infectious (I), post-infectious (P), or removed (R). We further subdivide the infectious and post-infectious compartments into two stages, namely I_1, I_2, P_1, and P_2 to more realistically model the timing of the disease progression [11, 12].

Susceptible individuals become latent through interactions with infectious individuals, at a rate Λ, the *effective*

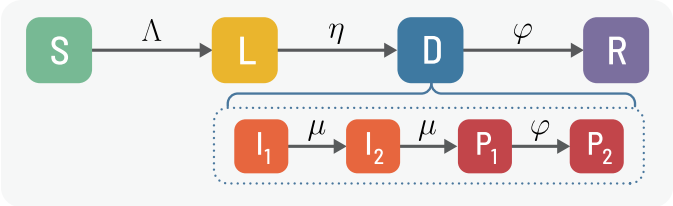

Figure S2: Compartmental model for wastewater surveillance at airports.

force of infection, which depends on the age of the susceptible individual but also on the whole state of the system, and thus varies in time. An important factor influencing the force of infection is the *basic reproduction number* $\mathcal{R}_0$—the average number of secondary infections caused by an infectious individual in a fully healthy population. Note that in our model, the reproduction number $\mathcal{R}_0$ will vary slightly from one subpopulation to another, since it is proportional to the largest eigenvalue of the age-structured contact matrices [8].

Latent individuals then progress to the first infectious stage at a constant rate inversely proportional to the mean latent period $\eta \equiv T_{\text{lat}}$. Infectious individuals in the first stage I_1 progress to the second stage I_2 at a rate $\mu \equiv 2 \times T_{\text{inf}}^{-1}$, where T_{inf} is the mean infectious period; the process is identical for the transition of I_2 individuals to P_1. Similarly, post-infectious individuals in the first stage (P_1) progress to the second stage P_2 at a rate $\varphi \equiv 2 \times T_{\text{post}}^{-1}$, where T_{post} is the mean post-infectious period, then progress to the recovered stage at the same rate φ. The post-infectious period is the length of time that an individual can still shed the virus and remain detectable through wastewater, but not generate any more new infections. Once an individual is in the removed compartment, it can no longer be detected. Here we assume only infectious and post-infectious individuals can be detected through wastewater, which is why we regroup them in a *detectable* (D) meta-compartment. The various transitions and their rates are portrayed in Fig. S2.

Because of the subdivision of the infectious and post-infectious states, the infectious and post-infectious periods are gamma-distributed, while the latent period is exponentially distributed. The *generation time*, the time between the exposures of an infector-infectee pair, will have a mean T_{gen} expressed as [11, 12]

$$T_{\text{gen}} = T_{\text{lat}} + \left(\frac{n_{\text{inf}} + 1}{2n_{\text{inf}}}\right) T_{\text{inf}} \,, \tag{1}$$

where n_{inf} is the number of infectious states—in our model $n_{\text{inf}} = 2$. Similarly, the *detectable period*—the length of time an individual can be detected through wastewater—has a mean of $T_{\text{det}} = T_{\text{inf}} + T_{\text{post}}$.

In this study, we adjust the parameters of our compartmental model disease dynamics by fixing the reproduction number, mean generation time, and mean detectable period. In Table S1 we provide the parameters' ranges considered in this study and compare them with estimated ranges of SARS-CoV-2.

Stochastic simulation of the transmission and mobility dynamics

With the mobility data layers and the disease dynamics defined, the number of individuals in each compartment c, age bracket a, and subpopulation l follows a discrete and stochastic dynamical equation that reads as

$$X_l^{[c,a]}(t + \Delta t) - X_l^{[c,a]}(t) = \Delta X_l^{[c,a]} + \Omega_l([c,a]) \tag{2}$$

where the term $\Delta X_l^{[c,a]}$ represents the changes induced by the disease dynamics and $\Omega_l([c,a])$ represents the variations due to air travel. In this study, each day is subdivided in $m = 12$ time steps, i.e., $\Delta t = 1/m$ days. While the disease dynamics part $\Delta X_l^{[c,a]}$ is applied at every of these time steps, the variations due to traveling $\Omega_l([c,a])$ are introduced daily. The latter $\Omega_l([c,a])$ is directly extracted from a multinomial distribution associated with the age-specific probability of travel per day, as defined by the global air-travel network.

The variation $\Delta X_l^{[c,a]}$ is determined by summing over all transitions in and out of the disease compartment c for

Table S1: Range of disease parameters explored in this study compared with estimates for the early transmission of SARS-CoV-2 (wild strain). †Estimates combine mean generation time and serial interval.

Parameter	Range considered	SARS-CoV-2 (wild strain)	References
Reproduction number	[1.5, 3]	[2, 3.5]	[13–16]
Mean generation time	[4, 36] days	[4, 7.5] days†	[14, 17]
Mean detectable period	[7.7, 22.7] days	[7, 22] days	[18–20]

the age group a,

$$\Delta X_l^{[c,a]} = \sum_{[c',a]} \left\{ -\mathcal{D}_l([c,a],[c',a]) + \mathcal{D}_l([c',a],[c,a]) \right\}, \tag{3}$$

where $\mathcal{D}_l([c,a],[c',a])$ represents the number of transitions from $[c,a]$ to $[c',a]$ during the time interval Δt. For all spontaneous transitions, like from latent to infectious, $\mathcal{D}_l([c,a],[c',a])$ is simply extracted from a binomial distribution.

The generation of new infections is a more complex procedure. First, it hinges on the age-structured contacts matrix $\mathbf{C}$, which gives the expected number of contacts per day between each age pair (a,a') in a given location l. We consider interactions in four social settings: contacts at school ($\mathbf{C}_{school}$), workplace ($\mathbf{C}_{work}$), home ($\mathbf{C}_{home}$), and in the general community ($\mathbf{C}_{community}$), which are linearly combined to create $\mathbf{C}$, as defined in Ref. [8]. Second, the mobility due to the commuting flows is also taken into account using a time scale separation approximation, as detailed in Ref. [1]. Altogether, these two factors contribute to the effective force of infections $\Lambda([l,a])$ acting on susceptible individuals in subpopulation l and age a, resulting in new transitions of the form $\mathcal{D}_l([c,a],[c',a])$.

Initial conditions are established by defining the quantity and location of individuals who can spread the infection. Subsequently, GLEAM tracks the number of individuals in each disease compartment for every subpopulation over time. Please see Ref. [2] for a more in-depth discussion of the simulation framework.

Wastewater detection at airports

We assume that a subset of all airports $\mathcal{S} = \{\nu_1, \nu_2, \dots\}$—*sentinels*—monitor the wastewater of incoming *international* aircrafts. Consequently, each detectable international traveler passing through a sentinel has a probability $p_{\rm det}$ of leading to a detection. As detailed in the Methods section of the main text, the probability $p_{\rm det}$ is a complex quantity combining multiple factors, such as sampling frequency of aircraft, length of the flight, lavatory usage estimates, etc. We settled on performing an extensive sensitivity analysis spanning the range 4–32%.

In GLEAM's stochastic simulation process, detections at sentinels are aggregated during the post-processing of the simulation data, which keeps track of all mobility-induced changes $\Omega_l([c,a])$. Since GLEAM produces origin-destination travel patterns at the level of subpopulations l, we extract from the global air-travel network the probability of detection $p_{l,l'}$ for each travel $l \to l'$. Each travel $l \to l'$ is associated with a set of potential airport *paths* of the form $\mathcal{P} = \nu_1 \to \nu_2 \to \cdots \to \nu_k$. If the path $\mathcal{P}$ contains an international flight $\nu \to \nu'$, where $\nu' \in \mathcal{S}$, then detectable individuals taking this path will be detected with probability $p_{\rm det}$. If a path $\mathcal{P}$ contains $\mathcal{N}(\mathcal{P})$ such international flight to any sentinel, the probability of detection is $1-(1-p_{\rm det})^{\mathcal{N}(\mathcal{P})}$. We therefore calculate

$$p_{l,l'} = \sum_{\mathcal{P}} P(\mathcal{P}|l \to l') \left[1 - (1-p_{\rm det})^{\mathcal{N}(\mathcal{P})} \right], \tag{4}$$

where $P(\mathcal{P}|l \to l')$ is the probability an individual will take the path $\mathcal{P}$, given the travel $l \to l'$.

1.2 Probability generating function framework

To characterize the early phase of an epidemic, we can map the transmission tree to a branching process, from which an efficient *probability generating function* (PGF) methodology can be leveraged [21–25]. This is a standard

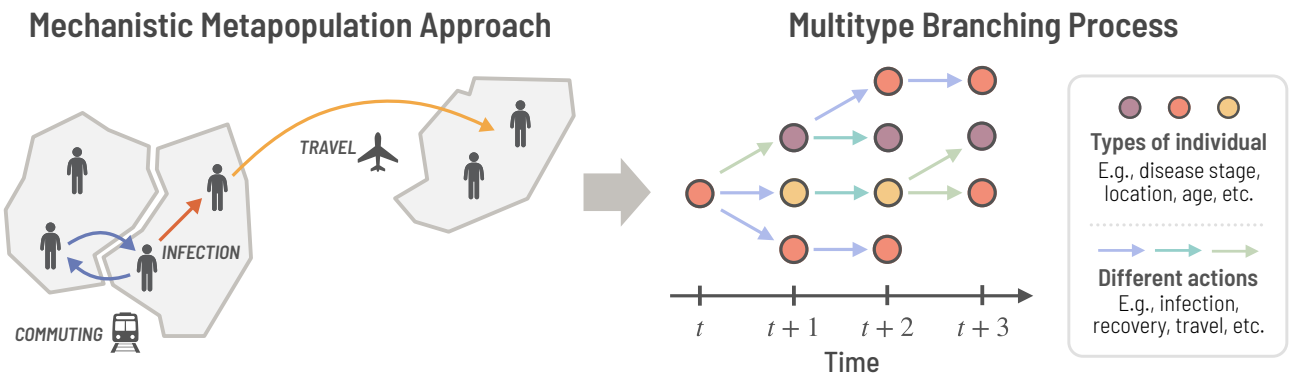

Figure S3: Mapping GLEAM to a multitype branching process. Infections happen within subpopulations—and across adjacent subpopulations when accounting for commuting—and agents can travel between the subpopulations. Individuals are distinguished by their *type*, which encapsulates everything that distinguishes them (like disease stage, age, and location). The early phase of an epidemic naturally takes the form of an event tree encoding all actions happening at each time step, including travel and transmission. This event tree is mathematically described via a multitype branching process.

approach in mathematical epidemiology and has been used, among others, to characterize the time evolution of contagion on heterogeneous networks [26–28], and to quantify the risk of introduction and outbreaks in metapopulation models [29–34]. Here we leverage this methodology by mapping to a multitype branching process the age-structured, stochastic, metapopulation dynamics of GLEAM, the disease progression, and the wastewater surveillance at airports (see Fig. S3).

PGFs are used to encode discrete probability distributions with functions. In the present case, we want to encode the full distribution for the state of the epidemic at all times t—the number of days since the start of the epidemic. The state of the epidemic includes the number of individuals in each stage of the disease, of each age, and in each subpopulation, but also other quantities we want to "measure" (evaluate an associated probability distribution), like the cumulative number of exported cases and the cumulative number of detections on each origin-destination travel ending at a sentinel.

To introduce our formalism, let us define the multi-index $\alpha = (l, a)$ characterizing the location l and the age a of an individual—we refer to α as the *category* of an individual or agent. We define ℓ_α as the number of latent individuals of category α. Since we divide the number of infectious and post-infectious states into two stages (I_1,I_2,P_1, and P_2) we identify them by the numbers $i_{\alpha,1}$, $i_{\alpha,2}$, and $j_{\alpha,1}$,$j_{\alpha,2}$ respectively. To track the number of exported cases, we introduce e_α as the cumulative number of α-agents, either latent or infectious, who were infected previously in another location—they were previously of another category—then traveled, thereby becoming of category α. Finally, to track wastewater detections of detectable individuals (infectious or post-infectious) at sentinel airports, we define $d_{\alpha,\alpha'}$ the cumulative number of detections for international travel $l \to l'$ resulting in a change of category $\alpha \to \alpha'$ for a given age group a. Note that we do not track susceptible or recovered individuals in this framework, since they do not play a significant role in the early phase of an outbreak. The whole state of the system is then described by the tuple of vectors $(\boldsymbol{\ell}, \boldsymbol{i}_1, \boldsymbol{i}_2, \boldsymbol{j}_1, \boldsymbol{j}_2, \boldsymbol{e}, \boldsymbol{d})$, where for instance $\boldsymbol{\ell} = [l_{\alpha_1}, l_{\alpha_2}, \dots]$.

To simplify the notation, we define the *state vector*

$$\boldsymbol{s} = [l_{\alpha_1}, l_{\alpha_2}, \dots, i_{\alpha_1,1}, i_{\alpha_2,2}, \dots, d_{\alpha_1,\alpha_2}, d_{\alpha_1,\alpha_3}, \dots] \equiv [s_1, s_2, \dots] \,, \tag{5}$$

as the concatenation of previous vectors, encoding all information about the system. Each component s_σ of the vector identifies a number we keep track of (e.g., number of infectious of a specific category α) and is associated with nodes

of a specific color in Fig. S3; we refer to σ as the *type* of each node in the multitype branching process representation of the epidemic and mobility dynamics.

Since the state vector is a random variable $\boldsymbol{s}_t$ at each time t, we write the probability of observing a particular state at time t as $P(\boldsymbol{s}_t = \boldsymbol{s}) \equiv P(\boldsymbol{s}, t)$. Finally, we encode this distribution with a PGF (in the compact format) as

$$\Psi^t(\boldsymbol{x}) \equiv \sum_{\boldsymbol{s}} P(\boldsymbol{s}, t) \prod_{\sigma} x_\sigma^{s_\sigma} \ , \tag{6}$$

where the sum runs over all potential values of the vector $\boldsymbol{s}$ and each x_σ is a dummy variable used to track each quantity s_σ.

If we unravel the vector $\boldsymbol{s}$, the PGF is written as

$$\Psi^t(\boldsymbol{z}, \boldsymbol{y}_1, \boldsymbol{y}_2, \boldsymbol{w}_1, \boldsymbol{w}_2, \boldsymbol{v}, \boldsymbol{u}) = \sum_{\boldsymbol{\ell}} \sum_{\boldsymbol{i}_1} \sum_{\boldsymbol{i}_2} \sum_{\boldsymbol{j}_1} \sum_{\boldsymbol{j}_2} \sum_{\boldsymbol{e}} \sum_{\boldsymbol{d}} P(\boldsymbol{\ell}, \boldsymbol{i}_1, \boldsymbol{i}_2, \boldsymbol{j}_1, \boldsymbol{j}_2, \boldsymbol{e}, \boldsymbol{d}, t) \prod_{\alpha,\alpha'} z_\alpha^{\ell_\alpha} y_{\alpha,1}^{i_{\alpha,1}} y_{\alpha,2}^{i_{\alpha,2}} w_{\alpha,1}^{j_{\alpha,1}} w_{\alpha,2}^{j_{\alpha,2}} v_\alpha^{e_\alpha} u_{\alpha,\alpha'}^{d_{\alpha,\alpha'}} \ , \tag{7}$$

where the vector of variables $(\boldsymbol{z}, \boldsymbol{y}_1, \boldsymbol{y}_2, \boldsymbol{w}_1, \boldsymbol{w}_2, \boldsymbol{v}, \boldsymbol{u})$ tracks the quantities $(\boldsymbol{\ell}, \boldsymbol{i}_1, \boldsymbol{i}_2, \boldsymbol{j}_1, \boldsymbol{j}_2, \boldsymbol{e}, \boldsymbol{d})$. For obvious reasons, we will favor the compact representation as much as possible, and use the unraveled vectors only when necessary to specify operations on a subset of the variables.

For a general multitype branching process, the solution is obtained by recursion [26]

$$\Psi^{t+1}(\boldsymbol{x}) = \Psi^t \left[\boldsymbol{F}(\boldsymbol{x}) \right] \ , \tag{8}$$

where $F(\boldsymbol{x}) = [F_1(\boldsymbol{x}), F_2(\boldsymbol{x}), \dots]$ is a vector of PGFs, and each PGF $F_\sigma(\boldsymbol{x})$ characterizes the *offspring* distribution at the next time step for each node of type σ. For instance, assuming σ identifies infectious α-agents in the first stage (I_1), each individual could lead to a certain number of new latent individuals (through transmission), an α-agent in the second stage (I_2) through disease progression, detection at airports through travel, and so forth. Each possible combination of offspring is encoded in a multivariate PGF, $F_\sigma(\boldsymbol{x})$, similar to Eq. (6).

We now decompose the vector of offspring PGFs $\boldsymbol{F}(\boldsymbol{x})$ by describing separately the reaction phase—modeling disease transmission and progression—, and the mobility phase of GLEAM in terms of vectors of PGFs $\boldsymbol{R}(\boldsymbol{x})$ and $\boldsymbol{M}(\boldsymbol{x})$ respectively. From a similar argument justifying Eq. (8), the vector of offspring PGFs is the composition of the PGFs for each phase [26], i.e., $\boldsymbol{F}(\boldsymbol{x}) = \boldsymbol{M}(\boldsymbol{R}(\boldsymbol{x}))$. The order of the composition indicates that air travel is happening *before* the reaction phase, in line with the convention in GLEAM.

Reaction phase: disease transmission and progression

While the PGF framework Eq. (8) is defined at a daily resolution, we model the reaction phase at a finer temporal resolution by dividing each day into $m = 12$ time periods of duration $\Delta t = 1/m$, as in the GLEAM simulation procedure. This provides a more realistic description of the intraday dynamics, especially for rapidly evolving epidemics, but one could work at any temporal resolution without significantly affecting the results. Consequently, the vector of PGFs $\boldsymbol{R}(\boldsymbol{x})$ for the reaction phase itself corresponds to the m-th composition of the vector of PGFs $\boldsymbol{r}(\boldsymbol{x})$, i.e.,

$$\boldsymbol{R}(\boldsymbol{x}) = \underbrace{\boldsymbol{r}(\boldsymbol{r}(\dots \boldsymbol{r}(}_{m \text{ times}} \boldsymbol{x}) \dots)) \ . \tag{9}$$

Each transition in the disease progression has a rate: latent individuals become infectious at rate η, infectious individuals in the first stage transition to the second stage (and then in the post-infectious stage) at rate μ, post-infectious individuals in the first stage transition to the second stage (and then in the removed stage) at rate φ. Also, infectious α-agents (at any stage) interact and transmit the disease to α'-susceptible individuals at rate $\beta_{\alpha,\alpha'}$, which is constructed from the age-structured contact matrix $\mathbf{C}$ and take into account commuting.

Table S2: Offspring PGFs associated with a single step of the reaction phase for each element of the state vector. The parameters η, μ, ϕ correspond to spontaneous transition rates between the disease stages (see Fig. S2). The parameter $\beta_{\alpha,\alpha'}$ is the rate at which infectious α-agents interact and transmit the disease to α'-susceptible individuals.

Element identified by the type σ	Reaction phase PGF $r_\sigma(\boldsymbol{x})$
Latent individuals of category α	$y_{\alpha,1}\eta\Delta t + z_\alpha(1-\eta\Delta t)$
Infectious individuals of category α in the first stage	$\exp\left[\sum_{\alpha'}\beta_{\alpha,\alpha'}(z_{\alpha'}-1)\Delta t\right]\left[y_{\alpha,2}\mu\Delta t + y_{\alpha,1}(1-\mu\Delta t)\right]$
Infectious individuals of category α in the second stage	$\exp\left[\sum_{\alpha'}\beta_{\alpha,\alpha'}(z_{\alpha'}-1)\Delta t\right]\left[w_{\alpha,1}\mu\Delta t + y_{\alpha,2}(1-\mu\Delta t)\right]$
Post-infectious individuals of category α in the first stage	$w_{\alpha,2}\varphi\Delta t + w_{\alpha,1}(1-\varphi\Delta t)$
Post-infectious individuals of category α in the second stage	$\varphi\Delta t + w_{\alpha,2}(1-\varphi\Delta t)$
Exported individuals of category α	v_α
Wastewater detections related to a change of category $\alpha \to \alpha'$	$u_{\alpha,\alpha'}$

Table S3: Offspring PGFs associated with the mobility phase for each element of the state vector. The parameter $m_{\alpha,\alpha'}$ is the probability per day for α-agents to move and become of category α'; the parameter $p_{\alpha,\alpha'}$ is the probability of detection for detectable individuals if they move according to $\alpha \to \alpha'$.

Element identified by the type σ	Mobility phase PGF $M_\sigma(\boldsymbol{x})$
Latent individuals of category α	$\sum_{\alpha'\neq\alpha} m_{\alpha,\alpha'} z_{\alpha'} v_{\alpha'} + m_{\alpha,\alpha} z_\alpha$
Infectious individuals of category α in the first stage	$\sum_{\alpha'\neq\alpha} m_{\alpha,\alpha'} y_{\alpha',1} v_{\alpha'}(1-p_{\alpha,\alpha'}+p_{\alpha,\alpha'}u_{\alpha,\alpha'}) + m_{\alpha,\alpha} y_{\alpha,1}$
Infectious individuals of category α in the second stage	$\sum_{\alpha'\neq\alpha} m_{\alpha,\alpha'} y_{\alpha',2} v_{\alpha'}(1-p_{\alpha,\alpha'}+p_{\alpha,\alpha'}u_{\alpha,\alpha'}) + m_{\alpha,\alpha} y_{\alpha,2}$
Post-infectious individuals of category α in the first stage	$\sum_{\alpha'\neq\alpha} m_{\alpha,\alpha'} w_{\alpha',1}(1-p_{\alpha,\alpha'}+p_{\alpha,\alpha'}u_{\alpha,\alpha'}) + m_{\alpha,\alpha} w_{\alpha,1}$
Post-infectious individuals of category α in the second stage	$\sum_{\alpha'\neq\alpha} m_{\alpha,\alpha'} w_{\alpha',2}(1-p_{\alpha,\alpha'}+p_{\alpha,\alpha'}u_{\alpha,\alpha'}) + m_{\alpha,\alpha} w_{\alpha,2}$
Exported individuals of category α	v_α
Wastewater detections related to a change of category $\alpha \to \alpha'$	$u_{\alpha,\alpha'}$

Considering all these possible transitions, we report in Table S2 the offspring PGF associated to a single step of the reaction phase, $r_\sigma(\boldsymbol{x})$, for each type of node. Disease progression transitions are represented by multinomial PGFs, while disease transmission (for infectious individuals only) is represented by a multivariate Poisson PGF. The multivariate Poisson PGF corresponds to an infinite-size subpopulation approximation for binomial draws used in GLEAM simulations for the infection process. Note that the offspring PGFs for elements of type σ identifying a cumulative number of exported individuals or a cumulative number of wastewater detections at airports are simply the identity PGF, i.e., $f(x) = x$. Indeed, these quantities do not generate new infections or transition to other states, they only serve to keep track of a sum [26].

Mobility phase: air-travel and detection at airports

Each day, latent, infectious, and post-infectious α-agents in location l move to a new subpopulation l' of multi-index α' with probability $m_{\alpha,\alpha'}$ and stay with probability $m_{\alpha,\alpha}$; agents that move and are detectable (infectious or post-infectious) are detected with probability $p_{\alpha,\alpha'} = p_{l,l'}$, calculated in Eq. (4). Similarly to the reaction phase, we report in Table S3 the offspring PGF associated with the mobility phase, $M_\sigma(\boldsymbol{x})$, for each type of node. Except for the types identifying exported individuals and wastewater detections, $M_\sigma(\boldsymbol{x})$ is a multinomial PGF.

Initial conditions

The solution of Eq. (8) takes the form

$$\Psi^t(\boldsymbol{x}) = \Psi^0(\underbrace{\boldsymbol{F}(\boldsymbol{F}(\cdots\boldsymbol{F}(}_{t \text{ times}}\boldsymbol{x})\cdots))) \,. \tag{10}$$

The PGF $\Psi^0(\boldsymbol{x})$ specifies the initial condition. In all cases in this study, we specify a number ℓ and i_1 of initial latent and infectious (I_1) individuals respectively. Their age is randomly selected according to the age distribution of the origin subpopulation l, which we represent by the conditional category distribution $P(\alpha|l)$. The PGF for the initial conditions then takes the form

$$\Psi^0(\boldsymbol{x}) = \left(\sum_\alpha P(\alpha|l) z_\alpha\right)^\ell \left(\sum_\alpha P(\alpha|l) y_{\alpha,1}\right)^{i_1} , \tag{11}$$

It is worth stressing that since Ψ^0 is applied *last* when evaluating Eq. (10), it is computationally inexpensive to test various initial conditions, which we use in this study to vary the origin of the outbreak.

Evaluation of probability distributions and cumulants

For a large number of multi-indices σ, evaluating the full joint distribution $P(\boldsymbol{s}, t)$ is computationally prohibitive. However, it is not our goal: In general, we want to evaluate a marginal or a joint distribution of some *observables*, like d_t, the total number of detections at any sentinels by time t, which can be estimated from the PGF $\Psi^t(\boldsymbol{x})$. For instance, the PGF for the distribution $P(d_t = d)$, is

$$\zeta^t(x) \equiv \sum_d P(d_t = d) x^d = \Psi^t\left[\boldsymbol{A}(x)\right] , \tag{12}$$

where $\boldsymbol{A}(x)$ is a vector where $A_\sigma(x) = x$ if σ identifies any of the cumulative detection at a sentinel for a specific pair of category, $d_{\alpha,\alpha'}$, and $A_\sigma(x) = 1$ otherwise. This allows us to implicitly sum over all possible combinations of $d_{\alpha,\alpha'}$ resulting in a total number of detection d_t. PGFs $\zeta^t(x, y)$ for joint distributions of observables are constructed in similar fashion.

For any observable n_t, we can extract the distribution $P(n_t)$ from its PGF $\zeta^t(x) = \sum_n P(n_t = n) x^n$ using the following identity

$$\begin{aligned} P(n_t = n) &= \frac{1}{n!} \frac{\mathrm{d}^n}{\mathrm{d}x^n} \zeta^t(x) \Big|_{x=0} , \\ &= \frac{1}{2\pi\rho^n} \int_0^{2\pi} \zeta^t\left(\rho e^{i\omega}\right) e^{-i\omega n} \mathrm{d}\omega , \end{aligned} \tag{13}$$

where $0 < \rho < 1$ is a free control parameter. In practice, we use the following discrete Fourier transform approximation (efficiently calculated using Fast Fourier Transform algorithms)

$$P(n_t = n) \approx \frac{1}{k\rho^n} \sum_{j=0}^{k-1} \zeta^t\left(e^{2\pi i j/k}\right) e^{-2\pi i j n/k} . \tag{14}$$

Note that it is possible to bound and control the error committed by choosing k and a suitable ρ value [35], making this approximation exact for all practical purposes. An analogous multidimensional discrete Fourier transform numerical solution is used for distributions of joint observables.

Finally, in some cases, it is more convenient and computationally efficient to extract a few cumulants—mean, variance, etc.—instead of the full distribution. Fortunately, the *cumulant generating function* (CGF) $K^t(x)$ for an observable is directly related to its PGF $\zeta^t(x)$ by the relation $K^t(x) = \ln \zeta^t(e^x)$ [36]. Cumulants are extracted from the CGF using a discrete Fourier transform procedure similar to Eq. (14), which is also directly generalizable to higher dimensions (joint cumulants).

Minimal example: SIR dynamics in two subpopulations

To illustrate the full PGF methodology from end to end, let us consider a simpler, minimal, example of two subpopulations and a single age group. Therefore, we only have two categories $\alpha \in \{1, 2\}$ associated with each

subpopulation. We also consider a simpler compartmental model: individuals are either susceptible, infectious, or recovered; since in our framework we do not track susceptible and recovered individuals, we only need to track i_1 and i_2, the number of infectious individuals in each subpopulation. The probability distribution for the state of the epidemic at time t, $P(i_1, i_2, t)$, is encoded with the PGF

$$\Psi^t(\boldsymbol{x}) = \Psi^t(y_1, y_2) = \sum_{i_1=0}^{\infty} \sum_{i_2=0}^{\infty} P(i_1, i_2, t) y_1^{i_1} y_2^{i_2} \ , \tag{15}$$

where y_1 and y_2 are placeholder variables tracking i_1 and i_2 respectively.

We assume that the epidemic starts at time $t = 0$ with 1 infectious individuals in subpopulation 1. From Eq. 11, this implies $\Psi^0(y_1, y_2) = y_1$. Let us now consider the evolution of the system for a single time step. To simplify the expressions, we use $m = 1$ ($\Delta t = 1$) for the temporal scale of the reaction phase. The offspring PGFs associated with the mobility phase are written as follows

$$\boldsymbol{M}(y_1, y_2) = \begin{bmatrix} M_1(y_1, y_2) \\ M_2(y_1, y_2) \end{bmatrix} = \begin{bmatrix} m_{1,1} y_1 + m_{1,2} y_2 \\ m_{2,1} y_2 + m_{2,2} y_2 \end{bmatrix} = \begin{bmatrix} m_{1,1} & m_{1,2} \\ m_{2,1} & m_{2,2} \end{bmatrix} \begin{bmatrix} y_1 \\ y_2 \end{bmatrix} \ . \tag{16}$$

We interpret $M_1(y_1, y_2) = m_{1,1} y_1 + m_{1,2} y_2$ as follows: an infectious individual in subpopulation 1 has a probability $m_{1,1}$ to stay in subpopulation 1 and a probability $m_{1,2} = 1 - m_{1,1}$ to move to subpopulation 2. A similar reasoning holds for $M_2(y_1, y_2)$.

The offspring PGFs associated with the reaction phase are written as follows

$$\boldsymbol{R}(y_1, y_2) = \begin{bmatrix} R_1(y_1, y_2) \\ R_2(y_1, y_2) \end{bmatrix} = \begin{bmatrix} \exp\{\beta_{1,1}(y_1 - 1)\} \exp\{\beta_{1,2}(y_2 - 1)\}\{\mu + (1 - \mu) y_1\} \\ \exp\{\beta_{2,1}(y_1 - 1)\} \exp\{\beta_{2,2}(y_2 - 1)\}\{\mu + (1 - \mu) y_2\} \end{bmatrix} \ . \tag{17}$$

We interpret $R_1(y_1, y_2)$ as follows: 1) An infectious individual in subpopulation 1 will generate a number of secondary infections in subpopulation 1, distributed according to a Poisson distribution with mean $\beta_{1,1}$, to which corresponds the PGF $\exp\{\beta_{1,1}(y_1 - 1)\}$. 2) If we take into account commuting, i.e., $\beta_{1,2} > 0$, an infectious individual in subpopulation 1 will also generate secondary infections in subpopulation 2, with PGF $\exp\{\beta_{1,2}(y_2 - 1)\}$. 3) An infectious individual in subpopulation 1 will either recover with probability μ or remain infectious with probability $1 - \mu$, resulting in the PGF $\mu + (1 - \mu) y_1$. Since these 3 kinds of events are *independent*, the PGF for the sum is the product of the individual PGFs [25], resulting in the expression for $R_1(y_1, y_2)$. A similar reasoning holds for $R_2(y_1, y_2)$.

Combining the mobility and reaction phases, the offspring PGFs $\boldsymbol{F}(\boldsymbol{x}) = \boldsymbol{M}(\boldsymbol{R}(\boldsymbol{x}))$ for infectious individuals in both subpopulations are

$$\boldsymbol{F}(y_1, y_2) = \begin{bmatrix} F_1(y_1, y_2) \\ F_2(y_1, y_2) \end{bmatrix} = \begin{bmatrix} M_1(R_1(y_1, y_2), R_2(y_1, y_2)) \\ M_2(R_1(y_1, y_2), R_2(y_1, y_2)) \end{bmatrix} = \begin{bmatrix} m_{1,1} & m_{1,2} \\ m_{2,1} & m_{2,2} \end{bmatrix} \begin{bmatrix} R_1(y_1, y_2) \\ R_2(y_1, y_2) \end{bmatrix} \ . \tag{18}$$

Using the recursion in Eq. (8) and the offspring PGFs above, we are able to calculate the PGF for the state of the epidemic at time $t = 1$

$$\Psi^1(y_1, y_2) = \Psi^0(F_1(y_1, y_2), F_2(y_1, y_2)) = F_1(y_1, y_2) = m_{1,1} R_1(y_1, y_2) + m_{1,2} R_2(y_1, y_2) \ . \tag{19}$$

We interpret Eq. (19) as follows: with probability $m_{1,1}$, the index case will stay in the first subpopulation, and generate secondary infections as prescribed by $R_1(y_1, y_2)$, or travel to subpopulation 2 with probability $m_{1,2}$ and generate secondary infections as prescribed by $R_2(y_1, y_2)$.

From $\Psi^1(y_1, y_2)$, we can estimate any distributions of *observables* for the state of the epidemic at time $t = 1$. For instance, if we compose Ψ^1 with $\boldsymbol{A}(x) = [A_1(x), A_2(x)]^\top = [x, x]^\top$ to get the PGF

$$\zeta^1(x) = \Psi^1(x, x) = m_{1,1} R_1(x, x) + m_{1,2} R_2(x, x) \ , \tag{20}$$

then $\zeta^1(x)$ encodes the distribution for the total number of infectious in both subpopulations, which can be recovered numerically through Eq. (14).

Altogether, this minimal example with the SIR model in two subpopulations illustrates the full PGF methodology: We start from a PGF describing the initial conditions, $\Psi^0(\boldsymbol{x})$, we define the vector of offspring PGFs $\boldsymbol{F}(\boldsymbol{x})$, using Eq. (8) we get the PGF for the state of the epidemic at a later time $\Psi^t(\boldsymbol{x})$, and finally we use it to get a PGF for the distribution of an observable $\zeta^t(x)$, like the total number of infectious individuals. For the compartmental model in Fig. S2 and the metapopulation network of GLEAM, the dimension of the PGFs and equations is much larger, but the procedure is exactly the same.

2 Time to first detection for a global wastewater surveillance system at airports

An important quantity introduced in the main text is the time to first detection, t_{fd}, with distribution

$$P(t_{\mathrm{fd}} = t) = P(d_{t-1} < 1, d_t \geq 1) \ . \tag{21}$$

We can simplify the joint distribution on the right-hand side. Note that the statements $A \equiv d_{t-1} < 1$ and $B \equiv d_t \geq 1$ are Boolean random variables. We can write the probability $P(A, B) = P(A) - P(A, \neg B)$. Since $P(\neg A, \neg B) = 0$ because it is impossible, then $P(A, \neg B) = P(\neg B)$. Therefore,

$$P(d_{t-1} < 1, d_t \geq 1) \equiv P(A) - P(\neg B) = P(d_{t-1} < 1) - P(d_t < 1) = P(d_{t-1} = 0) - P(d_t = 0) \ , \tag{22}$$

which is straightforward to evaluate using the PGFs. Let us emphasize that the time to first detection is independent of the wastewater methodology being used (pooled sampling or individual aircraft sampling), in the sense that it does not matter if more than one detectable individual contributed to a positive test at a sentinel. It is also worth highlighting the close connection with the extensive line of work on the *arrival time* of disease in metapopulation networks [37–41].

To complement Fig. 1 in the main text, we show in Fig. S4 the mean time to first detection from all potential sources for the four different levels of detection probability (4%, 8%, 16%, and 32%). We additionally validate in Fig. S5 the PGF solutions with GLEAM simulations for the full distribution of t_{fd} for two epidemic origins. In Fig. S5(A), the PGF prediction accurately reproduces the distribution, with T_{fd}, the mean time to first detection, being within less than 1 standard error (SE) of the simulation estimate. In Fig. S5(B), there are approximately 2 days of difference between the two estimates of T_{fd} (i.e., 3% difference), which is due to finite subpopulation effects not taken into account by the PGFs. Note that Kalemie is a subpopulation for which it takes a long time to detect with this surveillance system and therefore accentuates the discrepancy.

In Fig. 2 of the main text, we present results for T_{fd} aggregated over continents; in Fig. S6, we present a similar same analysis, but aggregating over statistical subregions in Africa and Asia. We again observe broad heterogeneity of the mean time to first detection at this geographical scale in all subregions.

An important surveillance network introduced in the main text is the complete WWSN, where all airports act as surveillance sites. In Fig S7, we show T_{fd} from every potential origin in the world for the complete WWSN. We note the similarity with the global map obtained in Figs. 1. The mean time to first detection is still very heterogeneous, with some locations taking a week and others as much as 100 days before a first detection by the WWSN. To better explain the source of this heterogeneity, in Fig. S8, we show the relation between the probability per day of traveling to an international destination for an individual in each location and T_{fd}. There is a clear negative correlation between the two—a higher probability leads to a faster detection—, but other factors are important. For instance, for some subpopulations, international travel is not directly possible—an individual must first travel to another subpopulation within the same country before moving abroad. In other words, one must take into account additional seeding events through importations or commuting to fully characterize the time to first detection.

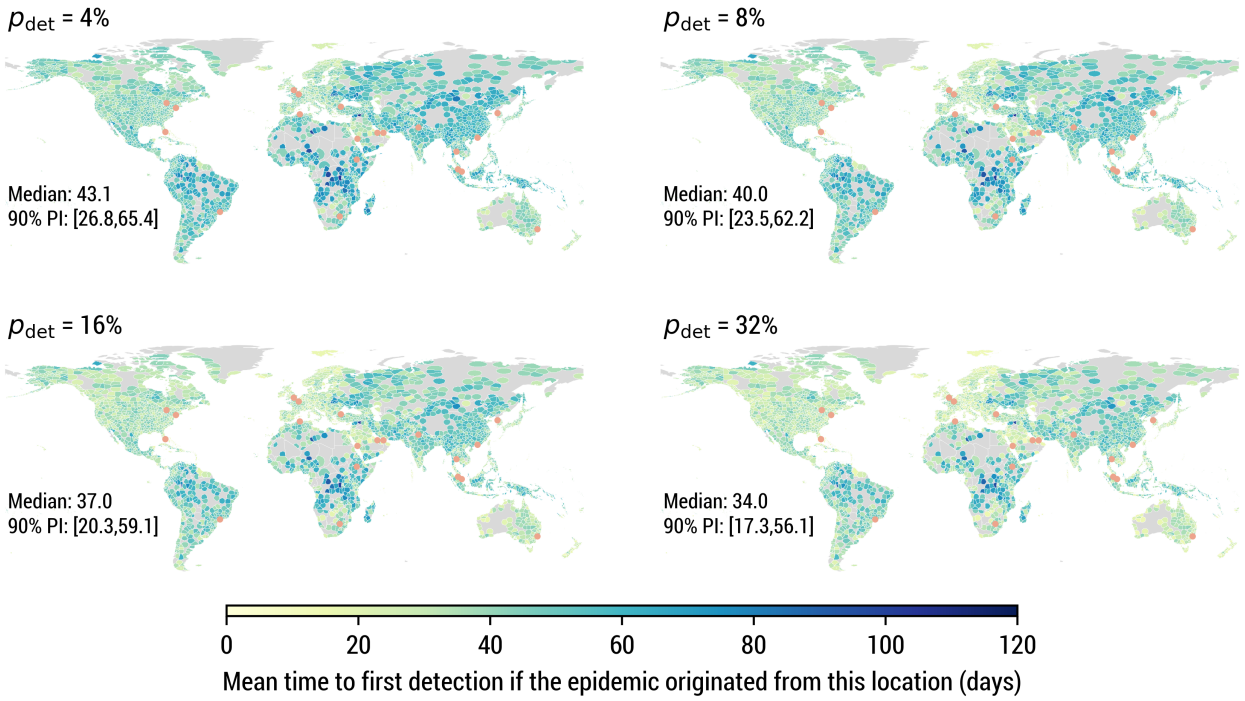

Figure S4: Mean time to first detection using different detection probabilities p_{det} at the sentinels. Otherwise, we use the same WWSN and model parametrization as in Fig. 1. Statistics reported are based on $n = 3244$ subpopulations.

2.1 Variation with the disease natural history

Changing the disease's natural history affects significantly T_{fd}, as can be seen in Fig. 4 in the main text. For the sake of completeness, we also show in Fig. S9 a similar analysis, where instead of varying generation time via the latent period, we do it via the infectious period, keeping the detectable period fixed. We obtain similar results for the mean time to first detection as in Fig. 4.

By changing the generation time or the reproduction number, we ultimately change the growth rate λ of the epidemic—or equivalently the doubling time $T_2 \equiv \ln 2/\lambda$. For the model we consider, the growth rate can be obtained by solving the following implicit nonlinear equation [11]:

$$\mathcal{R}_0 = \lambda T_{\text{inf}} \frac{\left(1 + \frac{\lambda T_{\text{lat}}}{n_{\text{lat}}}\right)^{n_{\text{lat}}}}{\left[1 - \left(1 + \frac{\lambda T_{\text{inf}}}{n_{\text{inf}}}\right)^{-n_{\text{inf}}}\right]} , \tag{23}$$

where n_{lat} and n_{inf} are the numbers of latent and infectious states respectively (here we use $n_{\text{lat}} = 1$ and $n_{\text{inf}} = 2$).

In Fig. 4 of the main text, we show that for all practical purposes, the following relationship holds:

$$\frac{T_{\text{fd}}}{T_2} + \log_2 T_2 \approx \text{const.} \tag{24}$$

Another way to interpret this equation is that changing the doubling time from T_2 to $\hat{T}_2$ ultimately amounts to a linear transformation of the form

$$\hat{T}_{\text{fd}} = a T_{\text{fd}} + b \quad ; \quad a = \left(\frac{\hat{T}_2}{T_2}\right) \quad ; \quad b = \hat{T}_2 \log_2 \left(\frac{T_2}{\hat{T}_2}\right) , \tag{25}$$

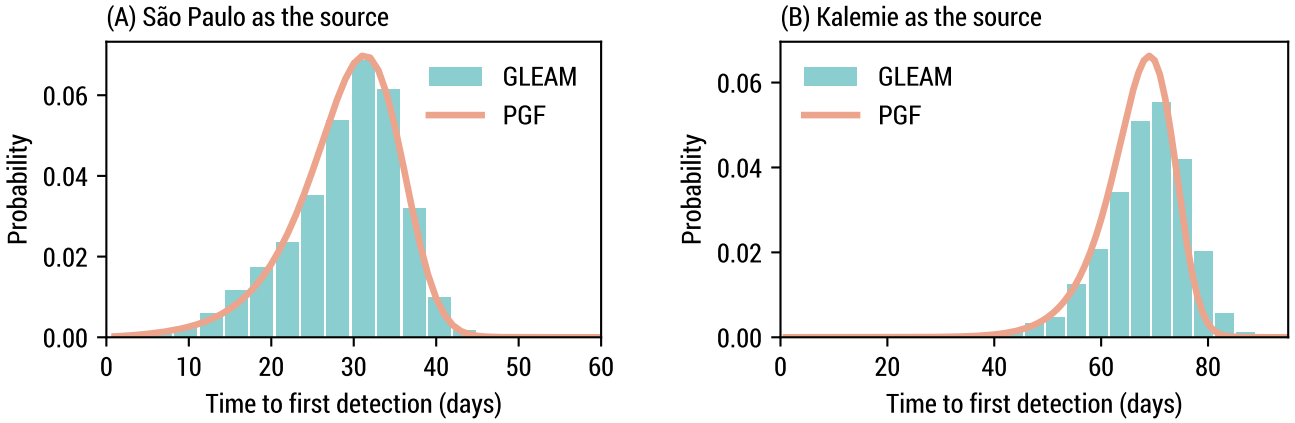

Figure S5: Comparison of the time to first detection. We use the same model, parametrization, and baseline WWSN as in Fig. 1. (A) The epidemic starts in São Paulo. GLEAM estimates are based on 1135 simulation runs. The mean time to first detection is 29.98 (SE, 0.19) days for GLEAM and 29.97 days using the PGFs. (B) The epidemic starts in Kalemie. GLEAM estimates are based on 1590 simulation runs. The mean time to first detection is 68.47 (SE, 0.20) days for GLEAM and 66.46 days using the PGFs.

where $\hat{T}_{\rm fd}$ is the mean time to first detection with doubling time $\hat{T}_2$. This is illustrated in Fig. S10 for all potential origins, when changing the mean generation time or the reproduction number. The Pearson correlation coefficients are very high (>0.99).

To justify Eq. (24), let us rephrase more formally the argument introduced in the main text. If we neglect the stochastic fluctuations of the epidemic, the number of detectable individuals is approximately $D(t) \simeq D_0 e^{\lambda t}$, t days after the beginning of the outbreak. Let us also assume that each day, a detectable individual has some constant probability ω to travel and be detected by the WWSN. In that case, we can approximate the probability of having a first detection on day t as [37]

$$P(t_{\rm fd} = t) \approx [1 - (1-\omega)^{D(t)}] \prod_{t'=1}^{t-1} (1-\omega)^{D(t')} \tag{26}$$

$$\approx \xi e^{\lambda t} \exp\left(-\frac{\xi}{\lambda} e^{\lambda t}\right) , \tag{27}$$

where $\xi = \omega D_0$, and the approximations hold when $\xi/\lambda \ll 1$. Since the probability per day of air travel is very small in general (see Fig. S8), this approximation is almost always valid. We recognize a Gumbel distribution with mean

$$T_{\rm fd} = \frac{1}{\lambda}\left[\ln\left(\frac{\lambda}{\xi}\right) - \gamma\right] , \tag{28}$$

where γ is the Euler–Mascheroni constant. Rearranging the terms and using $\lambda = \ln 2/T_2$, we get

$$\frac{T_{\rm fd}}{T_2} + \log_2 T_2 = \frac{1}{\ln 2}\left(\ln(\ln 2) - \ln \xi - \gamma\right) = \text{const.} , \tag{29}$$

which is identical to Eq. (24).

In Fig. S11, we show that the Gumbel distribution approximates well the distribution for the time to first detection, especially when the initial number of latent and infectious is high in Fig. S11(B). This is due to the fact that the Gumbel approximation neglects the stochastic fluctuations of the epidemic, which are more important when starting with fewer exposed individuals.

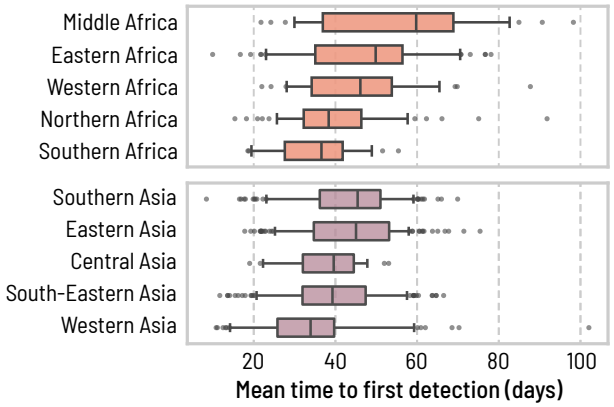

subregion	min	P5	median	mean	P95	max
M. Africa	21.8	28.2	59.8	55.8	84.5	98.3
E. Africa	9.9	23.0	49.9	47.2	70.5	78.1
W. Africa	22.0	28.0	46.1	46.2	67.2	87.7
N. Africa	15.4	24.5	38.4	40.1	58.7	91.8
S. Africa	18.6	19.1	36.6	35.6	50.2	55.4
S. Asia	8.4	23.1	45.4	43.6	59.1	69.9
E. Asia	17.8	24.9	45.0	43.9	58.1	75.4
C. Asia	19.0	22.1	39.6	37.7	48.6	53.0
S.-E. Asia	11.7	20.6	39.3	39.6	57.7	66.5
W. Asia	10.8	14.2	33.9	34.1	59.3	102.1

Figure S6: Heterogeneity of the time to first detection within statistical subregions. We aggregate the mean time to first detection T_{fd} obtained in Fig. 1 over statistical subregions as defined by the United Nations geoscheme in Africa (Middle, $n = 45$; Eastern $n = 121$; Western $n = 52$; Northern $n = 89$; Southern $n = 31$) and Asia (Southern $n = 205$; Eastern $n = 269$; Central $n = 37$; South-Eastern $n = 236$; Western $n = 120$). The center line of the box plot indicates the median, the box covers the interquartile range, the whiskers cover the 90% central prediction interval (P5–P95), and black dots correspond to outliers outside this interval. Numerical values for some of the statistics of the mean time to first detection are reported in the table on the right.

To obtain the Gumbel approximations in Fig. S11, we calculate λ and T_{fd} from our PGF framework, which allows us to fix ξ in Eq. (28). While ξ should not depend on λ, we do find small variations, which also explain the small variations of the approximate invariant quantity in Eq. (24) and in Fig. 4. This is because we treated the detectable individuals $D(t)$ as one homogeneous population with a fixed probability of moving and being detected ω, while in fact it is a heterogeneous group of individuals distributed across a complex metapopulation network.

2.2 Sensitivity analyses

Other aspects of the disease natural history

Aside from the reproduction number and the generation time that directly affect the growth rate, other aspects of the disease's natural history impact the time to first detection, but less significantly so. Here we vary the length of the post-infectious period—thereby changing the detectable period—and the shape of the secondary-infection distribution. In our framework, we do not directly fix the secondary-infection distribution, but rather the secondary-infection distribution per time step. To tune the variance, we replace the multivariate Poisson PGF term in the reaction phase (see Table S2) by the composition of a multinomial and a negative binomial PGF, namely

$$\exp\left[\sum_{\alpha'}\beta_{\alpha,\alpha'}(z_{\alpha'}-1)\Delta t\right] \mapsto \left[1+\frac{\Delta t}{\kappa}\sum_{\alpha'}\beta_{\alpha,\alpha'}(1-z_{\alpha'})\right]^{-\kappa}. \tag{30}$$

This results in the number of secondary infections per time step being distributed according to a negative binomial [42], a generalization of the Poisson distribution. The composition with the multinomial PGF ensures contacts are made according to the age-structured contact matrix. Increasing the overdispersion parameter κ reduces the variance while reducing κ increases the variance; in the limit $\kappa \to \infty$, we recover the multivariate Poisson PGF. It is important to distinguish the overdispersion parameter κ given here, associated to the secondary-infection distribution per time step of duration Δt, versus what one would expect using a negative binomial for the secondary-infection distribution over the whole infectious period.

Another way to communicate the overdispersion in epidemiology is to assess what portion of infections are caused

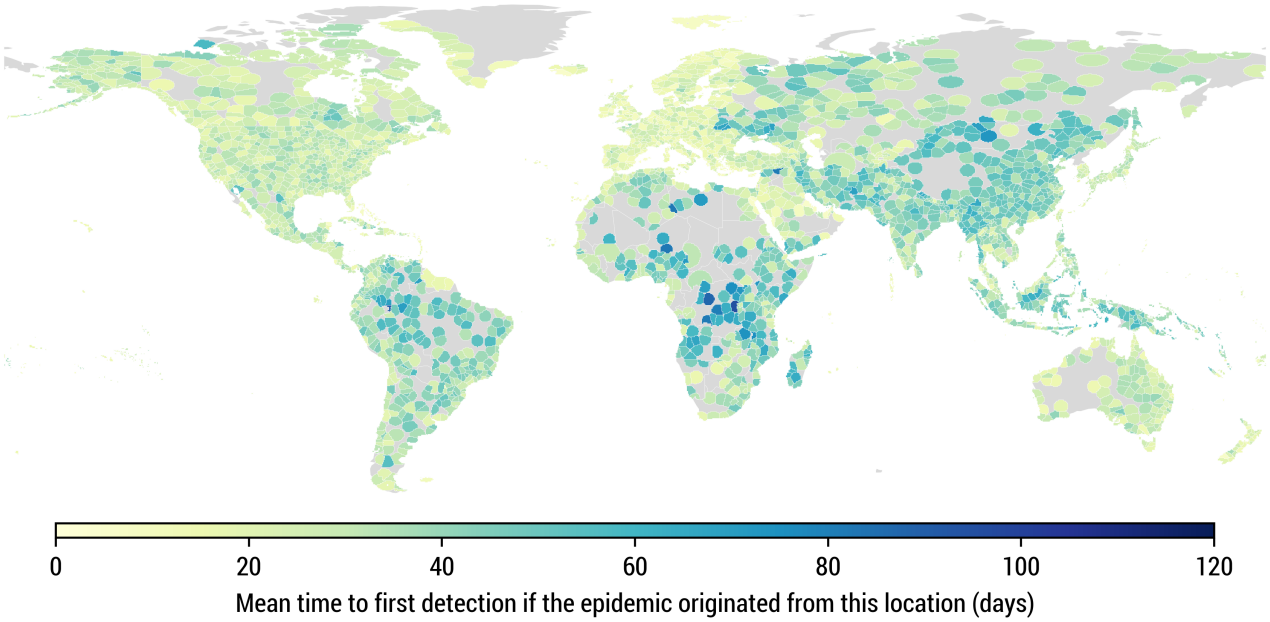

Figure S7: Mean time to first detection with the complete global surveillance network, with a sentinel at every airport. We use the same model parametrization as in Fig. 1.

Table S4: Statistics of the mean time to first detection for various post-infectious periods and overdispersion parameters for the secondary-infection distribution (per time step). The rest of the model parameters and the WWSN are the same as in Fig. 1. We report the median and the 5th and 95th percentile in parentheses ($n = 3244$).

Overdispersion κ		0.01	0.03	0.1	∞
Infections caused by the top 20%		81.9%	66.2%	56.8%	51.3%
Post-Infec. period	5	39.6 (22.4,62.1)	38.3 (21.4,60.7)	37.9 (21.1,60.1)	37.7 (21.0,59.9)
	10	38.9 (21.7,61.4)	37.7 (20.8,60.0)	37.2 (20.4,59.4)	37.0 (20.3,59.1)
	20	38.5 (21.3,60.9)	37.2 (20.4,59.5)	36.8 (20.1,58.9)	36.6 (20.0,58.7)

by the top 20% of infectors [42]. We compile our results in Table S4 for various combinations of post-infectious period and overdispersion parameters. Overall, both have a limited impact on the distribution of T_{fd} for all subpopulations. A broader secondary-infection distribution will mainly affect the beginning of an epidemic—once the outbreak is large enough, the stochastic fluctuations are averaged out. Similar results were obtained in Ref. [6]. The small impact of changing the detectable period (through the post-infectious period) is due to the fact that the number of infectious grows exponentially at the beginning of an epidemic. Consequently, unless the growth rate of the disease is very small, detection at airports should be predominantly caused by newly infectious individuals traveling.

Temporal variation of the traveling patterns

Variation of the air-travel patterns also does not lead to large variations of the global statistics of T_{fd} for all locations, as illustrated in Fig. S12. The median of the distribution for T_{fd} varies from 36 days in the summer to 38 days in the Fall, and the 90% prediction intervals remain relatively stable.

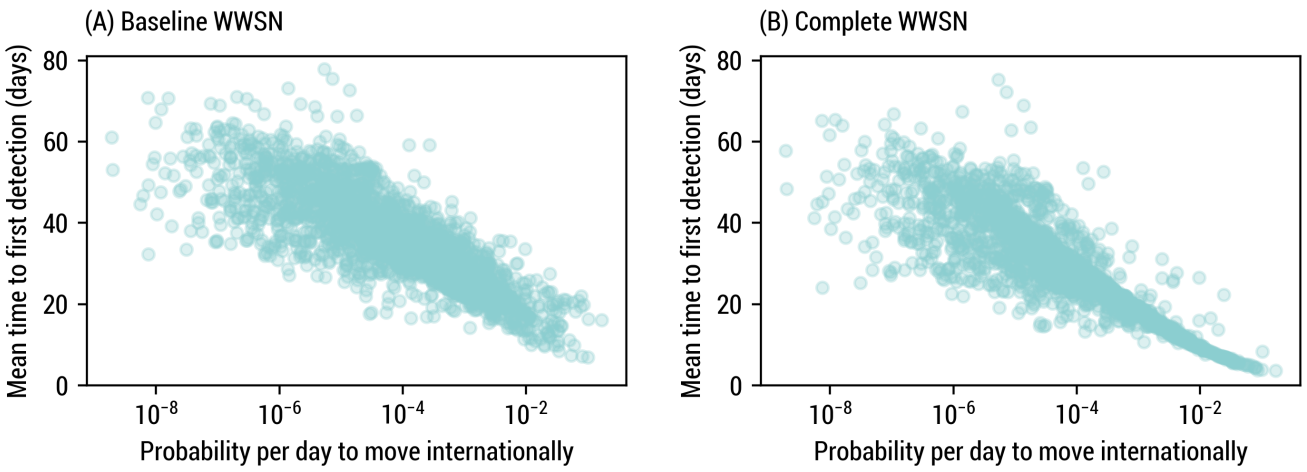

Figure S8: Mean time to first detection for different potential origin, against the probability per day to move internationally from each subpopulation. We only include subpopulations as origin where this probability is larger than zero. We use the same model parametrization as in Fig. 1. (A) We use the same baseline WWSN as in Fig. 1. The Pearson correlation coefficient is -0.810 (90% CI, -0.821 to -0.799; two-sided P value $<10^{-16}$, testing non-correlation) between the mean time to first detection and the logarithm of the probability per day to move internationally ($n = 2509$). (B) We use the complete WWSN, with a sentinel at every airport. The Pearson correlation coefficient is -0.862 (90% CI, -0.870 to -0.853; two-sided P value $<10^{-16}$, testing non-correlation) between the mean time to first detection and the logarithm of the probability per day to move internationally ($n = 2509$).

Heterogeneous detection at sentinel airports

In Fig. S13, we show that the time to first detection is robust to variation of the detection probability across sentinels. Instead of considering a homogeneous detection probability $p_{\rm det}$ at each sentinel, we allow a different probability of detection $p_{{\rm det},\nu}$ for each sentinel $\nu \in \mathcal{S}$ (conventionally, we define $p_{{\rm det},\nu} = 0$ if $\nu \notin \mathcal{S}$). We model this using a beta distribution with mean $\langle p_{\rm det} \rangle = 16\%$ and varying standard deviation $\sigma_{p_{\rm det}}$ in Figs. S13(A) to (C). To account for variable detection probability at each sentinel in our model, we generalize Eq. (4) to

$$p_{l,l'} = \sum_{\mathcal{P}} P(\mathcal{P}|l \to l') \left[1 - \prod_{\nu \in \mathcal{P}} (1 - p_{{\rm det},\nu}) \right] , \tag{31}$$

for the detection probability of a detectable individual traveling from l to l', where $\mathcal{P} = \nu_1 \to \nu_2 \to \cdots \to \nu_k$ is a potential sequence of airports connecting the two locations.

Even in the case of very heterogeneous detection probabilities ($\sigma_{p_{\rm det}} = 10\%$), the mean time to first detection from all sources is highly correlated with the homogeneous case, as seen in Fig. S13(F). The geographical variation of the mean time to first detection in Fig. S13(G) is also very similar to the homogeneous case in Fig. 1.

2.3 Optimization of the time to first detection

As illustrated in the main text, ranking airports based on their international inbound passenger volume is a simple, yet effective heuristic to minimize the time to first detection. To further support this point, we present in Fig. S14 an analysis of the mean time to first detection, considering a modified baseline WWSN where instead of systematically selecting the busiest international hubs, we select a combination of busiest and smaller airports in each World Health Organization region. While the detection from a few potential sources is enhanced, overall, the mean time to first detection is longer when discarding large hubs. This reinforces the crucial role of large international hubs in the dissemination of infectious diseases.

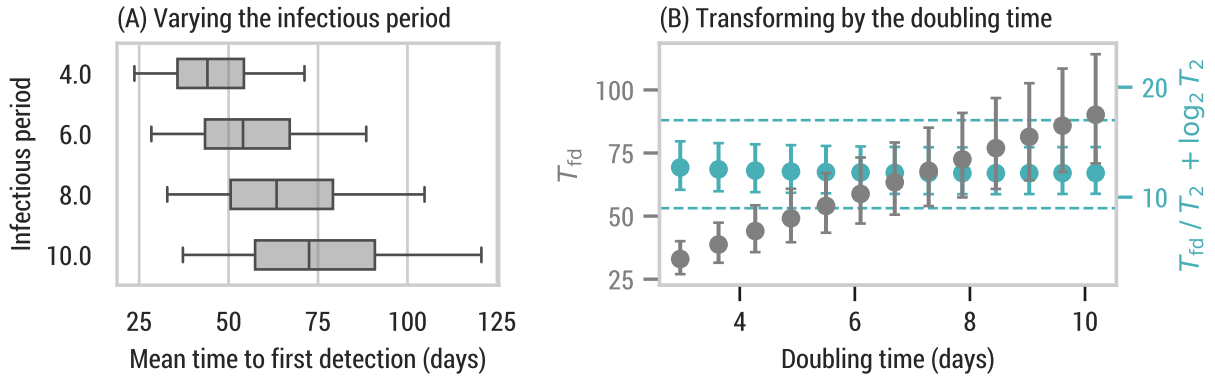

Figure S9: Impact on the mean time to first detection of varying the generation time via the infectious period instead of the latent period. We keep the detectable period fixed to 15 days by also changing the post-infectious detectable period as $T_{\text{post}} = T_{\text{det}} - T_{\text{inf}}$. Otherwise, we use the same WWSN and parametrization as in Fig. 1. All prediction intervals are obtained from $n = 3244$ subpopulations. (A) The center line of the box plot indicates the median, the box covers the interquartile range and the whiskers cover the 90% central prediction interval; the outliers outside the interval are not shown. (B) Circles indicate the median and the error bars cover the interquartile range. The dashed lines are there to guide the eyes. We vary the infectious period between 2 and 14 days, resulting in doubling times between 3 and 10.2 days.

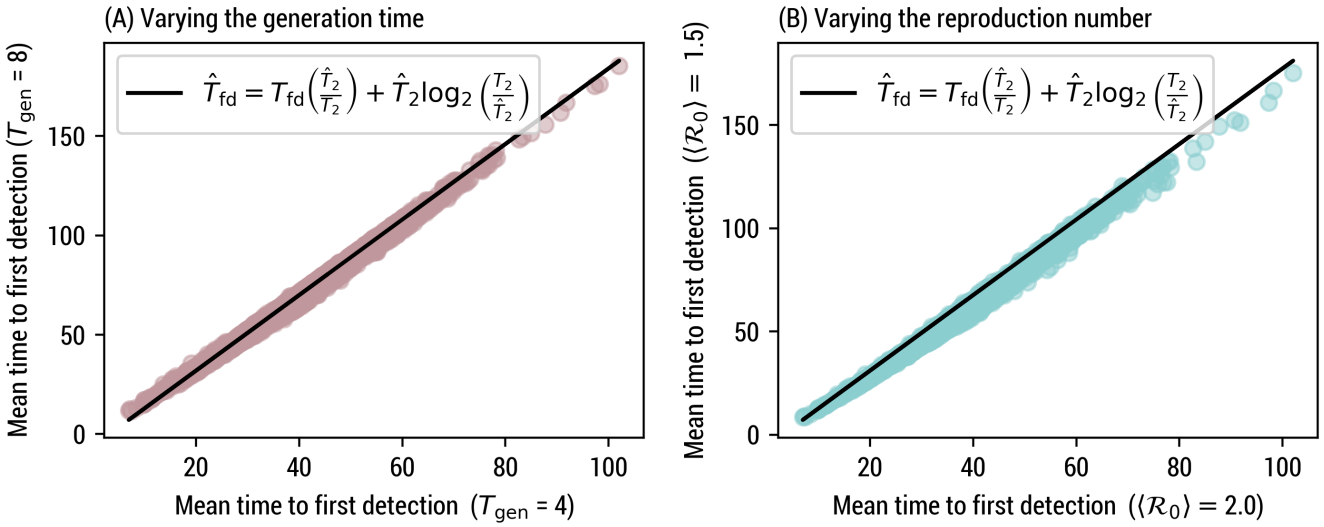

Figure S10: Linear transformation of the mean time to first detection for varying natural disease history. We use the same WWSN as in Fig. 1. The detection probability is 16% and the detectable period is 12.7 days. (A) The mean reproduction number is fixed $\langle \mathcal{R}_0 \rangle = 2$, and the mean generation time varies. The Pearson correlation coefficient is 0.997 with a two-sided P value $<10^{-16}$ ($n = 3244$), testing non-correlation. (B) The mean generation time is fixed $T_{\text{gen}} = 4$, and the reproduction number varies. The Pearson correlation coefficient is 0.996 with a two-sided P value $<10^{-16}$ ($n = 3244$), testing non-correlation.

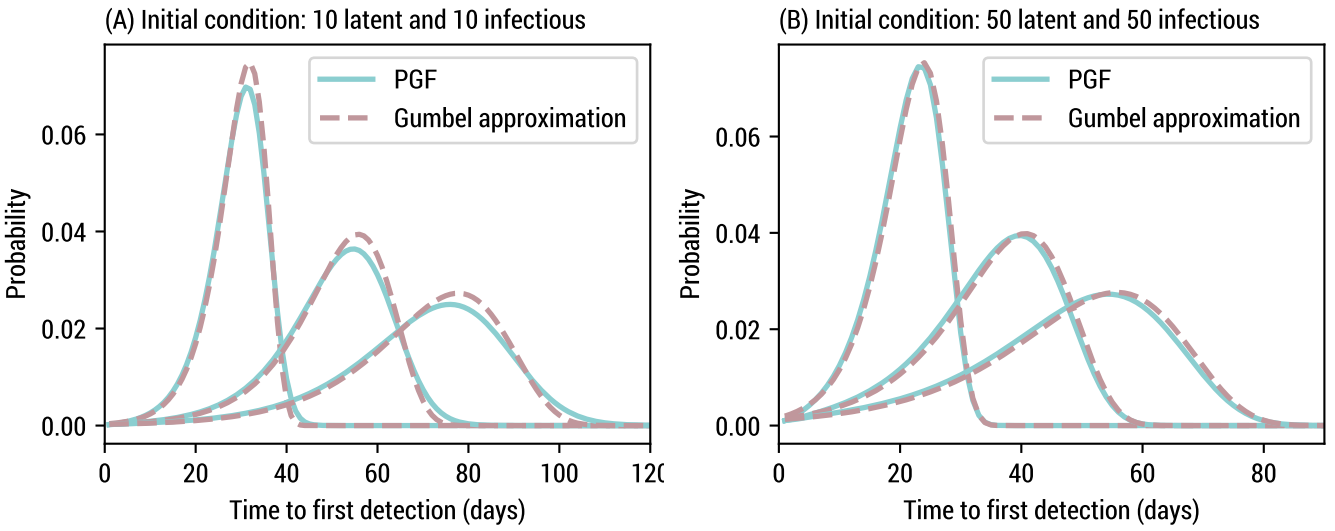

Figure S11: Approximation of the time to first detection using a Gumbel distribution. We use the same WWSN as in Fig. 1 and, unless specified, the same parametrization. We focus on an epidemic originating in São Paulo. We show the results for mean generation times of 4, 8, and 12 days. We consider two initial conditions: (A) 10 latent and 10 infectious individuals and (B) 50 latent and 50 infectious individuals.

In the Methods section of the main text, we introduce a more sophisticated greedy optimization scheme to minimize the mean time to first detection, averaged over all subpopulations as a potential source

$$\Phi(\mathcal{S}) = \sum_{l} P(l) T_{\mathrm{fd}}(\mathcal{S}, l) \ , \tag{32}$$

with probability $P(l)$ of being the source. In the second step of the optimization procedure, it requires the evaluation of $\Phi(\mathcal{S} \cup \{\nu\})$ for each airport $\nu \notin \mathcal{S}$ to assess the reduction in time to first detection associated with adding ν as a sentinel. However, evaluating $\Phi(\mathcal{S} \cup \{\nu\})$ for each new potential sentinel is computationally expensive.

Instead, we use an approximation for each $T_{\mathrm{fd}}(\mathcal{S}, l)$ hinging on two assumptions. First, we assume the full distribution of the time to first detection from each source subpopulation l is well-described by a Gumbel distribution—which is validated in Fig. S11. Second, we assume that the detection at all sentinels $\nu \in \mathcal{S}$ are independent processes. From these assumptions, we can leverage the following identity [37]

$$\exp\left(-\lambda T_{\mathrm{fd}}(\mathcal{S}, l)\right) = \sum_{\nu \in \mathcal{S}} \exp\left(-\lambda T_{\mathrm{fd}}(\{\nu\}, l)\right) \ . \tag{33}$$

This allows us to efficiently estimate $T_{\mathrm{fd}}(\mathcal{S}, l)$ from the individual $T_{\mathrm{fd}}(\{\nu\}, l)$ for all $\nu \in \mathcal{S}$. Figure S15 validates the accuracy of the approximation.

Submodularity proof

In the context of the approximation provided by Eq. (33), we want to show that $-\Phi(\mathcal{S})$ is a monotone submodular set function. Since $-\Phi(\mathcal{S})$ is a positive linear combination of $-T_{\mathrm{fd}}(\mathcal{S}, l)$ for each potential source l, it suffices to show that $-T_{\mathrm{fd}}(\mathcal{S}, l)$ is a monotone submodular set function for all l [44].

We define the set of all potential sentinels as Ω. Let us also simplify the notation by writing $\tau(B) \equiv T_{\mathrm{fd}}(B, l)$ and $\tau(b) \equiv T_{\mathrm{fd}}(\{b\}, l)$ for the mean time to first detection for every set of sentinels $B \subseteq \Omega$ and every sentinel b respectively[1]. Note that $\tau : 2^{\Omega} \to \mathbb{R}^{+}$ is a set function, where 2^{Ω} is the set of all subsets of Ω

[1]The ensuing results are general for all epidemic source l and therefore we drop the index to simplify the notation.

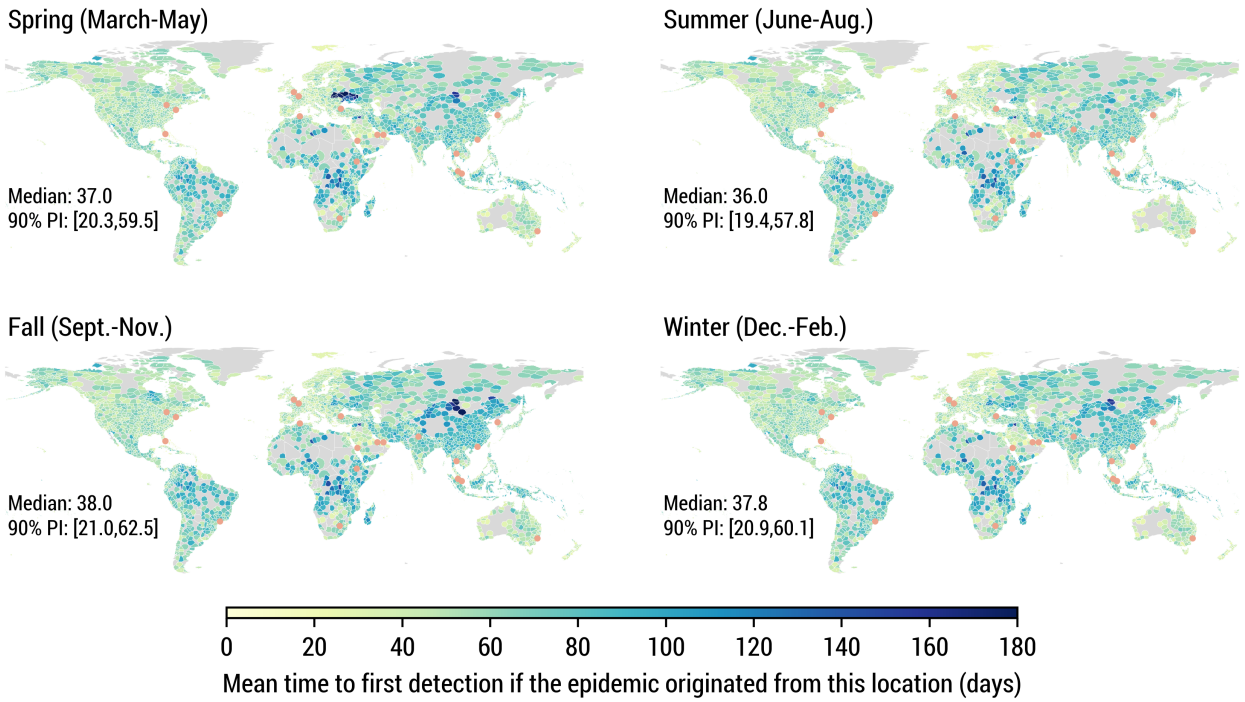

Figure S12: Mean time to first detection using different air-travel mobility networks associated with different seasons. We use the same WWSN and model parametrization as in Fig. 1. Statistics reported are based on $n = 3244$ subpopulations.

Lemma 1. *τ and $-\tau$ are monotone functions, i.e., $\tau(B) \leq \tau(A) \iff -\tau(B) \geq -\tau(A)$ for $A \subseteq B$.*

Proof. Let us define $C \equiv A \cap B$. From Eq. (33), we have

$$e^{-\lambda\tau(B)} = e^{-\lambda\tau(A)} + e^{-\lambda\tau(C)} \geq e^{-\lambda\tau(A)} , \tag{34}$$

where $\lambda > 0$. Taking the logarithm on both sides and dividing by λ, this implies $-\tau(B) \geq -\tau(A)$. □

Definition 1. *Let Ω be a finite set and $f : 2^{\Omega} \to \mathbb{R}$ a set function. The function f is submodular if for two subsets $A, B \subseteq \Omega$ with $A \subseteq B$ and $e \in \Omega \setminus B$, we have $f(A \cup \{e\}) - f(A) \geq f(B \cup \{e\}) - f(B)$ [44].*

Theorem 1. *The function $-\tau$ is monotone and submodular.*

Proof. The function $-\tau$ is monotone from lemma 1. Let us consider two sets A and B such that $A \subseteq B \subseteq \Omega$, $C \equiv B \setminus A$, and an element $e \in \Omega \setminus B$. Using Eq. (33), we have

$$\begin{aligned} e^{-\lambda\tau(B\cup\{e\})} &= e^{-\lambda\tau(B)} + e^{-\lambda\tau(e)} , \\ &= e^{-\lambda\tau(A)} + e^{-\lambda\tau(C)} + e^{-\lambda\tau(e)} , \end{aligned}$$

where $\lambda > 0$. Dividing both sides by $e^{-\lambda\tau(B)}$ and applying again Eq. (33), we find

$$e^{-\lambda[\tau(B\cup\{e\})-\tau(B)]} = \frac{e^{-\lambda\tau(A\cup\{e\})} + e^{-\lambda\tau(C)}}{e^{-\lambda\tau(A)} + e^{-\lambda\tau(C)}} \leq e^{-\lambda[\tau(A\cup\{e\})-\tau(A)]} , \tag{35}$$

where the inequality holds if and only if $\tau(A \cup \{e\}) \leq \tau(A)$, which is true from lemma 1, but also more intuitively because adding sentinels can only reduce the time to first detection. Taking the logarithm on both sides of Eq. (35)

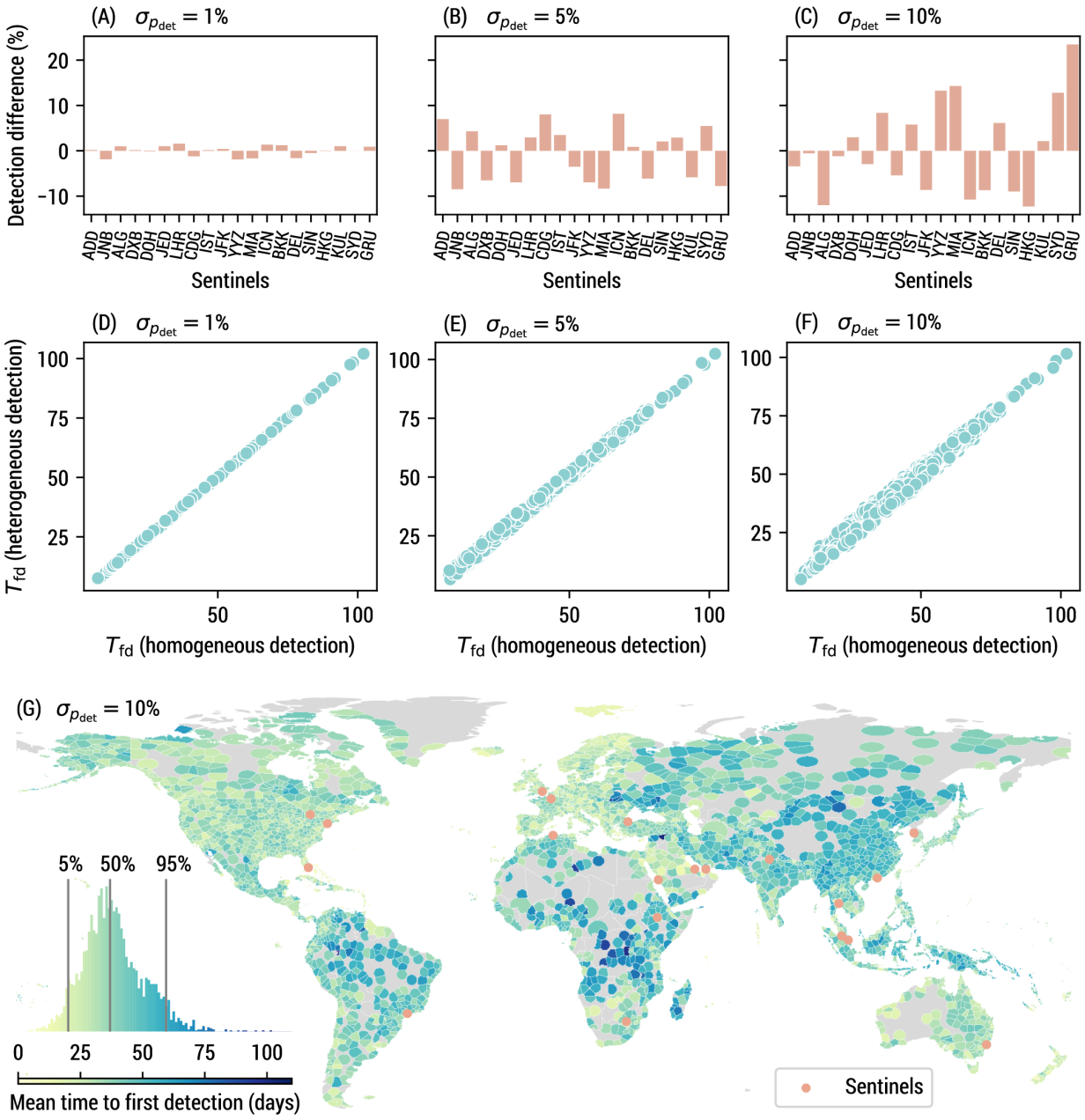

Figure S13: Impact on the mean time to first detection of considering a heterogeneous detection probability at different sentinels. We use the same WWSN and model parametrization as in Fig. 1, but instead of a homogeneous detection probability $p_{\mathrm{det}} = 16\%$, for each sentinel ν we draw a detection probability $p_{\mathrm{det},\nu}$ from beta distribution with mean $\langle p_{\mathrm{det}} \rangle = 16\%$ and varying standard deviation $\sigma_{p_{\mathrm{det}}}$. (A)-(C) Difference between $p_{\mathrm{det},\nu}$ and $\langle p_{\mathrm{det}} \rangle = 16\%$ for each sentinel identified by their IATA code [43]. (D)-(F) Comparison of the mean time to first detection from all potential sources, between the homogeneous and heterogeneous cases. The Pearson correlation coefficient is (D) $>$ 0.999, (E) 0.997, (F) 0.993, and the two-sided P value is $<10^{-16}$ in all cases ($n = 3244$), testing non-correlation. (G) Mean time to first detection for the $\sigma_{p_{\mathrm{det}}} = 10\%$ case.

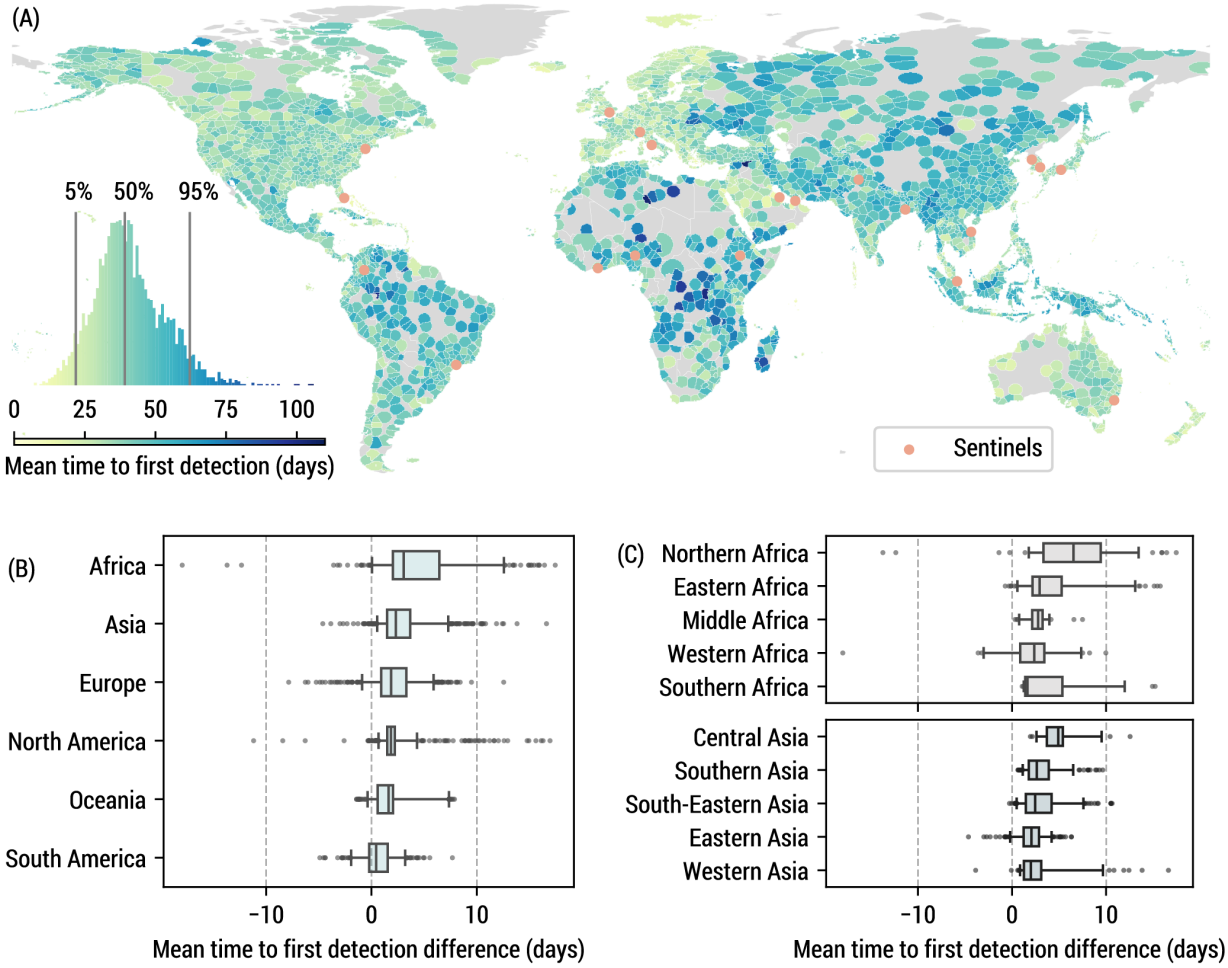

Figure S14: Mean time to first detection with a modified baseline surveillance network, where instead of selecting the three busiest airports in each World Health Organization region, we select the 1st, 10th, and 20th airports ranked by volume of inbound international passengers. We still use the busiest international airports for the two additional sites in South America and Oceania. We use the same model parametrization as in Fig. 1. (A) Mean time to first detection from all potential origins. (B) We aggregate the mean time to first detection over continents (S. America, $n = 297$; Africa $n = 338$; Asia $n = 867$; N. America $n = 854$; Europe $n = 596$; Oceania $n = 292$). (C) We aggregate the mean time to first detection over statistical subregions as defined by the United Nations geoscheme in Africa (Middle, $n = 45$; Eastern $n = 121$; Western $n = 52$; Northern $n = 89$; Southern $n = 31$) and Asia (Southern $n = 205$; Eastern $n = 269$; Central $n = 37$; South-Eastern $n = 236$; Western $n = 120$). (B)-(C) The center line of the box plot indicates the median, the box covers the interquartile range, the whiskers cover the 90% central prediction interval (P5–P95), and black dots correspond to outliers outside this interval.

and dividing by λ, we arrive at

$$-\tau(B \cup \{e\}) + \tau(B) \leq -\tau(A \cup \{e\}) + \tau(A) \,. \tag{36}$$

From definition 1, this implies that $-\tau$ is a submodular set function. □

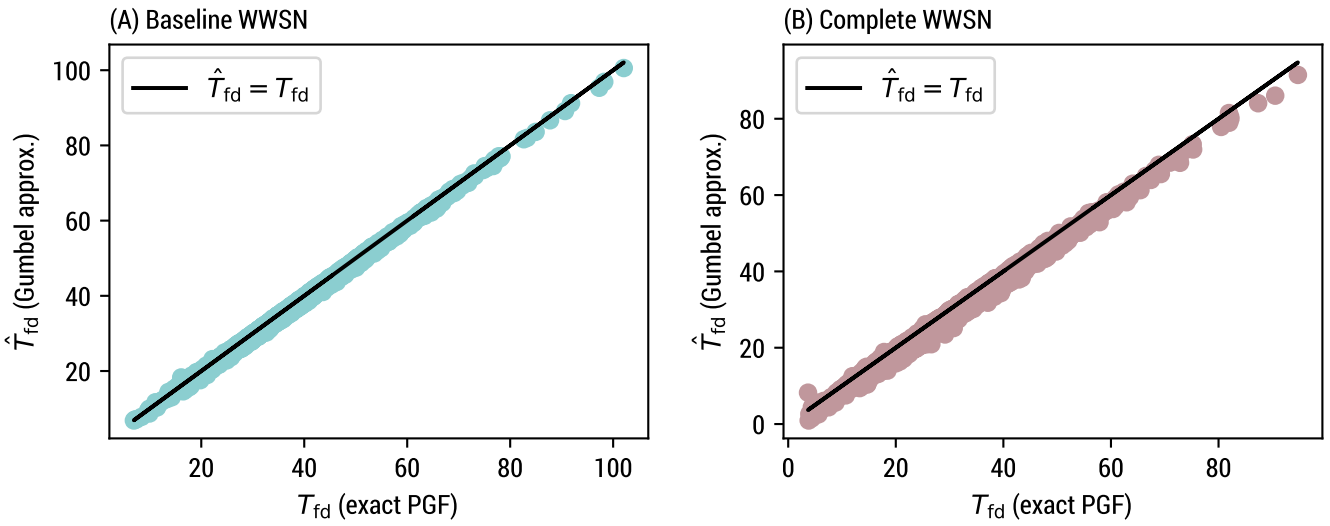

Figure S15: Comparison of the exact PGF calculation and the Gumbel approximation provided by Eq. (33) for the mean time to first detection, considering each of the 3200+ subpopulations as the origin. We use the same model parametrization as in Fig. 1. (A) We use the baseline WWSN. The Pearson correlation coefficient is > 0.999 with a two-sided P value $<10^{-16}$ ($n = 3244$), testing non-correlation. (B) We use the complete WWSN. The Pearson correlation coefficient is 0.997 with a two-sided P value $<10^{-16}$ ($n = 3244$), testing non-correlation.

3 Additional performance metrics

Our analysis primarily focused on time to first detection, but other metrics are important to assess the potential effectiveness of an outbreak response. In Fig. 3 of the main text, we provide modeling estimates for the outbreak size in the country of origin and the number of infections already dispersed internationally at the time of first detection. We use GLEAM stochastic simulations (100 per origin) for 16 different subpopulations as the source of the epidemic, all identified in Fig. S16. We reused the 4 origins of Fig. 1 (Geneva, São Paulo, Kotabaru, and Kalemie) along with 12 other subpopulations sampled at random, ensuring diversity for the time to first detection and sufficient geographical dispersion. Summary statistics for the simulation results are provided in Table S5. Note that the number of internationally dispersed infections—corresponding to international importations of latent or infectious individuals—can be zero at the time of first detection because of traveling post-infectious (but detectable) individuals.

4 Retrospective counterfactual scenarios

4.1 SARS-CoV-2 Alpha variant emergence

In the main text, we present the results of a counterfactual scenario where we would have had a global WWSN to track the international dissemination of the SARS-CoV-2 Alpha (B.1.1.7) variant. We utilize air-travel data from September 2020 to November 2020, along with the baseline WWSN of 20 sentinels (see Table S6).

This variant was first identified by health authorities in the United Kingdom and retrospective analyses trace the first identified case in Kent, South East England, on September 20, 2020 [45]. According to data published by the United Kingdom government [46], the effective reproduction number for SARS-CoV-2 between September 11 and October 30, 2020, was between 1.1 and 1.4 (90% CI) in both London and South East England. The Alpha variant was found to be more transmissible, with an estimated increased reproduction number ranging from 40 to 100% [45,

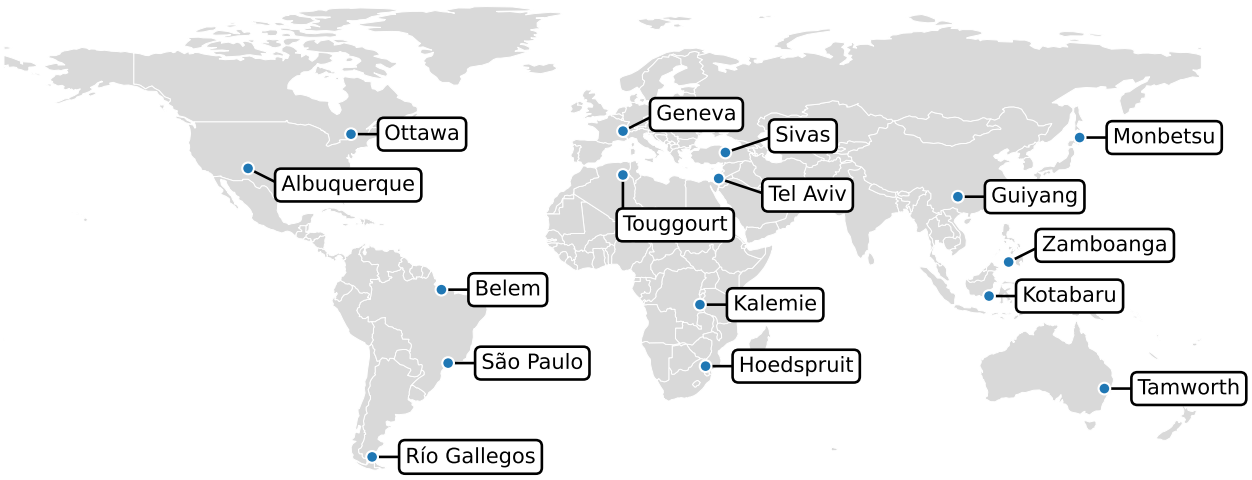

Figure S16: Epidemic origins chosen to estimate additional performance metrics with GLEAM simulations in Fig. 3.

47, 48]. In this counterfactual study, we considered a value of $\mathcal{R}_{\text{eff}}^{\text{alpha}} = 1.7$ for the Alpha variant, on the lower side of available estimates, equivalent to having an effective reproduction number of $\mathcal{R}_{\text{eff}}^{\text{ws}} = 1.1$ for the wild strain and an increased transmissibility of 55%. Since approximately 5% of positive cases were sequenced at the source [45], we considered an initial cluster of 20 infectious and 20 latent individuals on September 15. The generation time is kept fixed at 6.5 days, with a latency period of 4.5 days.

Distributions for the time to first detection in Fig. 6A are calculated using the PGF methodology and are not influenced by the wastewater sampling scheme. The geolocalization of the source (Fig. 6B) and the parameter inference (Fig. 6C), however, require us to transform distributions for the number detections to account for wastewater pool sampling at sentinel sites.

Distribution for the cumulative number of detections by a WWSN

Our PGF methodology allows us to estimate $P(d_t = d)$, the distribution for the cumulative number of detections at time t by the WWSN. However, as defined, all detectable agents traveling through a screened route could contribute to d_t *independently*. While this can be a reasonable assumption for individual testing, this is not the case for wastewater sampling, where it is not usually feasible to identify precisely the number of detectable individuals in an aircraft—we only get a binary *yes* or *no* answer to whether or not the pathogen was detected. Depending on how the testing is performed—on individual aircraft, or pooled sampling of multiple aircraft at a triturator—we would obtain different results for the cumulative number of detections.

We assume the pooled testing of all aircraft within a day at each sentinel airport. To take into account the potential copresence on the same day of detectable individuals traveling to the same destination, we need to define the probability $P(\tilde{d}|d)$, where $\tilde{d}$ represents the cumulative "wastewater" detections and d the cumulative "individual" detections we would obtain if we were able to detect each individual independently. Then we get the adjusted distribution

$$P(\tilde{d}) = \sum_{d} P(\tilde{d}|d)P(d) \ . \tag{37}$$

We evaluate $P(\tilde{d}|d)$ by first characterizing $q_{\nu,t}$, the relative probability an individual detection happens at sentinel ν and at time t. In general, $q_{\nu,t} \propto \langle d^*_{\nu,t} \rangle$, where $\langle d^*_{\nu,t} \rangle$ is the mean number of individual detections at sentinel ν and *incident* on time t—not the cumulative detections. The ratio $\langle d^*_{\nu,t} \rangle / \langle d^*_{\nu',t} \rangle$ is very stable in the early phase of

Table S5: Summary statistics for the outbreak size in the country of origin and the number of infections disseminated internationally at the time of first detection. For each epidemic origin, we report results for $n = 100$ simulations. P5 and P95 correspond to the 5th and 95th percentiles respectively.

	Source country outbreak size				International dissemination			
Origin	P5	median	mean	P95	P5	median	mean	P95
Geneva	78.4	518.0	734.2	2316.0	4.0	31.5	44.5	121.1
Tel Aviv	107.9	1417.5	2019.7	5915.4	2.0	20.5	29.6	77.0
Ottawa	1058.4	12049.0	15147.3	41843.6	2.0	30.0	42.2	129.1
São Paulo	993.2	12969.0	20946.4	52916.4	2.0	15.0	21.4	60.1
Albuquerque	2728.8	14847.0	20898.8	55591.9	1.0	17.0	27.4	81.4
Tamworth	1215.6	15766.5	19328.1	43192.3	2.0	13.5	19.2	56.0
Hoedspruit	7775.8	68722.5	87259.1	199986.6	1.0	9.5	12.1	32.0
Monbetsu	5297.2	29462.0	31424.2	66446.1	0.0	8.0	11.0	27.6
Río Gallegos	6988.4	31014.5	32105.8	65904.1	3.0	21.0	28.4	76.2
Zamboanga	7271.6	64520.0	83902.4	212207.8	1.0	9.5	12.6	35.0
Sivas	10194.1	86696.0	118694.5	311541.3	5.0	27.5	48.1	148.1
Guiyang	25848.3	167158.0	230677.2	805698.5	0.0	11.0	15.2	44.1
Belem	17910.3	177084.5	256976.2	692033.9	2.0	28.0	37.0	90.3
Touggourt	27902.6	180264.0	181945.0	401637.9	0.0	8.5	13.0	42.2
Kotabaru	58195.2	328464.0	344369.7	683204.4	1.0	8.5	12.2	37.0
Kalemie	542712.7	1198554.0	1354666.4	2533491.4	46.0	89.5	88.1	126.1

an outbreak for any pair of airports (ν,ν'). Therefore, $\langle d^*_{\nu,t} \rangle \sim A(\nu)e^{\lambda t}$, where λ is the growth rate at the source and $A(\nu)$ is the relative propensity of detection at each sentinel airports in the early phase. After normalization, we encapsulate all probabilities in a vector $\boldsymbol{q}$. Secondly, we assume that the number of *incident* detections for each sentinel and day $d^*_{\nu,t}$ ($\boldsymbol{d}^*$ in vector format) is distributed according to a multinomial $P(\boldsymbol{d}^*)$ with parameters d (the sum of all $\boldsymbol{d}^*$) and $\boldsymbol{q}$. The total number of *wasterwater* detections corresponds to the number of nonzero counts in $\boldsymbol{d}^*$, and thus $P(\tilde{d}|d)$ is obtained by summing $P(\boldsymbol{d}^*)$ over all configurations such that there are a total of $\tilde{d}$ nonzero counts. While this is technically a difficult combinatorial task, this can be carried out efficiently numerically (see Ref. [49]).

In Fig. S17(A), we show examples of time series for the cumulative number of detections at all sentinels of the WWSN generated by GLEAM. In Fig. S17(B), we illustrate the importance of accounting for wastewater pooled sampling when the number of detections is sufficiently large; the number of wastewater detections is effectively reduced due to the copresence of detectable individuals transiting through as sentinel during the same day.

Geolocalization of the source

Even without information about which flight paths led to detections, it is possible to recover information about the location of the source of an epidemic. Indeed, we can construct a likelihood $P(\tilde{\boldsymbol{d}}|\text{source} = l) \equiv P(\tilde{\boldsymbol{d}}|l)$ for the probability to have observed the wastewater detections $\tilde{\boldsymbol{d}} = (\tilde{d}_\nu)_{\nu\in\mathcal{S}}$ at the sentinel airports.

First, let us ignore wastewater pool sampling and consider individual detections $\boldsymbol{d} = (d_\nu)_{\nu\in\mathcal{S}}$ and the associated likelihood function $P(\boldsymbol{d}|l)$. Then $P(\boldsymbol{d}|l)$ can be modeled by a multinomial distribution with parameter $d = \sum_\nu d_\nu$ and probability vector $\boldsymbol{q} = (q_\nu)_{\nu\in\mathcal{S}}$, where $q_\nu \propto \langle d_\nu \rangle$, the expected number of detections at sentinel ν when we have d detections. In practice, we approximate q_ν by the expected number of detections at each sentinel when we have a first detection.

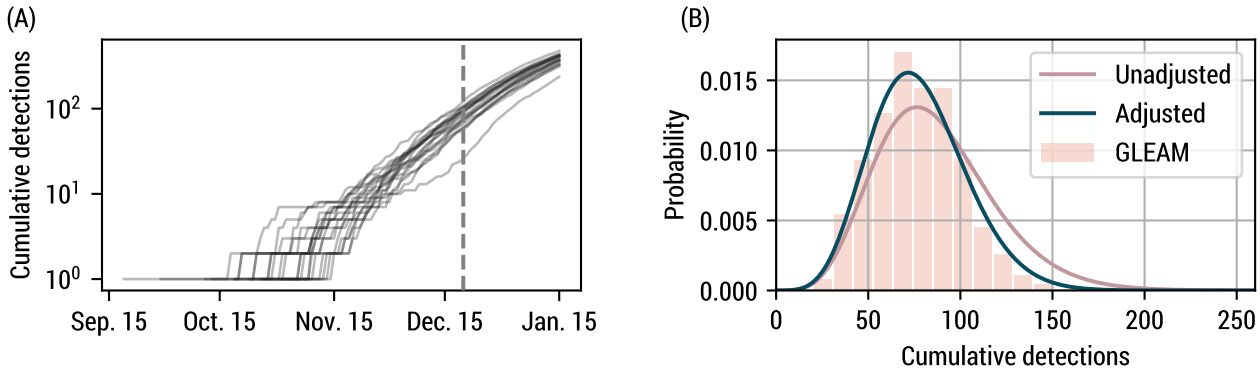

Figure S17: Cumulative number of wastewater detections for the Alpha variant counterfactual study. (A) Example of 20 detection time series from GLEAM simulations. The vertical dashed line indicates December 20, 2020. (B) Distribution for the cumulative number of detections on December 20, 2020, from 1250 GLEAM simulations and the PGF methodology, with and without adjustment for wastewater pool sampling.

To account for wastewater pool sampling, we transform the likelihood as

$$P(\tilde{\boldsymbol{d}}|l) = \sum_{\boldsymbol{d}} P(\tilde{\boldsymbol{d}}, \boldsymbol{d}|l) = \sum_{\boldsymbol{d}} P(\tilde{\boldsymbol{d}}|\boldsymbol{d}, l) P(\boldsymbol{d}|l) \ . \tag{38}$$

Assuming that $P(\tilde{\boldsymbol{d}}|\boldsymbol{d}, l)$ is concentrated around its mean, we can use the following approximation

$$P(\tilde{\boldsymbol{d}}|l) \approx \sum_{\boldsymbol{d}} \delta_{\boldsymbol{d},\boldsymbol{b}} P(\boldsymbol{d}|l) = P(\boldsymbol{b}|l) \ , \tag{39}$$

where $\boldsymbol{b}$ is the expected number of "individual detections" given the observed pooled wastewater detections $\tilde{\boldsymbol{d}}$, rounded to the nearest integer.

Using the likelihood in Eq. (39), we compute the following posterior distribution for the source

$$P(l|\tilde{\boldsymbol{d}}) \propto P(\tilde{\boldsymbol{d}}|l) P(l) \ , \tag{40}$$

where $P(l)$ is a prior distribution on the source location. In this work, we consider a uniform prior $P(l) = \text{const}$. In Fig. S18, we show this posterior distribution for at least 10 wastewater detections, averaged over 1250 simulations. We see that most of the posterior density is concentrated in Europe, and especially in the United Kingdom. The same simulations and posterior distributions are used to assess the geolocalization capacities of a WWSN in Fig. 6, as detections accumulate at the sentinels.

Characterization of the growth dynamics

The time series of cumulative detections can also be utilized to estimate key epidemic parameters. For generic parameter inference, we use the following approach. Given the observed cumulative number of wastewater detections $\tilde{d}$ and $\tilde{d}'$ at different time t and t', we calculate the posterior distribution over $\boldsymbol{\theta}$ (the parameters) using

$$P(\boldsymbol{\theta}|\tilde{d}', \tilde{d}) \propto P(\tilde{d}', \tilde{d}|\boldsymbol{\theta}) P(\boldsymbol{\theta}) \ . \tag{41}$$

To compute more efficiently the joint likelihood $P(\tilde{d}', \tilde{d}|\boldsymbol{\theta})$, we evaluate the joint cumulants from the CGF and employ the method of moments with a negative multinomial distribution.

In Fig. 6C of the main text, we jointly infer the epidemic start date and the increased transmissibility of the Alpha variant with respect to the SARS-CoV-2 wild strain. We use a flat prior $P(\boldsymbol{\theta}) = \text{const.}$, between 9% and 109% for

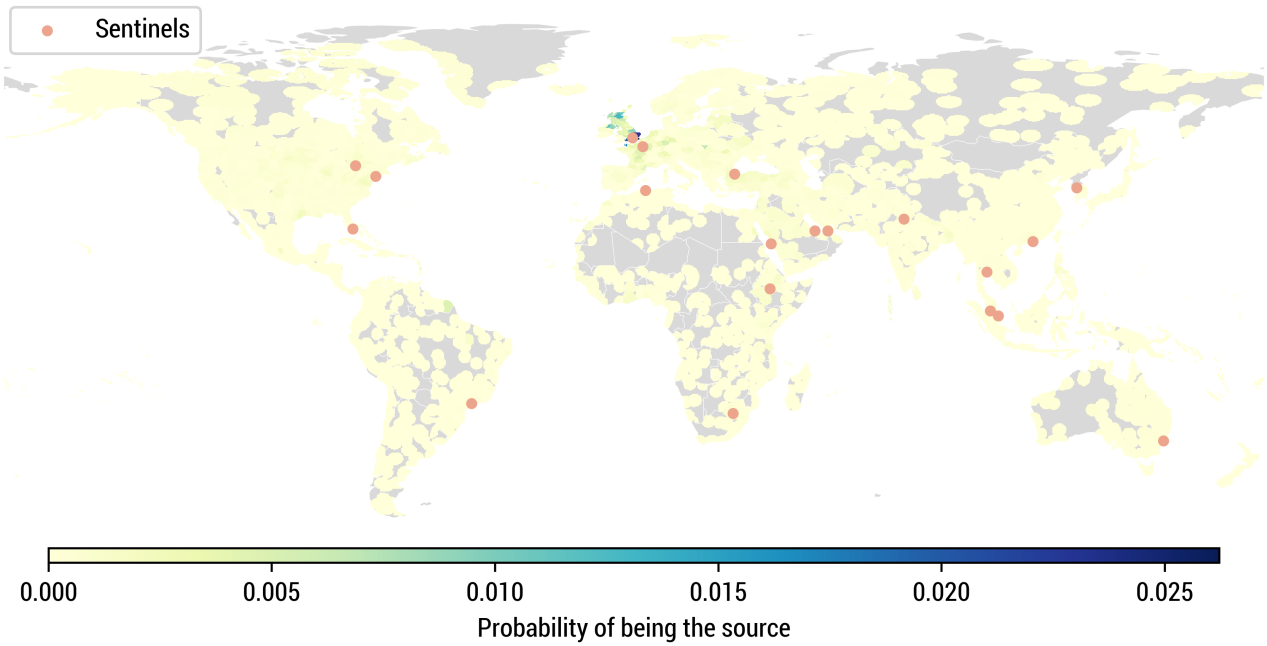

Figure S18: Geolocalization of the source for the SARS-CoV-2 Alpha variant counterfactual scenario. We show the posterior distribution over subpopulations averaged over 1250 GLEAM simulations, when ≥ 10 cumulative wastewater detections have occurred. We use the same model parametrization as in Fig. 6 for the geolocalization.

the increased transmissibility ($\mathcal{R}_{\text{eff}}^{\text{alpha}} \in [1.2, 2.3]$) and between July 12 and October 20, 2020, for the starting date (cluster of 20 latent and 20 infectious). In Fig. S19, we also illustrate a subset of the posterior distributions from individual time series.

4.2 SARS-CoV-2 (wild strain) emergence

To assess the potential effectiveness of a WWSN in early detection and response to a pandemic situation, we analyze a second hypothetical scenario: the operation of a WWSN prior to the onset of the COVID-19 pandemic. This counterfactual study utilizes air-travel data from December 2018 to February 2019, along with the baseline WWSN of 20 sentinels (see Table S6).

Calibration on importations

Considering the high uncertainty at the beginning of the pandemic, we first calibrate our model to available data. To do so, we use the same approach as in Refs. [5, 6], i.e., we calibrate our model on the number of international importations until January 23rd, 2020, when travel restrictions were imposed.

Only a fraction of importations are identified at the destination, notably because of asymptomatic individuals—we considered a 40% rate of asymptomatic individuals [50]—, but also because of different levels of capacity for detection. To account for the heterogeneity in case detection, we stratify countries into three groups based on the second component of the Global Health Security Index: high ($\geq$80th percentile), low ($\leq$20th percentile), and medium (the rest) surveillance capacity. We then use the estimates provided in Ref. [51] to assign a probability of detection relative to Singapore, which has had strong epidemiological surveillance in past infectious disease outbreaks including the COVID-19 pandemic. We used a 60% probability of detection for symptomatic individuals in Singapore, and then countries in the high, medium, and low categories were assigned relative capacities corresponding to 40%, 37%, and 11% compared to Singapore.

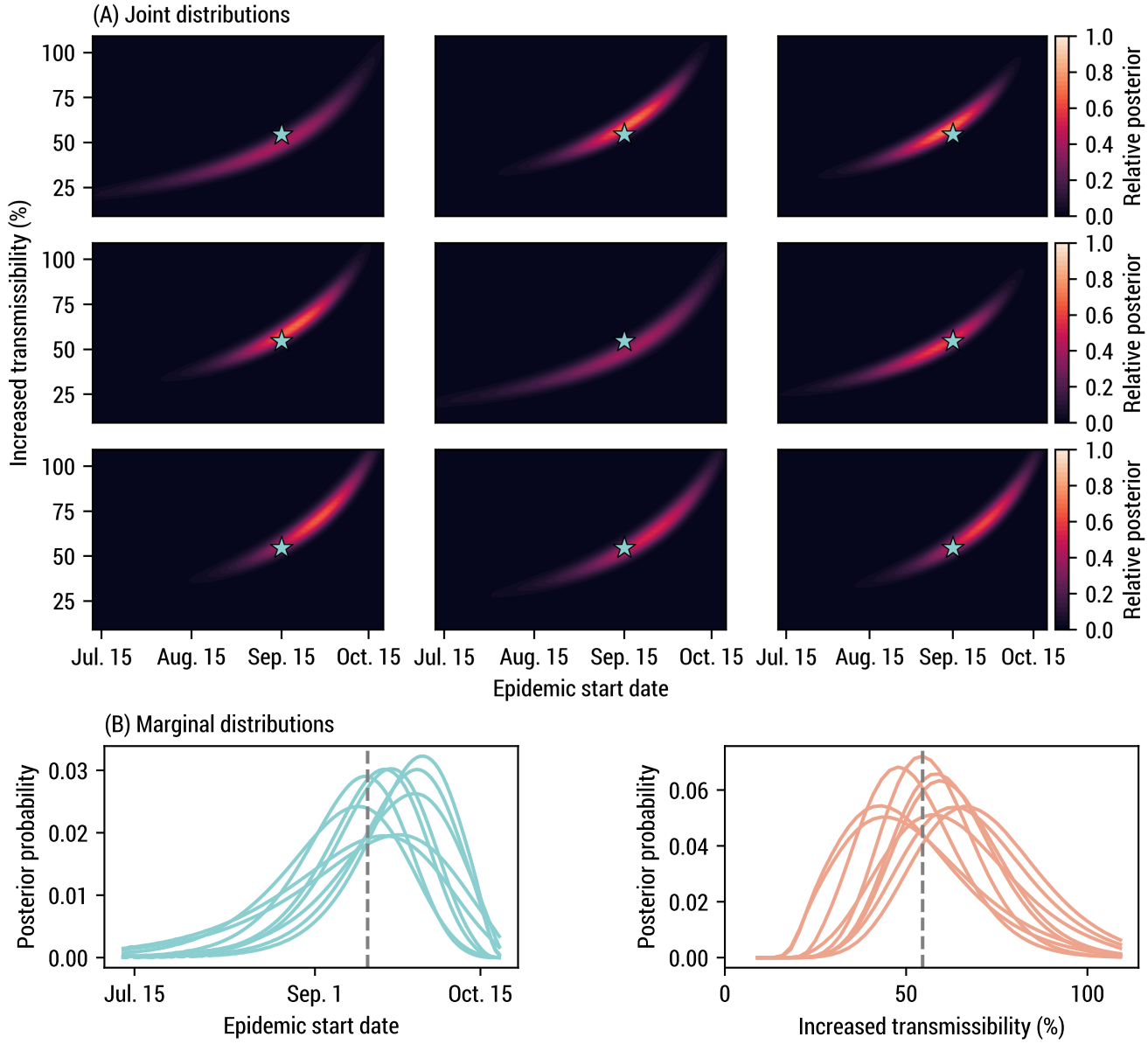

Figure S19: Examples of posterior distributions obtained for a subset of detection time series ($n = 9$) used to construct the average posterior distribution in Fig. 6C. (A) Joint posterior distributions. The blue star represents the ground truth (55% increased transmissibility and September 15, 2020, as the start date). (B) Marginal distributions, integrating over each axis. The vertical dashed line indicates the ground truth.

To calibrate our model, we compute the distribution $P(E|\boldsymbol{\theta})$ for the number of importations E given the parameters $\boldsymbol{\theta}$ of the model—in the present case, $\boldsymbol{\theta}$ corresponds to the start date and the basic reproduction number. This likelihood is used to evaluate the posterior distribution $P(\boldsymbol{\theta}|E) \propto P(E|\boldsymbol{\theta})$. We use a uniform prior between November 15th and December 1st, 2019 for the starting date with an initial cluster of 10 infectious and 10 latent individuals in Wuhan, consistent with estimates placing the index case mid-October to mid-November [52]. We also consider a uniform prior distribution on $\mathcal{R}_0$ between 2 and 2.9. The generation time is kept fixed at 6.5 days, with a latency period of 4.5 days.

In Fig. S20(A), we show the posterior distribution obtained for $\mathcal{R}_0$ and the starting date using as evidence 69

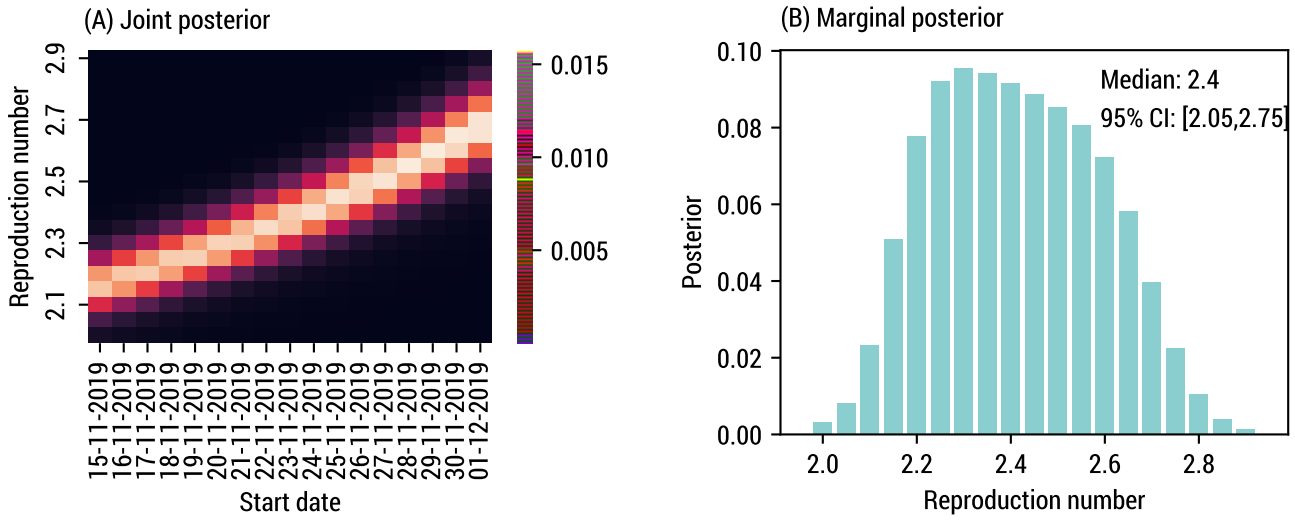

Figure S20: Calibration on international importations for the emergence of SARS-CoV-2 (wild strain). We assume an initial cluster of 10 infectious and 10 latent individuals, a generation time of 6.5 days, and a detectable period of 12.7 days. (A-B) Posterior distributions given 69 international COVID-19 cases with a travel history and an arrival date before or on Jan. 23, 2020.

identified importations by Jan. 23, 2020 (see Table S1 in the Supplementary Material of Ref. [5]). Summing the joint posterior over the plausible starting date, we obtain the marginal posterior distribution on $\mathcal{R}_0$ in Fig. S20(B), with a median of 2.4 (95% CI, 2.05–2.75). The resulting median doubling time is 4.05 days (95% CI, 3.35—5.15), broadly consistent with other estimates [5, 6, 13, 15, 16].

Results

In Fig. S21, we present similar results as in Fig. 6, but for the emergence of SARS-CoV-2 in Wuhan, demonstrating the robust early warning and situational awareness capacities of a global WWSN.

We use the joint posterior of Fig. S20(A) to compute the posterior predictive distribution for the time to first detection in Fig. S21(A). We find that even with a low detection rate (4%), there is a 54% probability that an international case outside China would have been detected earlier than the first reported case in Thailand (January 13th), with a median time to first detection on January 12th. With a 16% detection rate—more in line with estimates for a triturator sampling scheme capturing all international inbound flights—the probability to have detection prior to January 13th is 91% and the median time to first detection is on January 4th.

This hypothetical scenario presupposes the capability of detecting SARS-CoV-2 in aircraft wastewater. The key point, however, is that an operational WWSN has the potential to significantly expedite the detection of international pathogen introductions. Any reduction in the time taken to sequence the genome of emerging pathogens would directly correlate to earlier detections. Furthermore, frozen samples can be stored and analyzed in the future.

Similarly to the Alpha variant retrospective study, we use synthetic time series data from GLEAM to illustrate how we can evaluate the source and key epidemic parameters. We fix the basic reproduction number to $\mathcal{R}_0 = 2.4$ and an initial cluster of 10 infectious and 10 latent individuals on November 23, 2019, based on the joint posterior in Fig. S20(A). We obtain the posterior distribution over subpopulations as a function of the number of wastewater detections and aggregate the posterior distribution at the continent and country level in Fig. S21(C). We find reliable geolocalization capacities at the country level after about 10 detections, with a median posterior probability higher

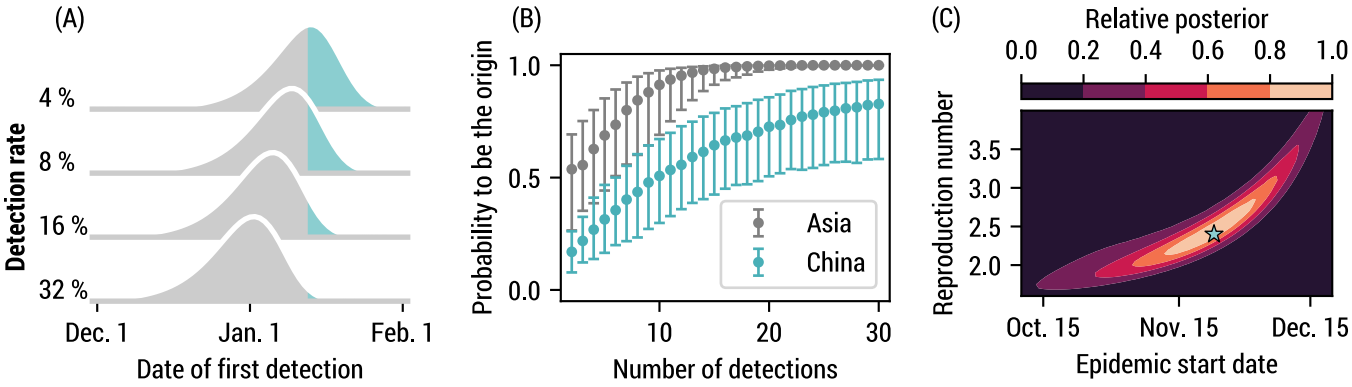

Figure S21: A global WWSN would provide an early warning system for international spreading and timely inferential capabilities. We consider a counterfactual scenario of the emergence of COVID-19 where a global WWSN would have been available. We use the baseline surveillance system consisting of 20 sentinels (see Table S6). We calibrate our model on international importations with an arrival date on or before Jan. 23 2020. (A) Distributions for the time to first detection with varying detection rates. The blue portion corresponds to dates after the first international case was reported in Thailand on January 13 [53]. (B)-(C) Inference experiment using data generated by the mechanistic GLEAM model with $\mathcal{R}_0 = 2.4$ and a start date of November 23 for the initial cluster. (B) Geolocalization of the source as more detections cumulate. We compute the posterior distribution for the origin of the epidemic based on the detection counts at each sentinel. Geolocalization of the source as more detections cumulate. We compute the posterior distribution for the origin of the epidemic based on the detection counts at each sentinel. The markers indicate the median posterior value and the error bars cover the interquartile range obtained from $n = 1200$ detection time series. (C) Joint posterior distribution on $\mathcal{R}_0$ and the start date, averaged over 59 detection time series. The blue star indicates the ground truth for the simulation experiment.

than 50%.

We also infer the basic reproduction number and the epidemic start date using the cumulative number of detections up until January 16 as the first observation $\tilde{d}$, and the cumulative number of detections between January 16 and January 23 as the second observation $\tilde{d}'$. We use a flat prior $P(\boldsymbol{\theta}) = \text{const.}$, between 1.5 and 4 for $\mathcal{R}_0$ and between October 5th and December 20th for the starting date (cluster of 10 latent and 10 infectious). The posterior distribution averaged over 59 time series is illustrated in Fig. S21(C). This average posterior indicates a median basic reproduction number of 2.4 (90% CI, 1.75–3.55), and a median starting date on November 20th (90% CI, Oct. 17–Dec. 14), illustrating the timely analytics a global WWSN could provide about the growth dynamics of emerging outbreaks.

5 Airport table for the sentinel surveillance system

We report in Table S6 the list of sentinel airports for the baseline WWSN and the different optimization schemes (volume, entropy, greedy) when considering all subpopulations as equiprobable sources of an epidemic. Each airport is identified by its IATA code. We additionally list the sentinels obtained by the greedy approach in the context of targeted optimization, assuming all subpopulations within a specific continent as equiprobable sources of an epidemic, but all subpopulations outside the continent are ignored.

References

1. Balcan, D. *et al.* Multiscale mobility networks and the spatial spreading of infectious diseases. *Proc. Natl. Acad. Sci. U.S.A.* **106,** 21484–21489 (2009).
2. Balcan, D. *et al.* Modeling the spatial spread of infectious diseases: The GLobal Epidemic and Mobility computational model. *J. Comput. Sci.* **1,** 132–145 (2010).
3. Pastore-Piontti, A. *et al.* in *Mathematical and Statistical Modeling for Emerging and Re-emerging Infectious Diseases* (eds Chowell, G. & Hyman, J. M.) 39–56 (Springer International Publishing, Cham, 2016).
4. Zhang, Q. *et al.* Spread of Zika virus in the Americas. *Proc. Natl. Acad. Sci. U.S.A.* **114,** E4334–E4343 (2017).
5. Chinazzi, M. *et al.* The effect of travel restrictions on the spread of the 2019 novel coronavirus (COVID-19) outbreak. *Science* **368,** 395–400 (2020).
6. Davis, J. T. *et al.* Cryptic transmission of SARS-CoV-2 and the first COVID-19 wave. *Nature* **600,** 127–132 (2021).
7. Gridded Population of the World (GPW). Socioeconomic Data and Applications Center (SEDAC). https://sedac.ciesin.columbia.edu/data/collection/gpw-v4, Accessed on September 12, 2023.
8. Mistry, D. *et al.* Inferring high-resolution human mixing patterns for disease modeling. *Nat. Commun.* **12,** 323 (2021).
9. Zipf, G. K. The P1 P2/D Hypothesis: On the Intercity Movement of Persons. *Am. Sociol. Rev.* **11,** 677–686 (1946).
10. Simini, F. *et al.* A universal model for mobility and migration patterns. *Nature* **484,** 96–100 (2012).
11. Wearing, H. J., Rohani, P. & Keeling, M. J. Appropriate Models for the Management of Infectious Diseases. *PLOS Med.* **2,** 621–627 (2005).
12. Krylova, O. & Earn, D. J. D. Effects of the infectious period distribution on predicted transitions in childhood disease dynamics. *J. R. Soc. Interface* **10,** 20130098 (2013).
13. Riou, J. & Althaus, C. L. Pattern of early human-to-human transmission of Wuhan 2019 novel coronavirus (2019-nCoV), December 2019 to January 2020. *Eurosurveillance* **25,** 2000058 (2020).
14. Li, Q. *et al.* Early Transmission Dynamics in Wuhan, China, of Novel Coronavirus–Infected Pneumonia. *N. Engl. J. Med.* **382,** 1199–1207 (2020).
15. Adhikari, S. P. *et al.* Epidemiology, causes, clinical manifestation and diagnosis, prevention and control of coronavirus disease (COVID-19) during the early outbreak period: a scoping review. *Infect. Dis. Poverty* **9,** 29 (2020).
16. Read, J. M. *et al.* Novel coronavirus 2019-nCoV (COVID-19): early estimation of epidemiological parameters and epidemic size estimates. *Philos. Trans. R. Soc. B* **376,** 20200265 (2021).
17. Griffin, J. *et al.* Rapid review of available evidence on the serial interval and generation time of COVID-19. *BMJ Open* **10,** e040263 (2020).
18. Foladori, P. *et al.* SARS-CoV-2 from faeces to wastewater treatment: What do we know? A review. *Sci. Total Environ.* **743,** 140444 (2020).
19. Weiss, A., Jellingsø, M. & Sommer, M. O. A. Spatial and temporal dynamics of SARS-CoV-2 in COVID-19 patients: A systematic review and meta-analysis. *EBioMedicine* **58,** 102916 (2020).
20. Li, Q. *et al.* Number of COVID-19 cases required in a population to detect SARS-CoV-2 RNA in wastewater in the province of Alberta, Canada: Sensitivity assessment. *J. Environ. Sci.* **125,** 843–850 (2023).

21. Brauer, F. *et al.* Mathematical epidemiology (Springer, 2008).
22. Allen, L. J. S. An introduction to stochastic processes with applications to biology (CRC press, 2010).
23. Miller, J. C. A primer on the use of probability generating functions in infectious disease modeling. *Infect. Dis. Model.* **3,** 192–248 (2018).
24. Roberts, D. *et al.* Quantifying the impact of individual and collective compliance with infection control measures for ethical public health policy. *Sci. Adv.* **9,** eabn7153 (2023).
25. Allard, A. *et al.* Complex Systems Modeling notes. COSMO-notes. https://cosmo-notes.github.io/index.html, Accessed on March 21, 2024.
26. Noël, P.-A. *et al.* Time evolution of epidemic disease on finite and infinite networks. *Phys. Rev. E* **79,** 026101 (2009).
27. Allen, A. J. *et al.* Predicting the diversity of early epidemic spread on networks. *Phys. Rev. Res.* **4,** 013123 (2022).
28. Boudreau, M. C. *et al.* Temporal and Probabilistic Comparisons of Epidemic Interventions. *Bull. Math. Biol.* **85,** 118 (2023).
29. Johansson, M. A. *et al.* Assessing the Risk of International Spread of Yellow Fever Virus: A Mathematical Analysis of an Urban Outbreak in Asunción, 2008. *Am. J. Trop. Med. Hyg.* **86,** 349–358 (2012).
30. Lahodny, G. E. & Allen, L. J. S. Probability of a Disease Outbreak in Stochastic Multipatch Epidemic Models. *Bull. Math. Biol.* **75,** 1157–1180 (2013).
31. Johansson, M. A. *et al.* Nowcasting the Spread of Chikungunya Virus in the Americas. *PLOS ONE* **9,** e104915 (2014).
32. Mier-y-Teran-Romero, L., Tatem, A. J. & Johansson, M. A. Mosquitoes on a plane: Disinsection will not stop the spread of vector-borne pathogens, a simulation study. *PLOS Negl. Trop. Dis.* **11,** 1–13 (2017).
33. Lai, S. *et al.* Seasonal and interannual risks of dengue introduction from South-East Asia into China, 2005-2015. *PLOS Negl. Trop. Dis.* **12,** 1–16 (2018).
34. Truelove, S. *et al.* Epidemics, Air Travel, and Elimination in a Globalized World: The Case of Measles. *medRxiv* (2020).
35. Abate, J. & Whitt, W. Numerical inversion of probability generating functions. *Oper. Res. Lett.* **12,** 245–251 (1992).
36. Hébert-Dufresne, L. *et al.* Beyond R0: heterogeneity in secondary infections and probabilistic epidemic forecasting. *J. R. Soc. Interface* **17,** 20200393 (2020).
37. Gautreau, A., Barrat, A. & Barthélemy, M. Global disease spread: Statistics and estimation of arrival times. *J. Theor. Biol.* **251,** 509–522 (2008).
38. Brockmann, D. & Helbing, D. The Hidden Geometry of Complex, Network-Driven Contagion Phenomena. *Science* **342,** 1337–1342 (2013).
39. Iannelli, F. *et al.* Effective distances for epidemics spreading on complex networks. *Phys. Rev. E* **95,** 012313 (2017).
40. Chen, L. M., Holzer, M. & Shapiro, A. Estimating epidemic arrival times using linear spreading theory. *Chaos* **28,** 013105 (2018).
41. Jamieson-Lane, A. & Blasius, B. Calculation of epidemic arrival time distributions using branching processes. *Phys. Rev. E* **102,** 042301 (2020).

42. Lloyd-Smith, J. O. *et al.* Superspreading and the effect of individual variation on disease emergence. *Nature* **438,** 355–359 (2005).

43. Airline and Airport Code Search. IATA. https://www.iata.org/en/publications/directories/code-search/, Accessed on July 30, 2024.

44. Nemhauser, G. L., Wolsey, L. A. & Fisher, M. L. An analysis of approximations for maximizing submodular set functions—I. *Math. Program.* **14,** 265–294 (1978).

45. World Health Organization. COVID-19 - United Kingdom of Great Britain and Northern Ireland. https://www.who.int/emergencies/disease-outbreak-news/item/2020-DON304, Accessed on March 19, 2024.

46. Agency, U. H. S. The R value and growth rate. www.gov.uk/guidance/the-r-value-and-growth-rate, Accessed on September 15, 2023.

47. Davies, N. G. *et al.* Estimated transmissibility and impact of SARS-CoV-2 lineage B.1.1.7 in England. *Science* **372,** eabg3055 (2021).

48. Volz, E. *et al.* Assessing transmissibility of SARS-CoV-2 lineage B.1.1.7 in England. *Nature* **593,** 266–269 (2021).

49. Distribution of number of non-zero counts of a multinomial distributed set. Mathematics Stack Exchange. https://math.stackexchange.com/q/4767477, Accessed on September 12, 2023.

50. Oran, D. P. & Topol, E. J. Prevalence of Asymptomatic SARS-CoV-2 Infection. *Annals of Internal Medicine* **173,** 362–367 (2020).

51. Niehus, R. *et al.* Using observational data to quantify bias of traveller-derived COVID-19 prevalence estimates in Wuhan, China. *Lancet Infect. Dis.* **20,** 803–808 (2020).

52. Pekar, J. *et al.* Timing the SARS-CoV-2 index case in Hubei province. *Science* **372,** 412–417 (2021).

53. World Health Organization. Novel Coronavirus – Thailand (ex-China). https://www.who.int/emergencies/disease-outbreak-news/item/2020-DON234, Accessed on September 15, 2023.

Table S6: Ordered list of sentinel airports (most important first) identified by the different optimization schemes. Each airport is identified by its IATA code [43]. We use the aggregated global air-travel network from September 2022 to August 2023. We also list the (unordered) baseline sentinels as determined in the main text.

Global				Targeted (greedy)					
baseline	volume	entropy	greedy	Africa	Asia	Europe	N. America	Oceania	S. America
ADD	DXB	FRA	LHR	DXB	DXB	IST	LHR	AKL	MIA
JNB	LHR	CDG	DXB	CDG	SIN	AMS	CUN	SIN	PTY
ALG	CDG	AMS	CDG	ADD	ICN	STN	YYZ	BNE	SCL
DXB	IST	LHR	SIN	IST	BKK	AYT	CDG	LAX	MAD
DOH	AMS	IST	IST	JNB	IST	FRA	MIA	HNL	LIS
JED	SIN	MUC	FRA	LIS	HKG	LGW	YVR	SYD	LIM
LHR	FRA	BRU	MIA	JED	JED	CPH	FRA	DPS	GRU
CDG	ICN	DXB	ICN	NBO	KUL	DXB	LAX	NAN	BOG
IST	MAD	VIE	AMS	LHR	TPE	DUB	MEX	MNL	AEP
JFK	DOH	DOH	CUN	MRS	DOH	VIE	AMS	SFO	EZE
YYZ	BKK	FCO	MAD	DOH	LHR	LHR	CPH	NRT	FLL
MIA	LGW	MXP	BKK	RUN	CAI	TLV	ICN	DXB	JFK
ICN	BCN	MAN	LAX	CAI	FRA	CDG	IAH	CDG	MEX
BKK	DUB	YYZ	DOH	BRU	DMK	EVN	PVR	KUL	CDG
DEL	HKG	STN	HKG	FRA	SHJ	MUC	PUJ	HKG	CUN
SIN	JFK	ZRH	YYZ	AMS	NRT	BCN	SJD	MEL	LHR
HKG	KUL	JFK	JED	EBB	SVO	TAS	FLL	ICN	MCO
KUL	FCO	LGW	LIS	CMN	KWI	ARN	YUL	LHR	SDQ
SYD	LIS	IAD	BNE	MXP	MNL	LTN	DFW	NOU	MVD
GRU	TPE	JNB	CPH	TUN	SGN	MAN	NRT	DOH	AMS
–	VIE	MAD	PTY	LYS	AUH	FCO	JFK	GUM	FRA
–	MUC	PRG	AYT	ABJ	MED	OSS	MNL	POM	HAV
–	ORY	DUS	TPE	MAD	CGK	PMI	YYC	BKK	PUJ
–	JED	ADD	KUL	BOM	CDG	DUS	PTY	CHC	FCO
–	YYZ	WAW	ADD	DZA	MCT	MAD	EWR	CNS	IAH
–	CPH	ORD	LGW	LPA	DEL	GYD	MBJ	YVR	YYZ
–	STN	YUL	NRT	KGL	KIX	ZRH	GDL	DEL	ATL
–	ZRH	EDI	JFK	ACC	DUS	BER	ATL	HND	BCN
–	TLV	DUB	FCO	RUH	SYD	FRU	BOG	SGN	ASU
–	CAI	BCN	AKL	BCN	SAW	AGP	MCO	ZQN	SJO
–	MAN	CPH	MNL	FCO	RUH	LIS	MAD	VLI	VVI
–	MIA	ZAG	JNB	DAR	MFM	BRU	HND	KIX	MXP
–	MXP	BER	MUC	LFW	AMS	SVO	DUB	TPE	UIO
–	BRU	CPT	GRU	LGW	HAN	ALC	MUC	WLG	LAX
–	CUN	LAX	DUB	DSS	LED	DYU	TPE	SEA	ZRH
–	NRT	BUD	CAI	KWI	PUS	MXP	ORD	CGK	EWR
–	MNL	MIA	MEX	DEL	BOM	CRL	FCO	SUV	IST
–	PMI	CRL	YVR	CPT	MEL	OSL	GRU	PVG	DXB
–	AUH	TLV	STN	KRT	AMM	OPO	LAS	OOL	GYE
–	LAX	BHX	SYD	LOS	DAC	LBD	DOH	FRA	DOH